THE UNIVERSITY *of* EDINBURGH

The flight of *Alsomitra macrocarpa*

THE UNIVERSITY
of EDINBURGH

Daniele Certini

School of Engineering
The University of Edinburgh

This dissertation is submitted for the degree of
Doctor of Philosophy

School of Engineering May 2022

To Dr Enrico Mastropaolo

To Andrea, Giovanni, Mahdi and Emma

Declaration

I declare that this thesis is an original report of my research, has been written by me and has not been submitted for any previous degree. The experimental work is almost entirely my own work; the collaborative contributions have been indicated clearly and acknowledged. Due references have been provided on all supporting literatures and resources. I declare that this thesis was composed by myself, that the work contained herein is my own except where explicitly stated otherwise in the text, and that this work has not been submitted for any other degree or professional qualification.

Acknowledgements

I would like to express my gratitude to the members of the supervisory team, including Dr Ignazio Maria Viola, Dr Cathal Cummins, Dr Francesco Giorgio Serchi and Dr Naomi Nakayama for their guidance during my PhD. My gratitude goes also to the researchers I had a chance to work with during these years, Prof Simone Camarri, Dr Richard Green, Prof Gregor Kozlowski and Dr Yunjie Yang, I appreciate their availability, support and knowledge. I am grateful for the care I have received from my parents. I am also glad that I am accompanied by old and new friends. I would like to thank everyone who helped and encouraged me throughout my past and present studies.

Abstract

Alsomitra macrocarpa is a gliding diaspore which grows on tall trees in tropical Asian forests. It does not rely on gusts nor even on a slight breeze to fly up to hundreds of meters. It is a low aspect ratio wing, which defies the conventional aerodynamic argument that efficient gliders need to be slender. Compared to pappose seeds like the dandelion, *Alsomitra macrocarpa* has a higher wing loading, yet it reaches a comparable terminal velocity. It also achieves a stable flight in the absence of both a vertical stabiliser and active control. What enables these remarkable flight abilities, which inspired the design of the first manned gliders, are yet to be understood. The investigation herein utilised image analysis, three-dimensional scans and wind tunnel tests. The morphological study highlighted *Alsomitra macrocarpa*'s uniqueness in terms of dimensions and shape. Through the use of depth cameras, the gliding path of 15 seeds was recorded. While existing literature treats *Alsomitra macrocarpa* as a flat, two-dimensional shape, drop tests evidenced a preferential flight orientation for every seed sample. Hence, and contrary to previous belief, the membrane wing has an intrados and an extrados. The majority of the seeds presented a helical path, while some moved in a straight oscillatory path that has not been previously reported, with oscillations on the vertical and horizontal plane. This gliding trajectory assumed to be two-dimensional, could be described by a simplified dynamics model. The phugoid style flight coupled the horizontal motion of a tumbling wing with the oscillation of a fluttering wing. Wind tunnel tests revealed how the membrane wing undergoes spanwise deformation under the loads experienced during a glide. This deformation displaces the aerodynamic centre from the plane of the membrane wing. Low-order dynamical models, which included a non-uniform mass distribution, were employed to recreate these oscillations in the vertical plane and showed good qualitative agreement with the experiments. Overall, this work provides new insights into the remarkably stable and efficient flight of *Alsomitra macrocarpa*. The aerodynamic conditions under which these seeds fly are in the range experienced by Micro Aerial Vehicles (MAVs). Thus, the outcomes of this thesis could aid the design of more efficient MAVs, just as early aviation pioneers were inspired when they saw *Alsomitra macrocarpa* glide down through the forest canopy.

Lay summary

Humankind has always been fascinated with flight. *Alsomitra macrocarpa*, also known as Javan cucumber, is a gliding seed that grows on high trees in tropical Asian forests. This gliding seed does not rely on gusts or a slight breeze to cover long distances. It has been a source of inspiration for the design of the first man manned gliders. Differently from the other gliding seeds, the Javan cucumber presents an unusual shape, more similar to a business card or a paper plane. A business card would tumble through the air, a paper plane would perform a steady glide, while the Javan cucumber presents a glide that is mainly affected by his deformability and weight distribution. The terminal velocity, hence the vertical component of velocity is close to the terminal velocity of dandelion seeds, known to be excellent in terms of dispersal capabilities. The investigation required classical tools commonly applied to study flying seeds like image analysis, 3D scanner and wind tunnel together with new tools such as depth cameras. While the Javan cucumber was commonly thought as a flat, two-dimensional shape, the use of a 3D scanner and drop tests showed a preferential flight orientation for all seeds studied. Wind tunnel tests highlighted the deformation of the membrane wing under the loads experienced during the glide. This deformation coupled with the weight distribution is at the origin of the phugoid motion. The phugoid style flight couples the horizontal motion of a tumbling wing and the oscillation of a fluttering wing. The gliding conditions, fall in the range experienced by Micro Air Vehicle (MAV), hence the outcomes of this thesis might help the design of more efficient MAVs, as early aviation pioneers were inspired.

Table of contents

List of figures

List of tables

Nomenclature

Roman Symbols

a Outer ellipse's semi-major axis

m_{ij} Added mass coefficients

I_a Added mass moment of inertia

a_k k-th Fourier coefficient

b Wing-span/Ellipse's semi-minor axis

b_k k-th Fourier coefficient

c Chord/Inner ellipse's semi-major axis/Damping parameter

c_{centre} Chord at wing centre

C_{Dpro} Profile drag coefficient

C_D, C_d Drag coefficient

C_{D0} Minimum drag coefficient

C_{Dmax} Maximum drag coefficient

C_L, C_l Lift coefficient

C_{Lmax} Maximum lift coefficient

C_{m0} Moment coefficient at zero-lift

C_m Moment coefficient

C_{m0} Moment due to camber coefficient

a Outer ellipse's semi-minor axis

D Drag

$a_{am}, b_{am}, c_{am}, d_{am}$ Coefficients

$C_T, C_R, C_0, C_\tau, C_{\pi/2}$ Dimensionless constants

D_{ind} Induced drag

D_{pro} Profile drag

E Efficiency

e Offset of the centre of gravity

f_a Reduced frequency

g Gravity acceleration

h Vertical distance/

k Spring constant

E_k Kinetic energy

L Lift

m Mass

M_0 Moment due to camber

$\bar{d}$ Mean depth

$m.g.c.$ Mean geometric chord

N Number of measurements/ harmonics/ wing-loading

n Number of samples

x_{am} Normalised chord

y_{am} Normalised wing-span

P Total power

E_p Potential energy

S Surface

T Descent time/Period

t time

τ_{camber} Torque due to camber

τ_{Lift} Torque due to lift

E_T Total energy

U Velocity

u Horizontal component of velocity

U_2 Minimum power speed

U_3 Minimum drag speed

v Lateral component of velocity

$\mathbf{V}_b = (u_b, v_b)$ Velocity vector of centre of buoyancy

$\mathbf{V}_g = (u_g, v_g)$ Velocity vector of centre of gravity

$\mathbf{X} = (x, y)$ Position vector in laboratory reference frame

$\mathbf{X}_g = (x_g, y_g)$ Position vector in body-fixed reference frame

W Weight

w Vertical component of velocity

ξ Fundamental frequency

x, y, z Inertial reference frame

a_x, a_y, a_z Acceleration components

U_{min} Minimum flight speed

Greek Symbols

α Angle of attack

α_{trim} Trimmed angle of attack

δ Displacement

Γ Circulation

γ Glide angle

Λ Sweep angle

ν Kinematic viscosity

ρ Density

ρ_a Density of ellipse with semi-major axis c

ρ_p Density of ellipse with semi-major axis a

τ^{ν} Dissipative torque

θ Angle between y_g and and **g**

Acronyms / Abbreviations

AR Aspect Ratio

$\bar{d}$ Mean value of the depth measurements

DF Descent factor

d_{gt} Ground truth depth

d_t Depth at time t

EFD Elliptical Fourier Descriptors

E_{random} Random error

$E_{systematic}$ Systematic error

FA Fluctuating Asymmetry

FFT Fast Fourier Transform

MAV Micro Air Vehicle

PC Principal Component

PCA Principal Component Analysis

PIV Particle Image Velocimetry

Re Reynolds number

RGB red, green, and blue colour model

UAV Unmanned Aerial Vehicle

WL Distance between the longitudinal axis and the left tip of the wing

WR Distance between the longitudinal axis and the left tip of the wing

Chapter 1

Introduction

1.1 Seed dispersed by the wind: a source of inspiration

The dream of flying has always fascinated humankind. It has been a driving force for the foundation of the science commonly known as *Bionics*. The term *Bionics*, introduced by Jack E. Steele in 1958, refers to the application of construction principles available in nature, to implement technological solutions (Srisuwan, 2020). *Bio-inspiration* is a more comprehensive domain instead, it involves *Bionics*, *Biomimetics* and *Design* and it adopts "phenomena in biology to stimulate research in non-biological science and technology" (Whitesides, 2015). The simple gliding of birds and the wind dispersal of seeds were an inspiration for engineers and scientists. The full spectrum of natural fliers provides a rich source of solutions for all kinds of flying machines (Kulfan, 2009). Seed dispersal allows plants to have some sort of mobility and it is a means of reproduction. Seeds present mass and energy efficiency, together with robustness and complete autonomy. Leonardo da Vinci was probably inspired by the descent of the maple seed, to design his aerial screw. Otto Lilienthal built the first gliders near the end of the 19^{th} century and was awarded the first worldwide bionic patent in 1893 (Knippers et al., 2016). After Otto's tragic death while flying one of his gliders, Ignaz and Igo Etrich, Austrian aviation pioneers, carried on his work. In order to build an inherently stable surface, Igo Etrich studied *Alsomitra macrocarpa* (Kulfan, 2009) and built the Taube, a monoplane-type aircraft (Srisuwan, 2020). It proved to aviation pioneers that it was possible to have a tailless air-plane, gifted with stability (Kulfan, 2009). "Plants mastered the art and science of aviation long before Orville and Wilbur Wright propelled their frail craft into the air" Dr McMasters once said (Chen and McMasters, 1981).

1.1.1 The natural glider

Alsomitra macrocarpa pictured in figure 1.1, is a genus of the plant family *Cucurbitaceae* and a perennial climber (Singapore, 2021). *Alsomitra macrocarpa* is a diaspore, a seed, that has a function in plant dispersal. For ease of readability, seed could be used in place of diaspore. The plant can reach up to 50 m in length and the base of stems of mature plants up

Fig. 1.1 A diaspore of *Alsomitra macrocarpa*, the scale bar is 1 cm.

to 15 cm in width (Singapore, 2021). It grows on high trees (figure 1.2a), towards the canopy, looking for sunlight in football-sized pods (figure 1.2b). *Alsomitra macrocarpa* is a type of climbing gourd, commonly known as the Javan cucumber, that climbs trees, adhering to trunks for support via adhesive discs, on the tip of the bifid tendrils. It is found in the tropical Asian forests of the Malay Archipelago: Southern Thailand, Peninsular Malaysia, Borneo, Indonesia, Philippines and New Guinea (Gardens, 2022). The tropical areas where *Alsomitra macrocarpa* grows, lack seasons (Sobel, 2012). Tropical plants tend to follow their nutritional levels and maturity to set up their life. Each pod is 20 cm to 30 cm in diameter and contains hundreds of individual seeds (figure 1.2c), peeled away by the wind. When the diaspores of *Alsomitra macrocarpa* are ripe the pod becomes brown. The glider, shown in figure 1.1, is composed of a seed containing pericarp of brown colour, placed near the leading edge and centred on the longitudinal axis, with a circular shape of 2 cm to 3 cm in diameter and a membranous wing of 17 cm in span. The gliding flight of seeds is usually unstable oscillations due to the nonlinear behaviour of the air which can lead to rocking, spinning and spiral gliding paths; *Alsomitra macrocarpa* is an exception (Minami and Azuma, 2003). Another key feature is that, unlike seeds from pioneer trees and maples (Lentink et al., 2009),

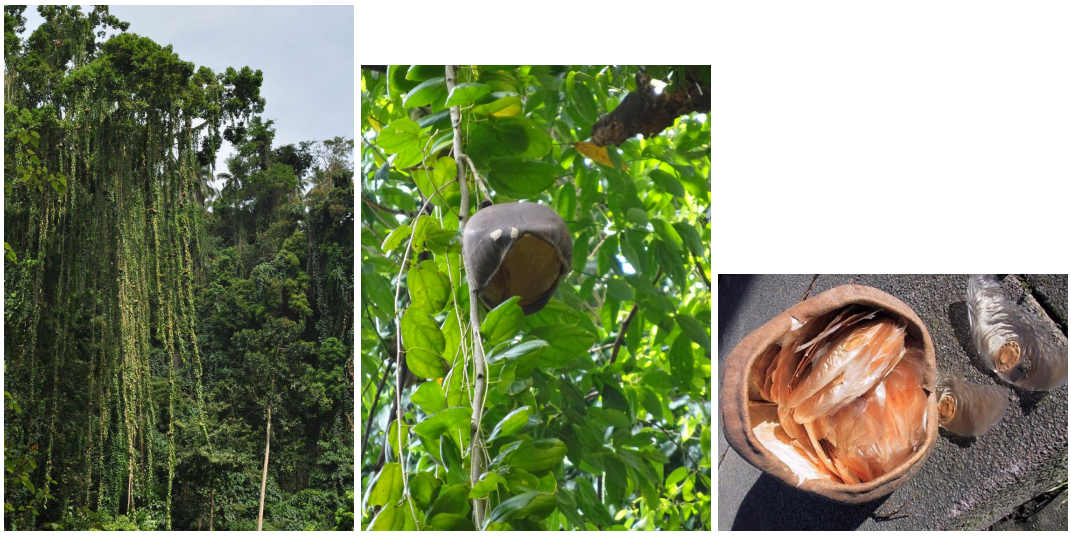

(a) Lianas hanging from a tree. (b) A liana with a pod. (c) A pod full of seeds.

Fig. 1.2 These images highlight the various elements of the plant: liana, pod and seeds.

Alsomitra macrocarpa does not rely on wind, gusts and updrafts to cover distances up to hundreds of meters (Viola et al., 2022). It has the highest descent time $T = \sqrt{0.5\rho\,\mathrm{DF}/(W/S)}$, where ρ is the density of the fluid, air, in this case, DF is the descent factor, W is the weight and S is the surface area (Lentink et al., 2009). *Alsomitra macrocarpa* outperforms the autorotating seeds, demonstrating how its design provides unique capabilities (Lentink et al., 2009). Descent time is proportional to the square root of descent factor $\mathrm{DF} = (1 + (u/w)^2)C_L$, where u is the horizontal velocity and w is the descent velocity or terminal velocity, hence the vertical component of the velocity vector, and C_L the lift coefficient. The descent factor gives an indication of the aerodynamic efficacy, it is divided by the wing loading (W/S), ratio between weight (W) and surface (S) of *Alsomitra macrocarpa* in the equation for the descent time (Lentink et al., 2009). Figure 1.3 highlights how *Alsomitra macrocarpa*, represented by a red diamond, is far from the average, it is a specialised gliding seed (Lentink et al., 2009), in terms of size, distance covered and type of flight, just to name a few.

1.1.2 Historical notes

Igo Etrich constructed a kite and then an unmanned glider, based on the shape of *Alsomitra macrocarpa*, in 1904 (Hertel, 1966). In 1910 Etrich built the *Dove*, a successful aircraft, where the concept of an inherently stable flying-wing like *Alsomitra macrocarpa* had to be replaced by birds, as an inspiration (Hertel, 1966). Birds have a tail and are capable of active control of their surfaces: wing and tail. The stability of *Alsomitra macrocarpa*, instead, is related to its shape, which is fixed. Its majestic flight more recently caught the

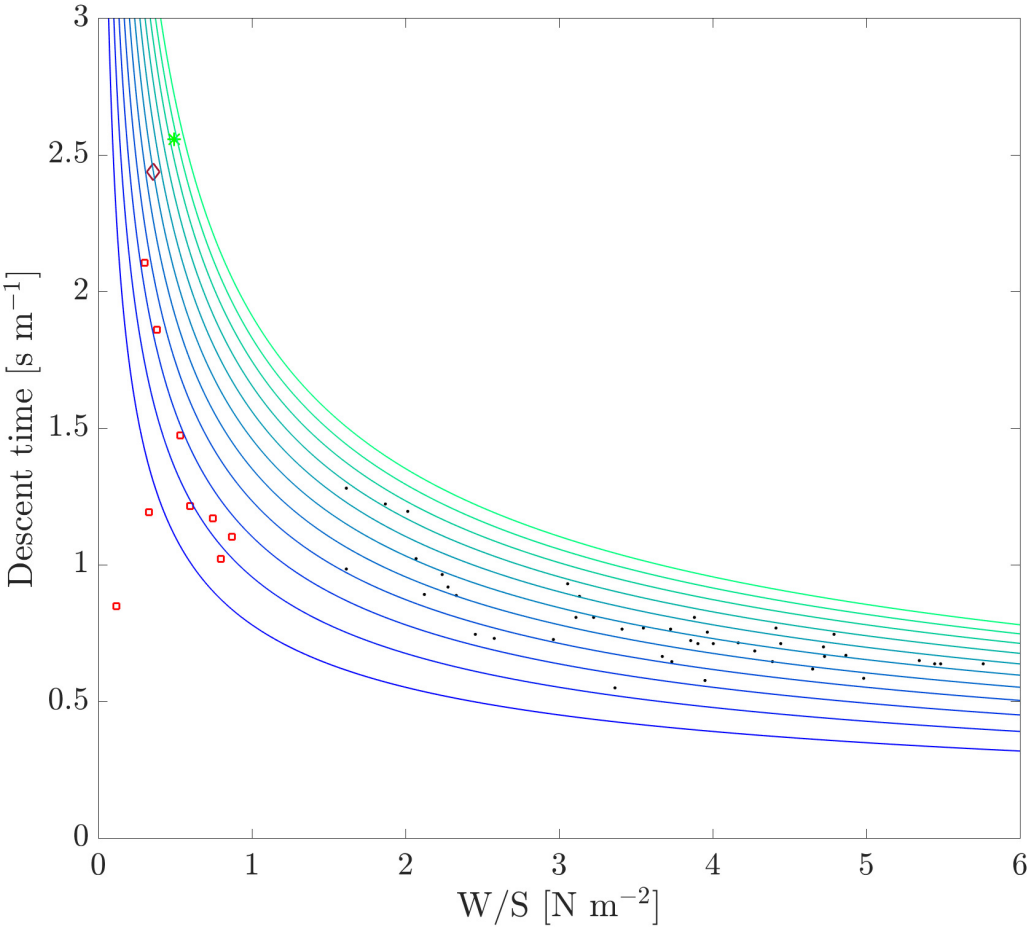

Fig. 1.3 The plot, adapted from Lentink et al. (2009), relates the descent time of autorotating seeds (·), such maple seeds, with that of straying seeds and gliding seeds (□), such as *Alsomitra macrocarpa*, which has the lowest descent time (Azuma and Okuno, 1987). The green star (∗) at the top right is the Dandelion, plotted with data available in Cummins et al. (2018). The coloured hyperbolic curves indicate the descent time as a function of wing loading at a constant descent factor.

attention of Sir David Attenborough, who featured *Alsomitra macrocarpa* in his award-winning TV series *Life* in 2009 (BBC, 2009) and a book (Attenborough, 1995) that he previously published. In 2016 the BBC briefly featured *Alsomitra macrocarpa* in *Life in the Air: Defying Gravity* (BBC, 2016). Studies from scientists and engineers are the result of *Alsomitra macrocarpa*'s exceptional glide. The pitching stability, for instance, is given by the centre of gravity being correctly positioned in front of the mean aerodynamic centre (Azuma and Okuno, 1987). The seed has an elliptical shape, whose centroid coincides with the centre of gravity. It is located on the axis of symmetry of the wing, towards the leading edge, it defines the location of the centre of gravity for *Alsomitra macrocarpa*. The membrane wing, whose mass is assumed to be negligible, is shaped as a flying wing, locating the mean aerodynamic centre to the rear of the centre of gravity (Azuma and Okuno, 1987). This highlights how a fixed geometry gives an important contribution to the stability of flight. Other contributions come from the tapered plan form of the wing, twisted (washout) and dihedral angle and reflected airfoil (Azuma and Okuno, 1987). Igo Etrich designed a stable glider by scaling up the shape of *Alsomitra macrocarpa*, however the addition of weights, in the form of a pilot and an engine, was changing the position of the centre of gravity, so some sort of control was required, hence the design inspired by a bird, the *Dove*. The change in scale, from the size of a seed, a few centimetres, to the size of a glider, three orders of magnitude bigger, had a great impact on the fluid dynamics. The Reynolds number ($Re = UL/\nu$, where U is the relative flow speed experienced by the diaspore, L is a characteristic length like the wing chord at the wing centre of *Alsomitra macrocarpa* and ν the kinematic viscosity of air) gives an indication of the relative magnitude of two crucial forces acting on a flying body: inertial and viscous forces. It is a few thousand for *Alsomitra macrocarpa*, while of the order of millions for a glider. This difference in the Reynolds number indicates a completely different flow behaviour, hence flow topology. Despite totally different fluid dynamics, Igo Etrich got a deep insight into flight. The knowledge acquired helped, later, the Horten brothers to develop the first flying wing aircraft, the Ho 229 in 1944 (Barba, 2011). The 20^{th} century was the era of planes and rockets, instead, the 21st century will be characterised by autonomous drones (UAVs). The applications range from agriculture, environment preservation and disaster mitigation to space exploration (Floreano and Wood, 2015). A new class of UAVs has recently emerged: micro air vehicles (MAVs), defined as drones with no length dimension greater than 150 mm and weight below 200 g, requirements that perfectly fit the morphology of *Alsomitra macrocarpa* (Azuma and Okuno, 1987). MAVs work in a low Reynolds number environment ($10^2 < Re < 10^4$), a flow regime full of complex flow phenomena, optimised by nature over thousands of years (Lentink et al., 2009), (Cummins et al., 2018). The type of flight performed by *Alsomitra macrocarpa* is

gliding, commonly used by birds, like Fregata minor, to sleep in mid-flight, allowing them to fly over the ocean for up to 10 days (Rattenborg et al., 2016). Insects use gliding for thermo-regulation (Church, 1960), in order to protect the performance of the flight muscles. Nature is a source of inspiration to improve the efficiency and aerodynamic performance of MAVs.

1.2 Research questions, aims and objectives

Alsomitra macrocarpa performs either spiral or straight gliding flights (Minami and Azuma, 2003), a unique feature that distinguishes it from the majority of seeds which show only a type of flying behaviour. This unique flight is not only due to the flight mechanics but also to the aerodynamics of *Alsomitra macrocarpa*, and thus the: lift (L) and drag (D) driving the flight. The aim of the thesis is to describe the gliding flight of *Alsomitra macrocarpa*, the trajectory, velocity and acceleration, and the flow structures and shape changes during the glide. The research questions:

1. What are the flow structures around the seed when it is gliding? Is the lift provided by a Leading Edge Vortex (LEV) as in autorotating seeds of maples (Lentink et al., 2009) and swift wings (Muir et al., 2017) or is it given by a distribution of vortices in the valley of corrugated wings, as for dragonflies (Vargas et al., 2008) and (Murphy and Hu, 2010). Is it a combination of Leading Edge Vortex and distribution of vortices? Could it be a completely new flow topology, such as the recently discovered Separated Vortex Ring (SVR) of the dandelion (Cummins et al., 2018)?

2. Can the three-dimensional gliding flight of *Alsomitra macrocarpa* be described, capturing the time dependence of position, velocity and acceleration?

3. What causes different *Alsomitra macrocarpa* to exhibit different gliding paths: spiral or straight gliding? Can we define a quasi-steady model that describes the gliding path?

These research objectives were pursued:

1. Measure morphological parameters that describe the shape on a statistically significant sample size;

2. Evaluate the deformation of the membrane wing in a low-speed wind tunnel;

3. Describe the flow field;

4. Track *Alsomitra macrocarpa* during its glide;

5. Development of a phenomenological model based on ordinary differential equations to predict straight gliding flight.

1.3 Thesis synopsis

Following on from this introductory chapter, the remainder of the thesis consists of as follows.
Chapter 2: Materials and methods
This chapter describes the experimental tools used to address the research questions: analytical balances, 3D scanner, wind tunnels, spectrofluorometer and depth cameras. The post-processing techniques are also described: morphometric analysis, Particle Image Velocimetry (PIV), principal component analysis (PCA) and vortex identification.
Chapter 3: Results
This chapter presents the results from the analysis of the data collected with the methods listed in the previous Chapter.
Chapter 4: Discussion
This chapter discusses some concepts from flight Mechanics and results available in the literature. It introduces the low-order model developed to study the gliding trajectory of *Alsomitra macrocarpa*.
Chapter 5: Conclusions
This chapter summarises key findings and outcomes from this thesis.
Chapter 6: Future Work
In the last chapter, the future work conducted by the author and his collaborators on the results obtained is briefly outlined.

1.4 Publications

The body of research listed in this section was instrumental in developing some of the experimental tools and the scientific approach used in this thesis. The characterisation of the morphology, design of drop tests, object tracking, and definition of simple models to capture some aspects of the flight of seeds are some examples.

1.4.1 Journal papers

- Certini, D., Fazan, L., Nakayama, N., Viola, I.M. and Kozlowski, G., 2020. Velocity of the falling dispersal units in Zelkova abelicea: Remarkable evolutionary conservation within the relict tree genus. American journal of botany, 107(12), pp.1831-1838;
- Cummins, C., Seale, M., Macente, A., Certini, D., Mastropaolo, E., Viola, I.M. and Nakayama, N., 2018. A separated vortex ring underlies the flight of the dandelion. Nature, 562(7727), pp.414-418.

1.4.2 Conference abstracts

- Certini, D., Cummins, C., Giorgio-Serchi, F., Yang, Y., Nakayama, N. and Viola, I.M., 2022. The flight of Alsomitra macrocarpa. ECCOMAS, Oslo, Norway, 5/06/2022 - 9/06/2022;
- Certini, D., Fazan, L., Nakayama, N., Kozlowski, G. and Viola, I.M., The branch-aided chaotic dispersal of Zelkova abelicea. 73rd Annual Meeting of the APS Division of Fluid Dynamics, online, 22/11/2020 - 24/11/2020.
- Certini, D., Cummins, C., Mastropaolo, E., Nakayama, N. and Viola, I.M., 2019. On the aerodynamics of the gliding seeds of Javan cucumber. UK Fluids Conference, Cambridge, UK, 27/08/2019 - 29/08/2019.

Chapter 2

Materials and methods

2.1 The seeds

In order to perform a representative description of the morphology of *Alsomitra macrocarpa* and understand the differences in the morphology that lead to different flight behaviours, 32 seeds were purchased from two different suppliers. Jam-Kobayashi provided 28 seeds in two shipments of 20 and 8 seeds respectively, while the remaining 4 were supplied by Onszaden. Unfortunately, three seeds, supplied by Jam-Kobayashi, were damaged during preliminary tests in the wind tunnel. Figure 2.1 displays the 31 *Alsomitra macrocarpa* used to have a characterisation of the morphology.

2.2 Morphometric analysis

Morphometric analysis is a technique commonly used in areas of plant biology such as agriculture (de Oliveira et al., 2016), evolution (Rose et al., 2016) and ecology (Gómez et al., 2016), to describe multiple quantitative characters among the population investigated, for instance, lengths, angles, masses, followed by inferential statistics on the data collected to uncover hidden structures (Chuanromanee et al., 2019). This analysis is the so-called *traditional morphometric*. It has been crucial to define species as shown by Boyd (2002) and Bateman and Rudall (2006). *Geometric morphometrics* instead requires a quantitative, analytical representation of a shape, involving outlines, in order to compare different shapes, for instance, flowers, leaves and seeds. The outline of *Alsomitra macrocarpa* pictured on a white background was the starting point to perform elliptical Fourier analysis, crucial in pattern recognition problems to describe image contours (Kuhl and Giardina, 1982). Digitised herbarium specimens of *Alsomitra macrocarpa* could not be analysed, because of

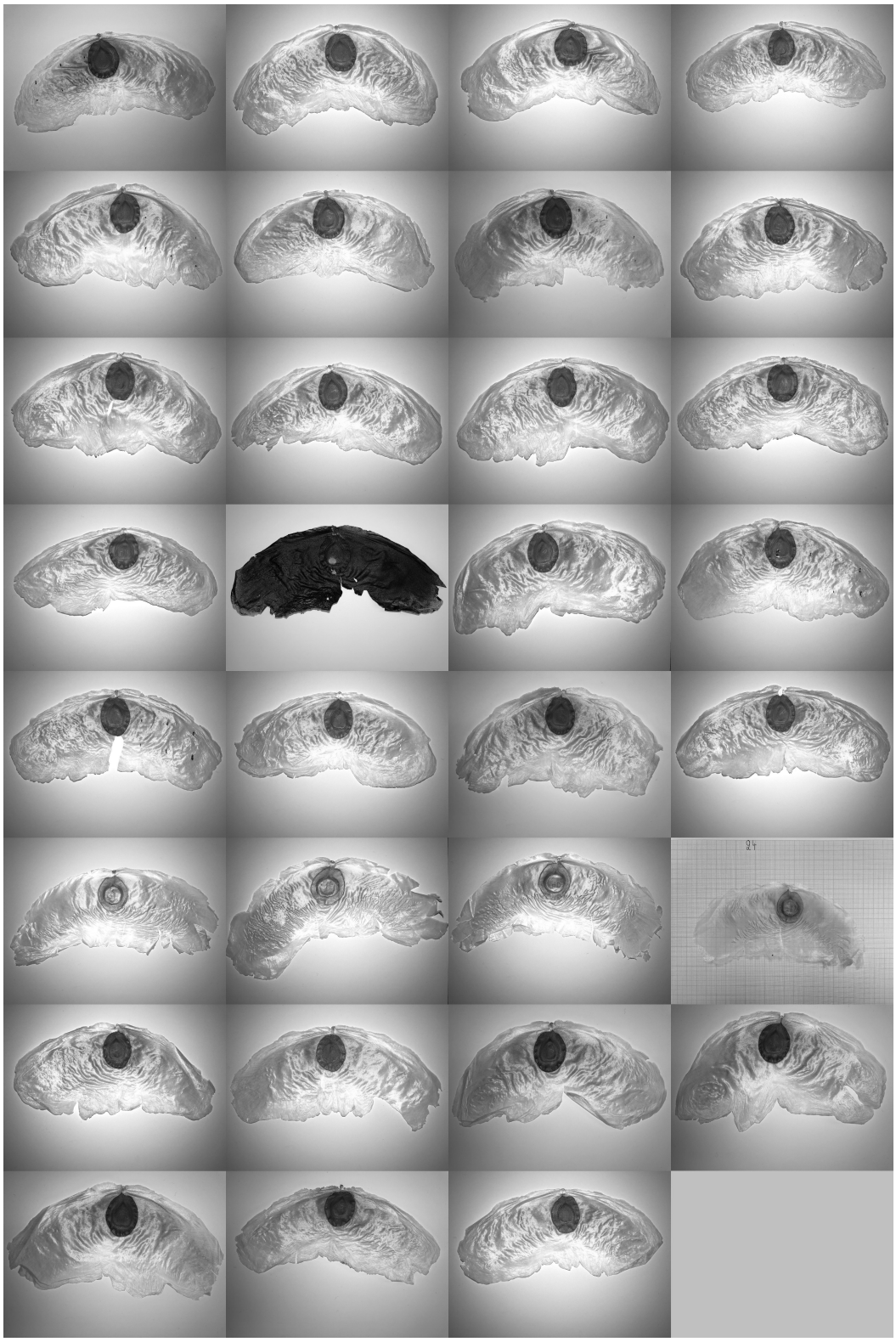

Fig. 2.1 *Alsomitra macrocarpa* used in the experimental investigations.

the state of conservation of the pictured *Alsomitra macrocarpa* (Gardens, 2022; ITHAKA, 2022). Elliptical Fourier analysis is an analytical tool used to characterise the shape of different objects (Neto et al., 2006). This technique allowed Innes and Bates (1999) to build a connection between the morphology of shells and their genotype. McLellan and Endler (1998) reviewed different morphometric methods and found that 15 harmonics of the Elliptic Fourier method accurately drew boundaries of *Acer palmatum*, *Acer saccharum* and *Acer saccharinum* leaves. As a consequence, 15 harmonics were treated as sufficient for *Alsomitra macrocarpa*. The combination of *traditional morphometric* and *geometric morphometrics* has lead to the understanding of patterns, for instance in *Passiflora* leaves (Chitwood and Otoni, 2017). The lack of clearly identifiable, meaningful landmarks, excluded the use of Procrustes analysis, a shape comparison that scales the data equally, providing an analysis that focuses on differences among shapes. Procrustes analysis is based on landmark data that identify homologous points of shape.

2.2.1 Mass

Two analytical balances: Sartorius Extend, Model ED822-CW and Mettler Toledo XP4002S both with a readability of 0.01 g measured the mass of 31 *Alsomitra macrocarpa*. The results are reported in Table 3.1 and Table A.1. While most *Alsomitra macrocarpa* had a mass (m) of 0.36 g (0.32 g to 0.39 g (95% confidence interval)); n = 31 seeds), four showed a mass less than half of the mean mass and were considered underdeveloped.

2.2.2 Morphological analysis of size and shape

Pictures of 29 *Alsomitra macrocarpa* were taken by a camera phone, under natural lightning conditions. The phone had automatic focus on and was placed around 200 mm above the imaged seed, with the light behind the phone. The resolution of the images was set to 3024 px times 4032 px, resulting in a resolution of 20 px/mm. The seeds were imaged on both sides, lying on a flat, white surface (Fig. 2.2a). Images were processed with the commercial software Photoshop to get a homogeneously white background, performing background subtraction (Fig. 2.2b) and covering *Alsomitra macrocarpa* with a black mask, in order to avoid errors given by the irregular and transparent surface (Fig. 2.2c). A ruler in each image allowed to have a size-scale for image calibration, to define the physical size scale of pixels in the image (Fig. 2.2). A similar quality of the processed pictures was obtained with the image processing software Fiji (Schindelin et al., 2012), that was discarded, because of time constraints. Subsequently, MASS, a tool for MATLAB, described in Chuanromanee et al. (2019), was used to analyse the pictures to extract the measures highlighted in figure 2.3 and

(a) Original picture. (b) Background subtracted. (c) Black mask.

Fig. 2.2 Editing of the picture used as input for MASS (Chuanromanee et al., 2019).

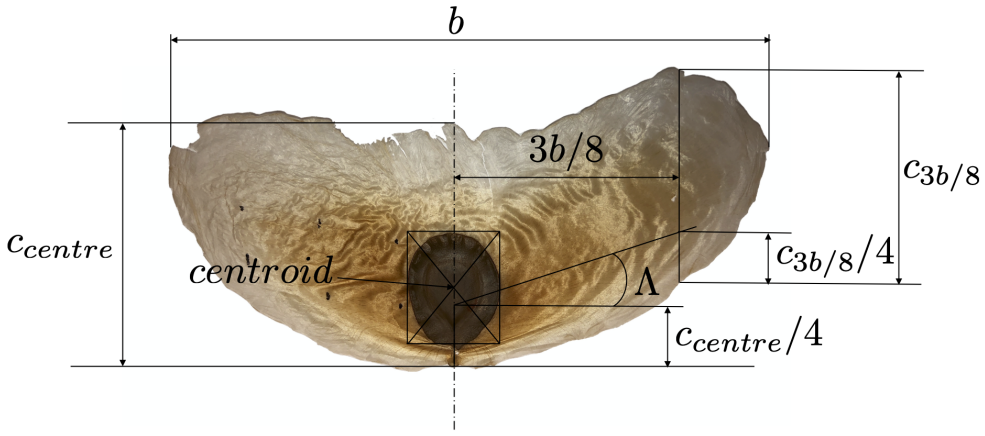

Fig. 2.3 Diagram showing the geometrical characteristics reported in table A.1.

reported in Table A.1. MASS was developed focusing on leaves, it can also be applied to flowers and seeds (Chuanromanee et al., 2019). The centroid of the seed and its principal axes were calculated from a binarised version of the original image. The images were then rotated to align the longitudinal axis with the vertical direction. These geometrical transformations allowed the recording of basic measurements of *Alsomitra macrocarpa*. Wing-span and wing chord on the longitudinal axis were measured fitting the planar shape of *Alsomitra macrocarpa* with a bounding box, whose height was directly linked to the wing chord, while the width with the wing-span. The wing area was extracted as the difference between the area of the bounding box and that of the white pixels in the bounding box. Values are reported in Table A.1. An important parameter to describe the shape of leaves, flowers and seeds is the fluctuating asymmetry (FA), a form of biological asymmetry, listed in Table A.3. It highlights small and usually random variations away from perfect bilateral symmetry (Van Valen, 1962).

Fluctuating asymmetry was investigated as a potentially insightful parameter influencing the type of flight path described.

$$FA = 2\left(\frac{WL - WR}{WL + WR}\right), \tag{2.1}$$

where WL and WR represented the euclidean distance from the longitudinal axis of *Alsomitra macrocarpa* to the left and right edge of the wing, respectively. The denominator of (2.1) is the wing span of *Alsomitra macrocarpa*. Fluctuating asymmetry ranges between -2 and 2. A perfectly symmetrical specimen has FA = 0, a positive value, caused by WL > WR means that the shape skews to the left of the longitudinal axis, while a negative value, the opposite, i.e. WR > WL. In Table A.3 the value of each *Alsomitra macrocarpa* is reported, it is a positive measure of the symmetry. The binarised image was subsequently employed to extract the Elliptical Fourier Descriptors (EFD) of each *Alsomitra macrocarpa* (Chitwood and Otoni, 2017; Klein and Svoboda, 2017). Elliptical Fourier analysis is a curve-fitting technique used to describe closed outline shapes. The perimeter of an object is described by a finite sum of sine and cosine functions. The perimeter is captured in a continuous manner at a precision related to the number of harmonics recorded. The Procrustes analysis, on the contrary, captures information in discrete locations, with the details falling in between landmarks failing to be taken (Caple et al., 2017). Elliptical Fourier analysis required *Alsomitra macrocarpa* to be scaled to a normalised length and be a closed contour (Kuhl and Giardina, 1982). Nearest-neighbour searching algorithm identified pixels belonging to the perimeter of the wing. This closed contour was then converted in an 8-bit chain code (Kuhl and Giardina, 1982), to be analysed by the Elliptical Fourier for Shape Analysis tool available in MATLAB's File Exchange (Manurung, 2016). The chain code that described the edge of the wing was fitted by a Fourier series with 15 harmonics as in Chuanromanee et al. (2019). The leading edge has a smooth, almost parabolic shape, easily described by a low ($N < 15$) number of harmonics. The main contribution achieved by increasing N was improving the number of details captured at the trailing edge, an indented profile. The EFD-generated outline for one *Alsomitra macrocarpa* using $N = 10$, $N = 15$ and $N = 20$ harmonics, is displayed in Fig. 2.4. The *Alsomitra macrocarpa* object of this thesis was accurately fitted by $N = 15$ harmonics. The four Fourier coefficients that define each harmonic were extracted and compared across the population of 29 *Alsomitra macrocarpa*. This fitting was followed by Principal Component Analysis (PCA), in order to compare the planar shape across the population.

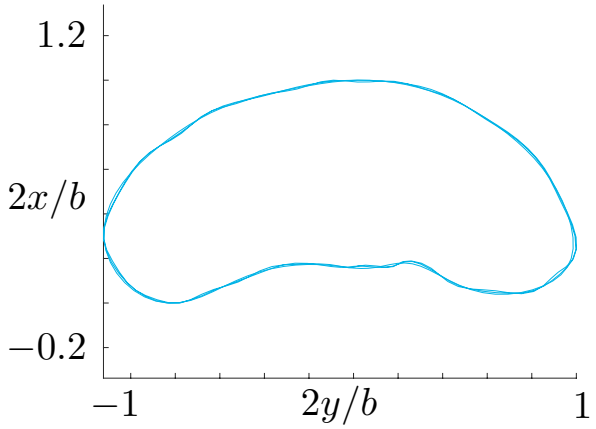

Fig. 2.4 Three EFD outlines highlighting results with N = 10, N = 15 and N = 20 harmonics.

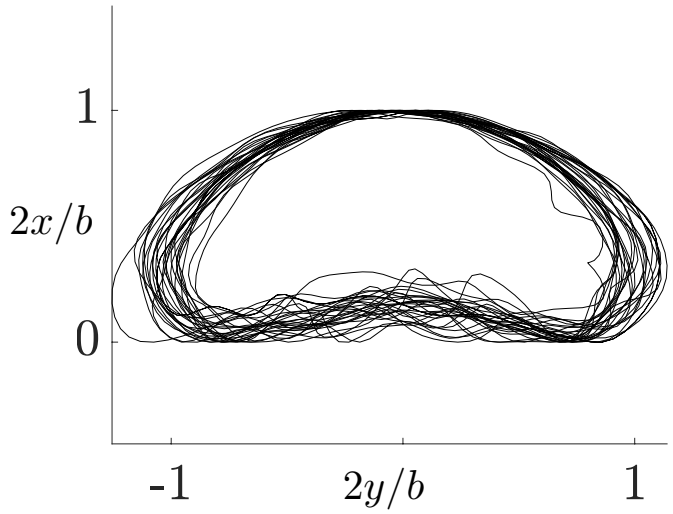

Fig. 2.5 Outline comparison of 29 *Alsomitra macrocarpa*.

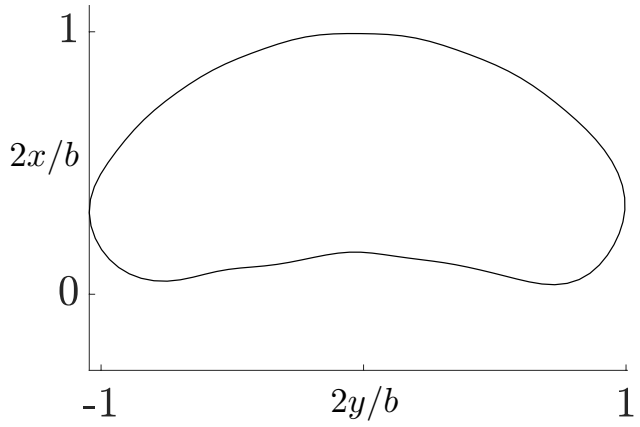

Fig. 2.6 Mean outline of the 29 *Alsomitra macrocarpa*.

2.2.3 Principal component analysis

The morphological values recorded in Table A.1 and Table A.2 represented a set of high-dimensional data with intrinsic complexity. Principal component analysis (PCA) performs a dimensional reduction of the data set while retaining patterns. It is similar to clustering (Lever et al., 2017). PCA performs a geometrical projection of the data onto lower dimensions, the principal components (PCs). The goal is to summarise the data studied using a limited number of PCs. The first PC (PC1), minimises the distance between the data and their projection onto PC1. The variance of the projected points is maximised, as a consequence. The following PCs follow the same goal, plus they need to be uncorrelated with all the previous PCs. The PCs are geometrically orthogonal and independent. The maximum number of PCs is then given by the number of samples (31 *Alsomitra macrocarpa*) or the number of features studied (8), depending on which is the smaller. Correlation is maximised by the PC selection process. These coefficients compose a matrix, and from a geometrical perspective, it can be interpreted as a rotation matrix. It rotates the data so that the projection with the greatest variance goes along the first axis. Linear regression minimises the distance between the response variable and the calculated value, while PCA minimises the perpendicular distance between a data point and a principal component. In most studies not all the extracted PCs are typically used, given that the majority of variance, the patterns in the data set, are usually limited to the first PCs. By limiting the number of PCs taken into account to 2 or 3 it is possible to plot the data in a scatter plot as in figure 2.7a and figure 2.8a, where it is possible to spot clusters (Lever et al., 2017). PCA is a process that summarises large data sets (Lever et al., 2017) and is

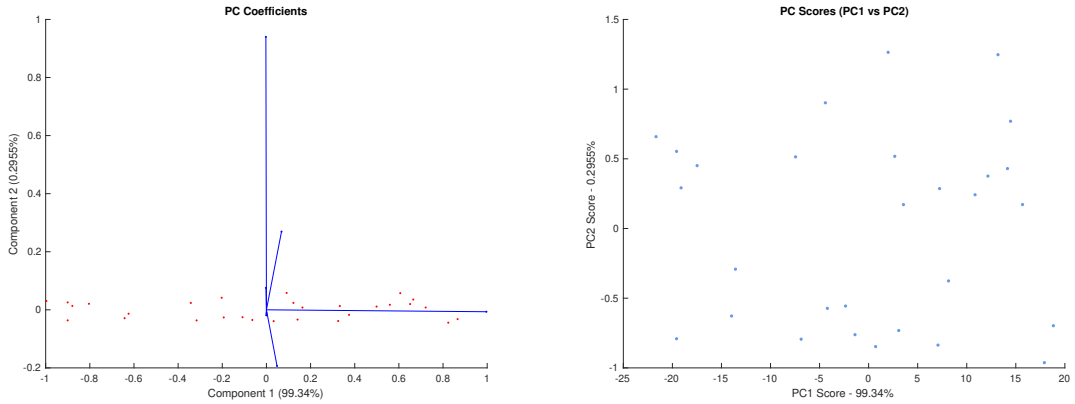

(a) Loading plot.

(b) Score plot.

Fig. 2.7 Principal component analysis loading and score plots of the descriptive morphological values of 29 diaspores.

especially effective when the searched patterns produce an increase in the variance of the projections onto orthogonal components.

Results of the PCA

Descriptive morphological values were collected for all 31 *Alsomitra macrocarpa* and listed in Table A.1, Table A.2, Table A.3 and Table A.4. Table 3.1 later on reports the mean value and the 95% confidence interval for the geometrical characteristics of *Alsomitra macrocarpa*. The 95% confidence intervals are calculated by applying bias-corrected and accelerated bootstrapping as in Cummins et al. (2018). The majority of the morphological data reported in Tables A.1, A.2 and A.3 proved to be normally distributed. Mass, centre of gravity, wing loading, density, fluctuating asymmetry and circularity were not normally distributed. The calculation of confidence intervals, usually requires the assumption that the data analysed are normally distributed. This is not required if the confidence intervals are obtained by bootstrapping. Elliptical Fourier Descriptors (EFD) were extracted from 29 *Alsomitra macrocarpa* with 15 harmonics to describe the planar shape of each specimen. Results produced by EFD were analysed with PCA and reported in figure 2.8 to look at variations in the morphology that could help explain the different flight behaviours. Figure 2.7a and figure 2.8a are loading plots that highlight how strongly each characteristic influences the two principal components. The loading plot in figure 2.7a presents 29 red dots, 29 diaspores provided the 8 morphological values used in the analysis, that led to 8 principal components with a decreasing weight. The blue vectors show how much weight the remaining 6 components have on the 2 selected principal components. Similarly, figure 2.8a

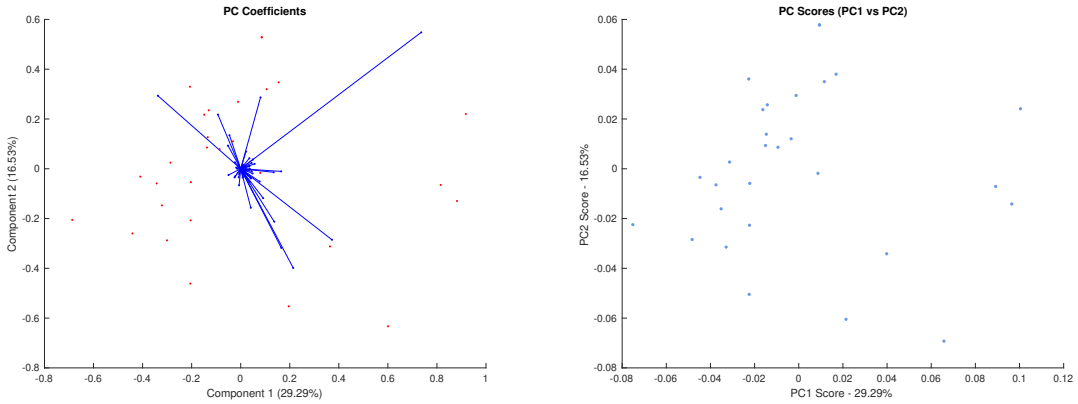

(a) Loading plot.

(b) Score plot.

Fig. 2.8 Principal component analysis loading and score plots of the Elliptical Fourier Descriptors on 29 diaspores.

displays the influence of the remaining 13 Elliptical Fourier Descriptors on the two principal Elliptical Fourier Descriptors. Figure 2.7b and figure 2.8b are score plots, projection of the data in two dimensions defined by the two principal components.

2.3 3D scanner

A diaspore of *Alsomitra macrocarpa* was scanned with a high-resolution 3D scanner, a ROMER absolute arm with Integrated Scanner RS4, as shown in Fig. 2.9. The scanner is made of two cameras and a laser that projects a red line, comprising 7520 points at 100 Hz, on the scanned object. The maximum width of the line is 150 mm, so *Alsomitra macrocarpa* was scanned along the spanwise direction. The single point repeatability is 0.027 mm with a volumetric accuracy (accuracy of multiple scans) of $\pm$0.038 mm. The point cloud generated by the investigated surface is built by the differences in the returned light detected by the two cameras. These values allowed for a detailed, non-destructive, description of the surface of *Alsomitra macrocarpa* and the different cross sections, but not a characterisation of the thickness distribution. The seed containing pericarp is about 1-2 mm thick. The membrane wing, instead presents a thickness distribution spanning from a few µm at the edges, to around 200 µm at the point of maximum thickness, as reported by Azuma and Okuno (1987); Nachtigall (2011b). A Vernier calibre, with an accuracy of 0.001 mm, allowed to measure the thickness on different points of three *Alsomitra macrocarpa*. These measurements were performed to check that the diaspores were representative of the values reported in the literature. The uneven, flexible and transparent surface of *Alsomitra macrocarpa*, posed a challenge.

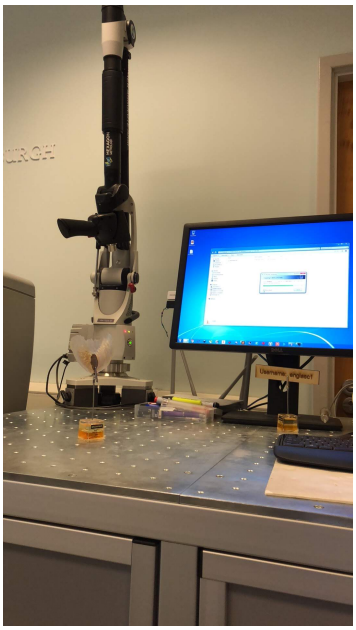

Fig. 2.9 3D scanner setup.

The average density of points on the membrane wing was 396 points/mm^2. Karasik et al. (2018), employed a high resolution 3D scanner to describe and subsequently classify grape pips, they reported a similar average density of points on the surface.

2.4 Visualisation Tunnel

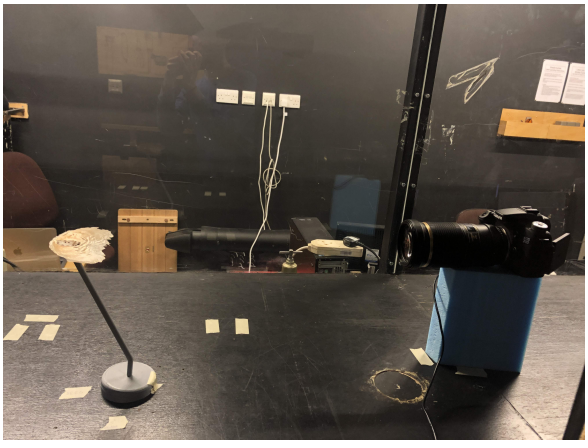

Fig. 2.10 Experimental set-up in the visualisation tunnel to study the deformation of the membrane wing.

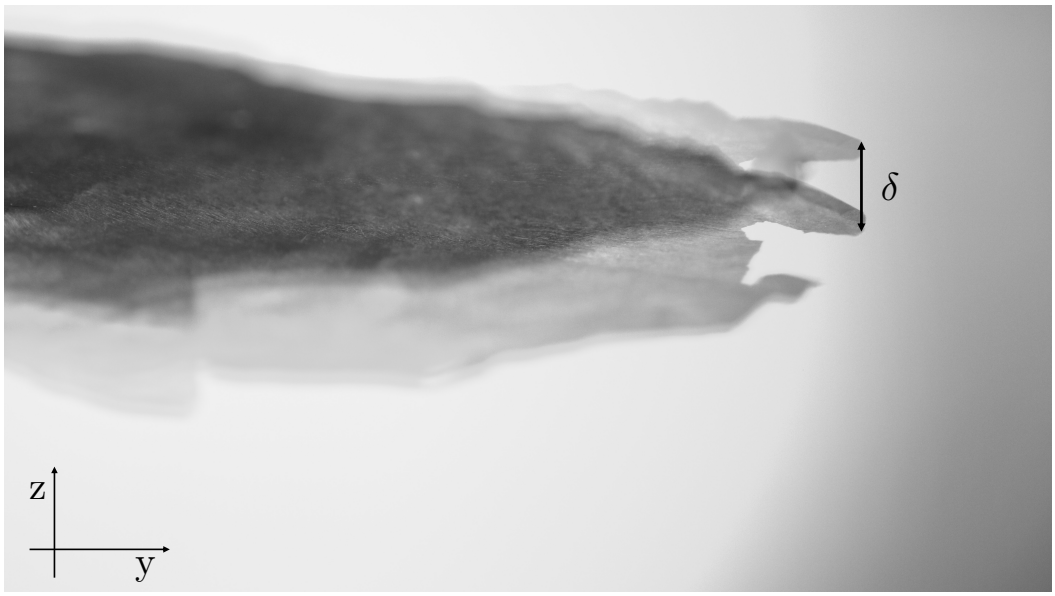

Fig. 2.11 Measurement of wing tip displacement.

The Visualisation Tunnel at the University of Glasgow is a low-speed, closed test section, open circuit wind tunnel, developed and built for flow visualisations (Giuni and Green, 2013). It presents a square, closed test section, with side 0.91 m. *Alsomitra macrocarpa* was mounted on a custom-made support and held in place by magnets, figure 2.10. The Visualisation Tunnel allowed investigation of the deformation of the membrane wing under gliding conditions, with the experimental set-up in figure 2.10. Calibration of the Visualisation Tunnel was performed to link the fan's duty cycle with the free stream velocity in the test section. A DSLR camera (Canon EOS 70D) with a Tamron 180 mm F3.5 SP AF Di Macro Lens, placed eight mean geometric chords downstream of *Alsomitra macrocarpa* took pictures of the wing during the experiment. A settling time of 30 s was interposed between reaching the desired free stream velocity in the test section and taking the pictures. Two separate sets of experiments were performed to investigate the tip deflection of the left and right sides of the wing. The angles of attack studied were 0 deg, 5 deg, 10 deg and 15 deg. The trimmed angle of attack reported by Minami and Azuma (2003) and Azuma and Okuno (1987) is around 12 deg. The free stream velocities tested were $0\,\mathrm{m\,s^{-1}}$, $1.13\,\mathrm{m\,s^{-1}}$, $1.23\,\mathrm{m\,s^{-1}}$, $1.33\,\mathrm{m\,s^{-1}}$, $1.43\,\mathrm{m\,s^{-1}}$, $1.55\,\mathrm{m\,s^{-1}}$, $1.63\,\mathrm{m\,s^{-1}}$ and $2.07\,\mathrm{m\,s^{-1}}$. The range was defined, based on the data available in Azuma and Okuno (1987); Minami and Azuma (2003); Nachtigall (2011a). The test in quiescent conditions described the resting coordinate of the tip. The tip displacement δ was calculated as the difference in the vertical position of the tip between quiescent conditions and vertical position at a free stream velocity, with an accuracy of 0.2 mm, figure 2.11.

(a) Diaspore mounted on the support. (b) Green laser illuminating the wake.

Fig. 2.12 *Alsomitra macrocarpa* in the test section of the Anatomy Wind Tunnel, before and during the PIV test.

2.5 Anatomy Wind Tunnel

This section describes the wind tunnel used to perform Particle Image Velocimetry (PIV) on *Alsomitra macrocarpa*. The set-up in the test section is presented in figure 2.12. The flow structures present in the wake and on the suction side of the membrane wing were investigated.

The Anatomy Wind Tunnel at the University of Glasgow is low-speed, low turbulence, closed-return wind tunnel. It has a rectangular test section of 1.15 m × 0.85 m and a turbulence level of approximately 0.3% (Green et al., 2005). A continuous laser sheet, 2 mm thick, generated by a diode laser of 5 W power at 532 nm created the plane of investigation. The laser was placed at the top of the test section with the laser sheet perpendicular to the free stream flow.

A custom-designed and 3D printed rigid support held *Alsomitra macrocarpa* more than 0.2 m above the test section floor, out of the boundary layer. Two couples of magnets were applied to the seed containing pericarp to keep *Alsomitra macrocarpa* in place during the measurements, without damaging the thin and fragile membrane wing and minimising the disturbance to the airflow. The maximum blockage ratio (ratio between the projected area of *Alsomitra macrocarpa* together with the support rig and the cross-sectional area of the test section) was lower than 0.5%, thus no blockage corrections were made.

2.5.1 Diaspores tested

A randomly selected *Alsomitra macrocapa*, number 17, was tested in the Anatomy Wind Tunnel to get insights on the flow topology around the tip of the membrane wing. This diaspore, as reported in Tables A.1 and A.4, has a mean geometric chord of $m.g.c$ = 57 mm

and a wing-span of b = 166 mm, resulting in an aspect ratio AR = 2.9. The free stream velocity was fixed at $1.5\,\mathrm{m\,s^{-1}}$, in agreement with the average gliding velocity reported in the literature Azuma and Okuno (1987); Nachtigall (2011a). The chord-based Reynolds number was Re = 5790. The diaspore was tested at an angle of attack of 5 deg. The laser sheet illuminated the wake one mean geometric chord downstream of the trailing edge, as shown in figure 2.12b, to avoid reflections from the surface of the wing.

Another randomly selected *Alsomitra macrocapa*, number 14, was painted matt black to reduce the reflections coming from the wing (Muir et al., 2017) and was tested to investigate the flow topology near the wing in the vicinity of the leading edge. This diaspore, as detailed in Tables A.1 and A.4, has a mean geometric chord of $m.g.c.$ = 59 mm and a wing-span of b = 172 mm, resulting in an aspect ratio AR = 2.9. The free stream velocity of the test was the same as the previous test, as was the angle of attack. The chord-based Reynolds number was Re = 5990.

2.5.2 Particle Image Velocimetry

Time-resolved particle image velocimetry (TR-PIV) is implemented to characterise the flow field near the tip and on the suction side of the membrane wing. The set-up used for the measurements was based on a Spectra-Physics Lab-130-10 double-pulsed frequency-doubled Nd:YAG laser for illumination and a Kodak Megaplus ES1.0 digital video camera, with a resolution of 2048 px times 2048 px in triggered double-exposure mode for photography. The laser repetition rate was 10 Hz, and the inter-pulse separation for the laser was set to $125\,\mu$s (for narrow field of view investigation of the flow field between the leading edge and half of the chord on the suction side of the membrane wing) or $150\,\mu$s (for wide field of view investigation of the domain near the tip). Both time intervals between image pairs were selected such that the particle displacement within image pairs was less than 5 px.

The light sheet was delivered into the wind-tunnel working section from above using beam shaping optics, mirrors and a cylindrical lens. The camera was fitted with a Nikkor 50 mm $f/2.8$ lens which was set to $f/4$ during the experiment. The camera was synchronised with the laser to $1\,\mu$s accuracy, with a National Instruments PC-TIO-10 counter timer, and the digital images were captured using a National Instruments PCI-1424 digital image frame grabber. A C. F. Taylor scientific smoke generator generated the seeding needed. It used an electrical heater to vaporise Shell Ondina EL oil and form a fine mist gently pumped in the settling chamber, using carbon dioxide. It was introduced upstream from the test section and circulated for approximately 1 min, until evenly distributed. The oil mist has a nominal particle diameter of $2\,\mu$m and an average density of $1\,\mathrm{kg\,m^{-3}}$. The resulting Stokes number is approximately 9.2×10^{-8}, therefore seeding particles accurately follow the fluid flow.

A calibration plate, located in the same position as the laser sheet was used to get spatial calibration of the PIV system. The narrow field of view produced images with a resolution of $48\,\mathrm{px\,mm^{-1}}$, while the wide field of view had $22\,\mathrm{px\,mm^{-1}}$. The Anatomy Wind Tunnel had been used for studies on rotors Green et al. (2000) and Green et al. (2005).

Analysis of the collected images was undertaken using the LaVision software (DaVis 8.4, LaVision Inc.) and a multipass cross-correlation algorithm. A Fast Fourier Transform (FFT) algorithm with a window size of 96 px times 96 px and 50 % overlap was applied. This analysis was subsequently refined with three passes at 48 px times 48 px of window size and 75 % overlap. Results presented in this thesis are averages of over 100 image pairs.

2.5.3 Vortex identification

The boundary of the identified vortex was defined using swirling strength λ_{ci} (Zhou et al., 1999). Swirling strength, λ_{ci} is based on the concept that the velocity gradient tensor, in Cartesian coordinates, can be decomposed as follows:

$$\frac{\partial u_j}{\partial x_i} = \left[d_{ij}\right] = \left[\bar{v}_r \bar{v}_{cr} \bar{v}_{ci}\right] \begin{bmatrix} \lambda_r & 0 & 0 \\ 0 & \lambda_{cr} & \lambda_{ci} \\ 0 & -\lambda_{ci} & \lambda_{cr} \end{bmatrix} \left[\bar{v}_r \bar{v}_{cr} \bar{v}_{ci}\right]^T \tag{2.2}$$

where λ_r is the real eigenvalue with corresponding eigenvector $\bar{v}_r$ and the complex conjugate pair of complex eigenvalues is $\lambda_{cr} \pm i\lambda_{ci}$ with corresponding eigenvectors $\bar{v}_{cr} \pm i\bar{v}_{ci}$. By expressing the local streamlines in a coordinate system spanned by the three vectors ($\bar{v}_r$, $\bar{v}_{cr}$, $\bar{v}_{ci}$) we can see that the local flow is either stretched or compressed along the axis $\bar{v}_r$ while on the plane spanned by the vectors $\bar{v}_{cr}$ and $\bar{v}_{ci}$ the flow is swirling. The strength of this swirling motion can be quantified by λ_{ci}, called the local swirling strength of the vortex. Onoue and Breuer (2016), Ōtomo et al. (2021) and Wilroy et al. (2018) have successfully employed this method to define coherent vortices in PIV data. Each vortex is considered as the centroid of its circulation distribution.

2.6 Emission

A collaboration with Dr Taani, from King's College London, was established to measure the emission spectrum of a diaspore. This test campaign was carried out to check if the light emitted by the seed containing pericarp and the membrane wing of *Alsomitra macrocarpa* was at the same wavelength as the incident light. The emission spectrum of the seed containing pericarp and of the membrane wing were investigated in two separate experiments. A JASCO

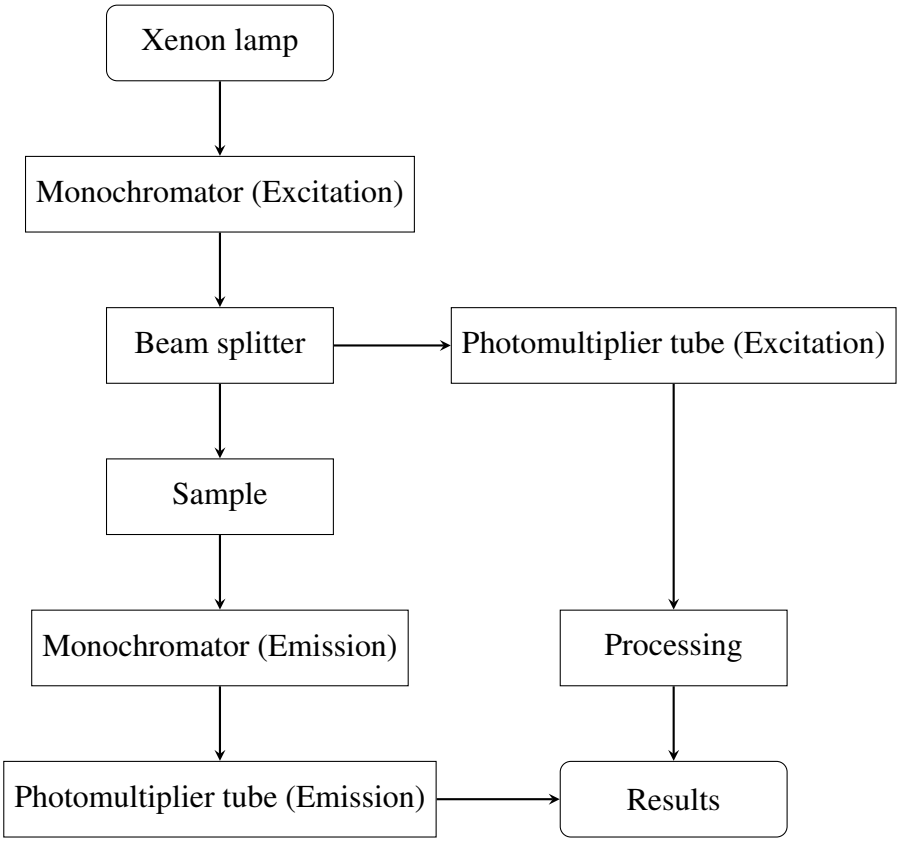

Fig. 2.13 A schematic diagram of an emission spectrum measurement diagram.

FP-6500 spectrofluorometer, which emits and measures light of precise wavelengths, was used for the measurements. A diagram of the setup is presented in figure 2.13. A Xenon lamp emits light which is then filtered by a monochromator that selects the wavelength of interest. A beam splitter subsequently splits the light, hence the intensity of the incident light can be measured. The light then hits the wavelength shifting sample, either the seed containing pericarp or the membrane wing, in our experiments. Light is absorbed and fluorescent light is emitted. The emitted light goes through a monochromator and its intensity is measured by a photomultiplier tube. This setup allowed to determine the emission spectrum for different wavelengths of the incident light, among whom lies the wavelength emitted by the Azure Kinect depth cameras to define the distance of the object from the camera.

2.7 Flight experiments

Alsomitra macrocarpa gently glides in the tropical Asian forests, trading the height where the parent pod rests, hence the potential energy, for horizontal displacement. The problem of detecting and tracking flying birds, insects and objects has been studied by various research groups, trying to answer different research questions. Tracking the flight of seeds, pieces of paper and insects with Azure Kinect DK depth cameras is an interesting investigation method, because it requires no manipulation of the investigated subject, provides high spatial resolution and can be quickly implemented in a laboratory. The raw data define the position in space, these measurements can be further analysed, providing values for velocity and acceleration (Hedrick, 2008). Two-dimensional video analysis is implemented in Biology and Fluid Mechanics to study the flight of seeds like maple seeds (Varshney et al., 2011), dandelions (Casseau et al., 2015; Cummins et al., 2018) and dispersal units of *Zelkova abelicea* (Certini et al., 2020). Photogrammetry and video analysis gather information from two or more cameras to extract coordinates in three dimensions.

2.7.1 Drop test

When an *Alsomitra macrocarpa* takes off from its parent pod, containing up to 400 individual seeds (BBC, 2009), it usually performs a helical path (table B.2 and table B.3), rather than a straight path (table B.1) or a curved path, but with a large (i.e. a few meters) radius of curvature (Azuma and Okuno, 1987). Simple drop tests of hand-held seeds allowed to get an idea of the different flight behaviour and extent of the transient of the 31 *Alsomitra macrocarpa* available. Drop tests performed on *Alsomitra macrocarpa* and detailed in the literature (Azuma and Okuno, 1987; Nachtigall, 2011a; Saito et al., 2008)

(a) Back view of set-up for straight flight.

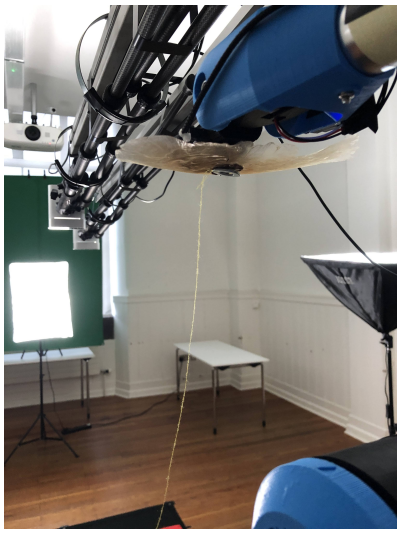

(b) Release mechanism.

(c) Front view of set-up for straight flight.

(d) Back view of set-up for helical flight.

Fig. 2.14 The experimental apparatus; two depth cameras, a robotic arm, *Alsomitra macrocarpa*, three soft-boxes (pyramid-shaped light diffusers), a black curtain and a desktop.

gave further details on how to design the experimental set-up. These drop tests were also performed with *Alsomitra macrocarpa* taking off from 4 different initial orientations. Starting from the horizontal position, where *Alsomitra macrocarpa* is parallel to the ground, the other three initial positions were achieved by turning *Alsomitra macrocarpa* by 90°. After a short transient, less than 5 *m.g.c.* in the vertical direction, all the diaspores reached their gliding position and landed on the same side of the seed-containing pericarp. The majority, 27 exhibited helical gliding, while the remaining ones (i.e. 4) had a straight trajectory. These observations agreed with the experiments of Azuma and Okuno (1987) who tested 10 seeds and 3 flew in front of the camera used for the drop test. McCutchen (1977) reported that *Zanonia* samaras, old taxonomic denomination for *Alsomitra macrocarpa*, fly in circles, a meter or less in diameter, and a minority glides in a straight path. The free flights of 15 *Alsomitra macrocarpa* were investigated using the experimental set-ups in figure 2.14. The collected data allowed to confirm the results about the diaspores expected to fly straight or in a helical path. Two Azure Kinect depth cameras facing the ground recorded the flight in a closed room of 5.5 m in width, 9.0 m in length and 3.0 m in height, in still air conditions. A thermal hot-wire anemometer (Testo 405-V1 (Lentink et al., 2009)) measured air temperature and flow speed before the flight of each *Alsomitra macrocarpa*. The range of temperatures recorded during the glides was 16.9 °C to 20.3 °C, hence air density was considered constant and convection negligible as stated by Vogel (1996). The range of flow speeds measured was $0.01\,\mathrm{m\,s^{-1}}$ to $0.02\,\mathrm{m\,s^{-1}}$. Two different release positions, hence two different locations of the robot arm (figure 2.14c and figure 2.14d) were used as release points depending on the flight path. The height of the release point was kept constant at 1.74 m. The planar position, with respect to the cameras, was changed to maximise the portion of the flight path falling into the investigated volume. Each *Alsomitra macrocarpa* performed at least 5 glides, so 5 technical repeats minimum. The seeds were held in place by a Nyrio One robotic arm with an electromagnet and a metal disk pressing on the seed containing pericarp, the only rigid part of *Alsomitra macrocarpa*. The robot arm with the metal disk pressing against the seed containing pericarp is pictured in figure 2.14b. A vacuum pump gripper was tested as an alternative. It produced enough suction force to counteract the average weight of the seeds (0.003 N), but the uneven surface of the seed containing pericarp did not allow its deployment. The set-up, controlled by two personal computers, was operated remotely to minimise the disturbances (Vincent et al., 2020a). All seeds were released from a horizontal position, with zero translational or angular velocity (Vincent et al., 2020a). The gliding path was captured using two Azure Kinect depth cameras facing the ground, in order to increase the camera coverage of the glide. The orientation of the two depth cameras was changed according to the gliding path of the diaspore. The data were captured at 30 fps

with a resolution of 3840 px times 2160 px for the RGB camera and 640 px times 576 px for the depth camera. A sampling rate of 30 fps is enough to capture events happening at a frequency lower than 15 fps, according to the Nyquist–Shannon sampling theorem (Shannon, 1949). The comparison between two videos of the same flight of one seed, recorded at 15 fps and 60 fps with a camera proved that 15 fps was sufficient to capture the dynamics of the glide. The volume investigated was around $6\,\mathrm{m}^3$. A custom made Matlab script, that worked with the combined data of the two depth cameras, extracted the instantaneous x, y and z coordinates of the position of *Alsomitra macrocarpa* during the glide, the velocity u, v, w and acceleration a_x, a_y, a_z components. The vertical distance covered during the glide was 1.74 m. After the release, *Alsomitra macrocarpa* goes through a quick transient, followed by the periodic motion that it experiences during the glide. The transient, in all cases, ended within 0.3 m of the fall.

2.7.2 The Azure Kinect DK sensor

Two Azure Kinect DK sensors tracked the different gliding flights of 15 *Alsomitra macrocarpa*. Each Kinect sensor combines a depth sensor, a spatial microphone array, with a video camera and an orientation sensor that provides the reference system. The Azure Kinect DK sensor comprises two different cameras: a 3D range sensor, called a depth camera and a monocular colour camera, called RGB camera (Microsoft, 2019; Nakamura, 2011). The depth camera has an infrared laser projector combined with a manochrome CMOS sensor developped by Nakamura (2011). It implements the Amplitude Modulated Continuous Wave (AMCW) Time-of-Flight (ToF) principle. The camera projects a modulated illumination in the near infrared (NIR) onto the investigated scene. It then measures the time it takes to the light to travel from the source (i.e. the camera) to the scene and back. This measurement allows to build a depth map, a three dimensional representation of the scene. The depth map is a set of z-coordinate values linked to every pixel in the image, the x and y-coordinate of the scene. Millimetres is the SI unit applied by the sensor. A clean infrared reading is a byproduct of the depth map. A clean infrared reading is a 2D image where the intensity of the pixels is proportional to the amount of light returned by each pixel in the 2D scene. Some relevant technical characteristics of the depth camera, reported in (Microsoft, 2019) are:

- 1-Megapixel ToF imaging chipwith advanced pixel technology enabling higher modulation frequencies and depth precision;
- two NIR Laser diodes enabling near and wide field-of-view (FoV) depth modes;
- the world's smallest ToF pixel, at $3.5\,\mu$m by $3.5\,\mu$m;

- automatic per pixel gain selection enabling large dynamic range allowing near and far objects to be captured cleanly;
- global shutter that allows for improved performance in sunlight;
- multi-phase depth calculation method that enables robust accuracy even in the presence of chip, laser, and power supply variation;
- systematic and random errors are low.

The raw modulated infrared images captured by the depth cameras were transferred to the host PC. An HP EliteDesk 800 G4 TWR running Windows 10, with 8th Generation Intel Core i7 Processor and 32.0 GB of RAM was exploited. The GPU accelerated depth engine software of the PC converts the raw signal into depth maps. The depth camera of the Azure Kinect DK sensor supports several modes. The narrow field of view (FoV) modes are applied to scenes where two dimensions, given the reference system linked to the sensor, x and y, are smaller than the z coordinate Microsoft (2019). On the contrary, when the scene has large x and y coordinate values, but smaller z coordinate ranges, the wide FoV modes are better suited. All glides of *Alsomitra macrocarpa* were recorded with the narrow field of view. It proved to give a better resolution of the flight in preliminary tests. The depth camera supports 2×2 binning modes to extend the z-range in comparison to the corresponding unbinned modes. The binning mode lowers the image resolution. All modes presented, narrow field of view binned and unbinned, wide field of view binned and unbinned, can record at a maximum of 30 fps, with the exception of the 1 Mpx mode which records at a maximum frame rate of 15 fps. The depth camera also has a passive infrared mode. The infrared mode disallows the source of infrared light and the only source of illumination is ambient light.

Camera errors in static conditions

The camera's performance was assessed in static conditions, where it is tracking a static scene. Two types of errors were identified: systematic and random errors.

Systematic error The systematic error is the difference between the measured depth after noise removal and the real (ground truth) depth. The position of the black carpet, lying 1787 mm under the depth camera, was utilised to quantify the systematic error in the experiments.

The computation of the temporal average over many frames of a static scene defines the depth noise caused by the systematic error. Systematic error is defined as:

$$E_{\text{systematic}} = \frac{\sum_{t=1}^{N} d_t}{N} - d_{gt} \tag{2.3}$$

Where d_t is the measured depth at time t, N is the total number of frames used to calculate the average, $N = 10$ in this analysis, and d_{gt} is the ground truth depth, $d_{gt} = 1787\,\text{mm}$. The depth camera's systematic error in our experiments was less than 1 mm, hence considered negligible. This calculation of the systematic error does not take into account multi-path interference (MPI). Multi-path interference is mitigated by the depth camera using higher modulation frequencies, coupled with depth invalidation.

Random error The depth of the investigated scene is slightly different in each of the 30 images acquired in a second. This subtle difference is caused by the so-called shot noise. Shot noise is defined as the total number of photons that reach the sensor, it varies by a random factor over time. The random error is described in Microsoft (2019), as the standard deviation of the measured depth, a function of time, over a static scene.

$$E_{\text{random}} = \sqrt{\frac{\sum_{t=1}^{N} \left(d_t - \bar{d}\right)^2}{N}} \tag{2.4}$$

In the above equation, N represents the total number of depth measurements, $N = 10$ in this evaluation, d_t the depth measurement at time t and $\bar{d}$ the mean value computed over all depth measurements d_t. The random error in the data collected was around 1 mm.

2.7.3 Invalidation

The depth camera, under certain conditions, light conditions, for example, may not provide the right depth values for some pixels composing the scene. Related pixels, as a consequence, are invalidated and the corresponding depth values are assigned to zero. There are various reasons why the depth engine might be incapable of assigning the right depth, some include:

- multi-path interference;
- the investigated object is outside of the active infrared illumination;
- the infrared signal is either saturated or low.

Pixels are invalidated when they belong to a part of the scene which is outside of the active infrared illumination mask. The edges of *Alsomitra macrocarpa*, during sections of the glide,

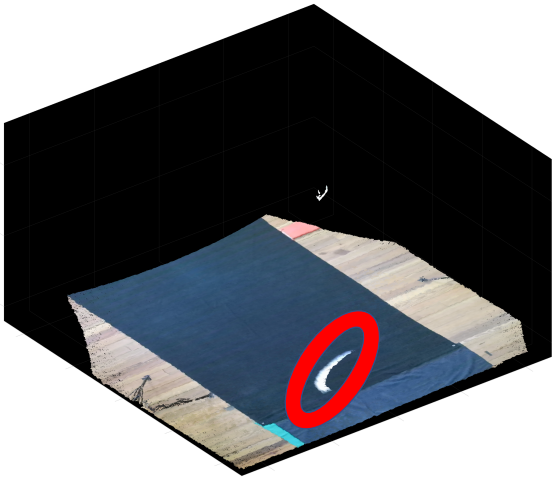

Fig. 2.15 The invalidated pixels, belong to *Alsomitra macrocarpa* and are highlighted with a red ellipse.

were affected by invalidation. Figure 2.15 shows the result of the invalidation due to the illumination mask. Some invalidated pixels are plotted as black-colour pixels outside of the hexagon in the narrow field of view mode.

The strength of the infrared signal is also a cause for pixel invalidation. Saturated pixels are invalidated because the phase information is lost. Invalidation can also occur when the infrared signal is not strong enough to generate a depth value. A source of ambiguous depth that leads to pixel invalidation is when a pixel receives the depth signal from more than one object in the scene. This happens at the edges of objects, where pixels can contain mixed signals from foreground and background (see Figure 2.15). This phenomenon is known as the flying pixel problem Tölgyessy et al. (2021). The reflected light causes ambiguity in the depth assigned to the pixels, but filters implemented in the depth algorithm (Microsoft, 2019) detect this issue and invalidate the pixels. The use of multiple Azure Kinect DK sensors can be an approach to tackle this problem if the sensors investigate the same scene from different perspectives as in our set-up. Object edges are a source of multipath interference because they tend to contain a mixed signal of foreground and background. Fast motion is a common cause of invalidated pixels around the edges.

The coordinate system

Depth and colour cameras have an independent 2D coordinate system. The *x*-*y* coordinate system has units of pixels, with *x* and *y* ranging between 0 and 1. The pixel coordinate

$[0,0]$ represents the top-left pixel of the image. Sub-pixel coordinates are shown as fractions. The 2D coordinate system is centred in zero, while the sub-pixel coordinate of the centre is $[0.0,0.0]$. The depth and RGB cameras present an independent 3D coordinate system. Every point in the 3D coordinate system has a triplet of coordinates $[x,y,z]$ with units in millimetres. The origin $[0,0,0]$ is located at the focal point of each camera. The orientation of the coordinate system is fixed: the positive x-axis points right, the positive y-axis points down and the positive z-axis points forward. The fixed orientation of the coordinate system, together with the position of the Azure Kinect cameras required geometrical transformations during the post-processing. Every Azure Kinect camera is calibrated, but a calibration was required to merge the two point clouds. A point cloud is a set of data points in a volume and it describes three-dimensional objects. Each point of a point cloud is represented by an x, y, and z geometric coordinate.

2.8 Analysis of a glider performance

In this section we describe the two non-dimensional parameters that characterise the gliding flight: aspect ratio AR and Reynolds number *Re*. Section 2.8.1 and 2.8.2 are a detailed analysis of the gliding flight (Ennos, 1989), while section 2.8.3 applies this knowledge to *Alsomitra macrocarpa*. The gliders that fly up in the sky have high aspect ratio wings, sometimes over 50, like the Eta glider. The aspect ratio (AR) is a dimensionless parameter defined as:

$$AR = \frac{b^2}{S}\ , \tag{2.5}$$

where b is the wingspan, the distance between the wing tips and S is the planform area of the wing, as seen from above. *Alsomitra macrocarpa*, an incredible gliding diaspore has a low aspect ratio, as reported in table 3.1. Man-manned gliders fly at a Reynolds number over 10^6, while the Reynolds number of gliding seeds is of the order of 10^3. The Reynolds number is a non-dimensional parameter describing the relative importance of inertial and viscous forces in a fluid. It is expressed by:

$$Re = \frac{Uc}{\nu}\ , \tag{2.6}$$

where U is the velocity of the body, c a characteristic length and ν the kinematic viscosity. *Alsomitra macrocarpa* has a flight speed of $1.12\,\mathrm{m\,s^{-1}}$ and a wing chord at the wing centre of 70 mm, so its *Re* is approximately 5000. Table 2.1 records the flight characteristics of the four *Alsomitra macrocarpa* that flew in a straight glide. In this section, we will examine how

Table 2.1 Mean value and 95% Confidence interval of flight characteristics of four *Alsomitra macrocarpa*.

	Mean value	95% Confidence interval
Terminal velocity, w [$\mathrm{m\,s^{-1}}$]	0.41	0.38 to 0.45
Velocity, U [$\mathrm{m\,s^{-1}}$]	1.12	0.97 to 1.29
Glide angle, γ [deg]	23	21 to 25

the aspect ratio, a geometric parameter that describes the planar shape of a wing, affects flight performance and show the reason for different aspect ratios at different Reynolds numbers.

Rewriting the calculations in Ennos (1989), we find that the drag which opposes the motion of a glider on a plane consists of two components. The frictional component, the profile drag, D_{pro}, is (Alexander, 1982):

$$D_{\mathrm{pro}} = \frac{1}{2}\rho U^2 S C_{D\mathrm{pro}} \,, \tag{2.7}$$

where ρ is the fluid density and $C_{D\mathrm{pro}}$ is the profile drag coefficient. Profile drag is defined as the sum of form drag and skin friction. The induced drag D_{ind} is related to the production of lift, so it is a property of streamlined bodies and is approximately (Alexander, 1982):

$$D_{\mathrm{ind}} = \frac{(mg)^2}{2\rho U^2 S\ \mathrm{AR}} \,, \tag{2.8}$$

where m is the mass of the glider and g is the acceleration due to gravity. Lift (L) generated by a streamlined body is equal to or close to the weight $W = mg$ during a cruise flight or a low gliding angle (Alexander, 1982). The spanwise lift distribution is assumed to be elliptical and $L = \frac{1}{2}\rho U^2 S C_L$. The total drag ($D$) on a glider is the sum of the profile (D_{pro}) and induced drag (D_{ind}). It can be expressed as:

$$D = \frac{1}{2}\rho U^2 S C_{D\mathrm{pro}} + \frac{(mg)^2}{2\rho U^2 S\,\mathrm{AR}} \,, \tag{2.9}$$

At low speeds, induced drag dominates, while at high speeds, profile drag dominates.

Total power, plotted in figure 2.16, is the product of force time velocity:

$$P = \frac{1}{2}\rho U^3 S C_{D\mathrm{pro}} + \frac{(mg)^2}{2\rho U S\,\mathrm{AR}} \,, \tag{2.10}$$

Differentiating the last two equations (2.9) and (2.10) with respect to U it is possible to

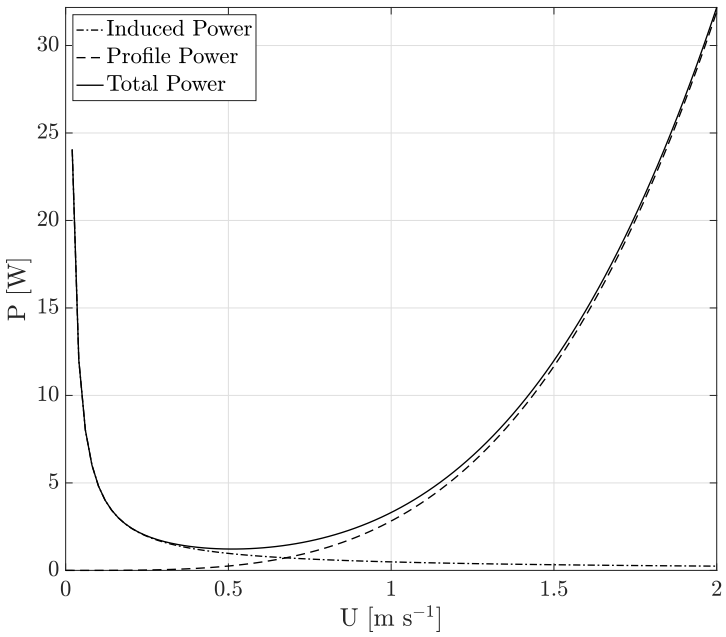

Fig. 2.16 Total power is the sum of profile power and induced power as expressed in equation 2.10.

derive the expressions for the minimum drag speed (U_3), at which a glider achieves its shallowest glide angle (γ) and the minimum power speed (U_2) that minimises the rate of sink. While U_3 maximises the horizontal distance travelled for a unit vertical height loss, U_2 maximises the time spent in the air for a unit vertical height loss. It is also known as the flight path angle, the angle between the velocity vector and the horizontal plane. The minimum drag speed is

$$U_3 = \left(\frac{N^2}{\rho^2 AR C_{D\text{pro}}} \right)^{1/4} , \tag{2.11}$$

where N is the wing loading mg/S. Flying at U_3 gives $D_{\text{pro}} = D_{\text{ind}}$. When the glide angle is minimised the horizontal distance, x is maximised:

$$\left| \frac{\partial x}{\partial h} \right| = \frac{1}{|\gamma|} = E = \frac{L}{D} , \tag{2.12}$$

here h is the vertical distance. Assuming γ small, so that $\cos(\gamma) \approx 1$ and $\sin(\gamma) \approx \gamma$. E is the efficiency and it is the ratio of lift (L) and drag (D). The minimum power speed (U_2) is

obtained from the first derivative of the total power P, equation 2.10, with respect to U:

$$U_2 = \left(\frac{N^2}{3\rho^2 \mathrm{AR} C_{D\mathrm{pro}}} \right)^{1/4} = 0.75 U_3 \ , \tag{2.13}$$

It minimises the rate of sink, maximising the time spent in the air, hence the ability to use updrafts and wind to be carried around.

$$\left| \frac{\partial t}{\partial h} \right| = \frac{1}{|U\gamma|} = \left| \frac{W}{UD} \right| , \tag{2.14}$$

Gliders with high wing loading N will therefore have high optimal flight speeds. Higher aspect ratio wings will provide lower optimal flight speeds. At the minimum drag speed (U_3) profile drag equals induced drag and the minimum glide angle $(\gamma_{\min})$ is:

$$\sin(\gamma_{\min}) = \left(\frac{C_{D\mathrm{pro}}}{\mathrm{AR}} \right)^{1/2} , \tag{2.15}$$

Gliders with higher aspect ratio wings, like those we see sailing the skies, possess a better glide performance, achieved at a low speed.

2.8.1 Minimum flight speed

The previous discussion assumes that the glider is capable of flying at the minimum drag and power speeds (Ennos, 1989). A free body diagram, displayed in figure 2.19, highlights the forces involved.

$$L = mg = \frac{1}{2} \rho U^2 S C_L \ , \tag{2.16}$$

Hence the minimum flight speed ($U_{\min}$) is:

$$U_{\min} = \left(\frac{2N}{\rho C_{L\max}} \right)^{1/2} . \tag{2.17}$$

equation 2.17 shows that there is a minimum velocity U_{min}, which depends on the maximum lift coefficient C_{Lmax} as proven in Ennos (1989). According to Ennos (1989) the minimum flight speed U_{min} rises with the wing loading N. The minimum drag speed is reachable if and only if it is higher than the minimum flight speed (Ennos, 1989), so $U_{\min} < U_3$ gives:

$$\mathrm{AR} < \frac{C_{L\max}^2}{4 C_{D\mathrm{pro}}} . \tag{2.18}$$

The aspect ratio appears to have an upper bound. It is low for small gliders, like wind-dispersed seeds, because they operate at low Reynolds numbers where the profile drag is the main source of drag.

2.8.2 Why do gliding seeds have a low aspect ratio?

Small gliders like *Alsomitra macrocarpa* experience a Reynolds number of the order of a few thousand during their flight. The friction drag at such Reynolds numbers is much greater than the pressure drag, the profile drag coefficient decreases with the Reynolds number (Vogel, 1996). For aerofoils, operating at a Reynolds number of less than a few thousand, the profile drag coefficient can be approximated by Ellington (1984) formula:

$$C_{D\text{pro}} = \frac{7}{Re^{1/2}} \tag{2.19}$$

The Reynolds number is

$$Re = \left(\frac{2mg}{\rho S C_L}\right)^{1/2} \frac{c}{\nu} = \left(\frac{2mg}{\rho C_L \nu^2 \mathrm{AR}}\right)^{1/2} \tag{2.20}$$

where c is the mean chord. The drag coefficient is

$$C_{D\text{pro}} = 7\left(\frac{\rho C_L \nu^2 AR}{2mg}\right)^{1/4}, \tag{2.21}$$

and the profile drag is:

$$D_{\text{pro}} = 7\left(\frac{mg}{C_L}\right)^{3/4}\left(\frac{\rho \nu^2 \mathrm{AR}}{2}\right)^{1/4} \tag{2.22}$$

i.e. the profile drag increases with aspect ratio to the power of one-quarter. The induced drag is (Ennos, 1989)

$$D_{\text{ind}} = \frac{(mg)^2}{2\rho S U^2 \mathrm{AR}} = \frac{mgC_L}{4\,\mathrm{AR}}, \tag{2.23}$$

when a glider operates at a fixed C_L, D_{ind} if fixed. The minimum glide angle is achieved with maximum efficiency $E = L/D = C_L/C_D$. When flying at a constant C_L, it will be achieved when the total drag ($D_{\text{pro}} + D_{\text{ind}}$) is minimised and the differential of drag with respect to the aspect ratio equals zero (Ennos, 1989; Torenbeek and Wittenberg, 2009). This happens when the profile drag is equal to four times the induced drag

$$D_{\text{pro}} = 4D_{\text{ind}}, \tag{2.24}$$

and the aspect ratio is

$$AR = 0.20 C_L^{7/5} \left(\frac{2mg}{\rho v^2} \right)^{1/5} \tag{2.25}$$

The total drag is five times the induced drag and the minimum glide angle at this speed becomes:

$$\sin(\gamma) = 5.93 C_L^{-2/5} \left(\frac{\rho v^2}{2mg} \right)^{1/5} \tag{2.26}$$

Therefore, Ennos (1989) has shown that the shape and performance of the gliders depend on the lift coefficient. The higher the lift coefficients, the lower the speed to generate enough lift and the higher the aspect ratio shallower glides can be achieved. Stall sets an upper limit on the lift coefficient that can be produced by an airfoil. The optimum aspect ratio increases and the best glide angle decreases with increasing mass.

2.8.3 Shape and flight of *Alsomitra macrocarpa*

Ennos (1989) proved that gliding seeds do not need a high aspect ratio, differently from planes and man-manned gliders. Figure 2.18a highlights that the glide angle γ changes with the aspect ratio AR and a minimum is reached for AR $\simeq 4.3$, close to the value reported in table 3.1 and listed in the literature (Azuma and Okuno, 1987; Minami and Azuma, 2003). Around a similar value of the aspect ratio, the vertical component of velocity w is close to its minimum, figure 2.18b. When AR ≥ 6.0, the vertical component of velocity is almost constant, the plot in figure 2.18b shows that there would not be any significant reduction of w further increasing AR. Below the aspect ratio indicated by equation (2.18), the glider is able to fly at the minimum drag speed (U_3), reaching its minimum glide angle ($\gamma_{\min}$) (Ennos, 1989). *Alsomitra macrocarpa* flies at $U = 1.12\,\mathrm{m\,s^{-1}}$ (Azuma and Okuno, 1987), it is double the value of minimum drag speed, which minimises the glide angle reported in table 2.2. The plot in figure 2.17a displays that the minimum glide angle ($\gamma \simeq 14$) is reached when the angle of attack α is approximately 5 deg. The terminal velocity provided by the experiments with depth cameras, $0.53\,\mathrm{m\,s^{-1}}$, similar to the value of $0.41\,\mathrm{m\,s^{-1}}$ presented by (Azuma and Okuno, 1987) and points at an angle of attack lower than 5 deg , figure2.17b. The glide angle measured by (Azuma and Okuno, 1987) is 21 deg, slightly bigger than the minimum glide angle that would maximise the distance covered. The profile drag is more than four times higher than the induced drag, because of the low Reynolds. *Alsomitra macrocarpa*, *Ulmus glabra*, *Parthenos Sylvia* and *Neptis sappho* are examples of small natural gliding seeds and insects with large, low aspect ratio wings, which optimise their glide performance over a range of speeds due to the environment and the natural variation. The simplest design is an equivalent flat plate which keeps the mean wing span, surface and aspect ratio listed in

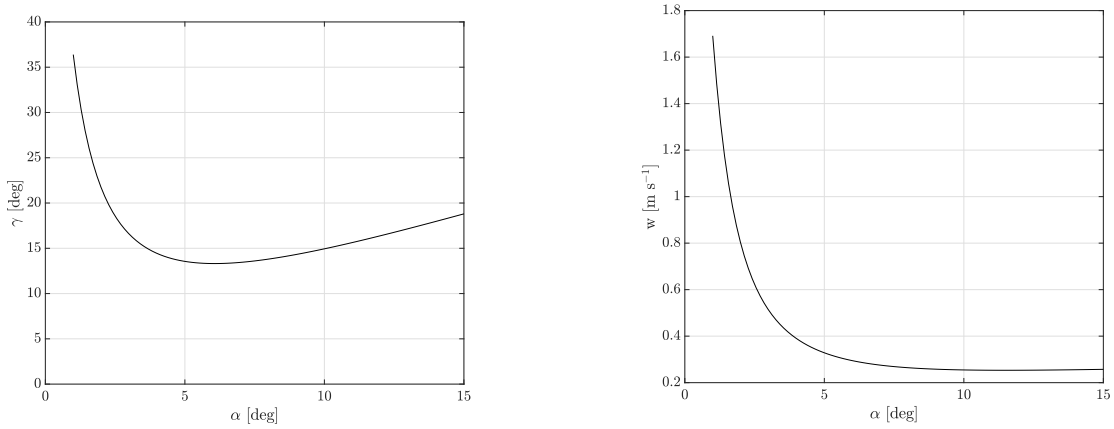

(a) Glide angle γ versus angle of attack α.

(b) Velocity w versus angle of attack α.

Fig. 2.17 Two graphs showing the influence of the angle of attack α on glide angle γ and vertical component of velocity w.

table 3.1 of the studied population (n=24). This shape gives aerodynamic coefficients and dependence on the angle of attack similar to that of the artificial model tested in the wind tunnel by Minami and Azuma (2003). A flat plate has the aerodynamic centre at a quarter of the chord from the leading edge, hence in front of the centre of gravity which coincides with the centroid, making it an unstable configuration. This lack of pitching stability is key to excluding this design because stability is as essential to flying, as lift itself. To get stability we will introduce the sweep angle which moves the wing backwards, hence the centroid in front of the aerodynamic centre. The planform of *Alsomitra macrocarpa* presented sweep angle, listed in table 3.1. The location of the centre of mass, instead, is related to the position of the seed-containing pericarp, where the mass is concentrated. The location of the centre of mass was defined with a static test conducted on the 31 diaspores available. Each *Alsomitra macrocarpa* was balanced on a 3D printed cylindrical support with a radius of 2 mm and the centre of mass was always located in the seed containing pericarp.

2.9 Aerodynamic coefficients of *Alsomitra macrocarpa*

The lift coefficient C_L, drag coefficient C_D and the efficiency $E = C_L/C_D$ reported by Azuma and Okuno (1987) are the results of drop tests and describe the 3D wing. These coefficients can be obtained by solving the equations that describe a steady symmetric glide as reported in the free body diagram of figure 2.19. The lift coefficient is defined by:

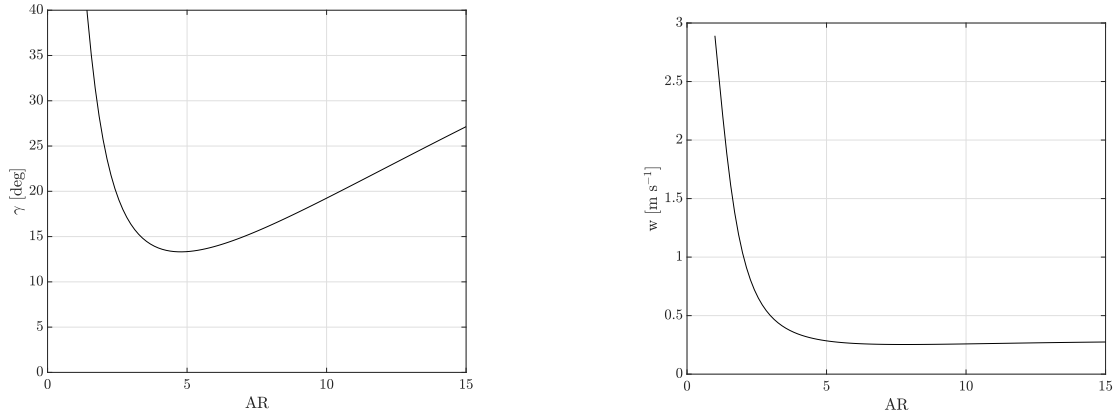

(a) Glide angle γ versus aspect ratio AR.

(b) Velocity w versus aspect ratio AR.

Fig. 2.18 Two graphs showing the influence of the aspect ratio AR on glide angle γ and vertical component of velocity w

Table 2.2 Optimal performance of *Alsomitra macrocarpa*.

Lift coefficient	0.425
Drag coefficient	0.163
Efficiency	2.61
Reynolds number	5336
$C_{L\max}$ airfoil (Azuma and Okuno, 1987)	1.19
Minimum drag speed, $[\mathrm{m\,s^{-1}}]$	0.52
Minimum rate of sink, $[\mathrm{m\,s^{-1}}]$	0.39
Minimum flight speed, $[\mathrm{m\,s^{-1}}]$	0.69
Minimum glide angle, [deg]	20

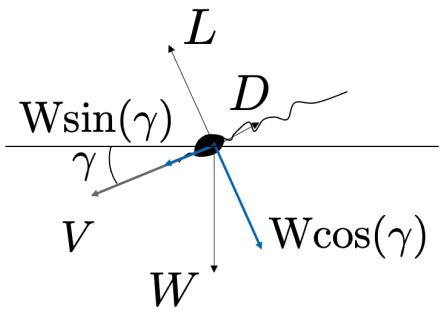

Fig. 2.19 Free body diagram of *Alsomitra macrocarpa* in trimmed gliding.

$$C_L = \frac{2\cos(\gamma)}{\rho V^2}\frac{W}{S}, \tag{2.27}$$

and the drag coefficient:

$$C_D = \frac{2\sin(\gamma)}{\rho V^2}\frac{W}{S}, \tag{2.28}$$

where the air density (ρ) is assumed to be $1.225\,\mathrm{kg\,m^{-3}}$, while the wing loading (W/S) and the flight speed (V) are given in Azuma and Okuno (1987). The gliding angle γ, being the angle between the plane of the horizon and the path of *Alsomitra macrocarpa*, is calculated:

$$\gamma = \arctan(1/E) \tag{2.29}$$

The angle of attack α is the angle between the horizontal component of velocity and the flight speed V (total velocity), it can be written as:

$$\alpha = \arcsin(w/V) \tag{2.30}$$

Where w is the terminal velocity, the vertical component.

2.10 Theoretical analysis

The lift coefficient (C_L) for low aspect ratio ($AR < 4$) swept wings (Λ, sweep angle at half of the chord line) with an elliptical lift distribution in incompressible flow, is predicted by the

following equation Anderson Jr (2010):

$$C_L = \frac{2\pi\cos(\Lambda)}{\sqrt{1+[(2\pi\cos(\Lambda))/(\pi AR)]^2}+[2\pi\cos(\Lambda)/(\pi AR)]}\alpha \tag{2.31}$$

and plotted in figure 2.20.

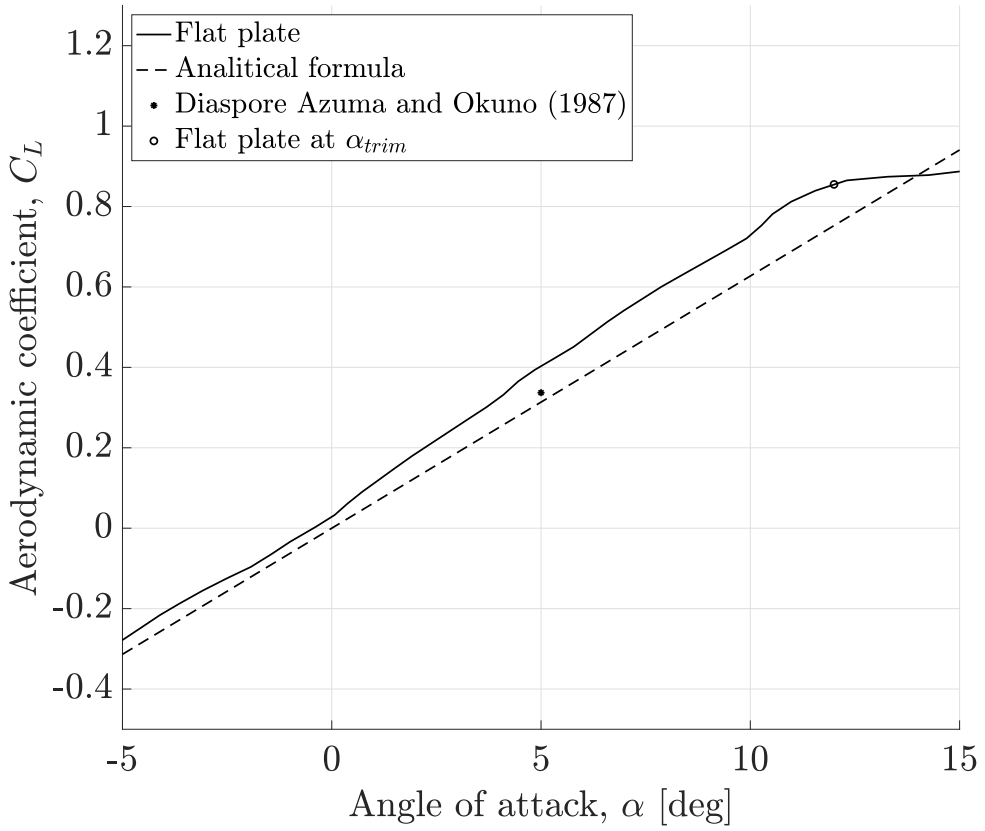

Fig. 2.20 The solid black line is the lift coefficient versus the angle of attack of a flat plate with a simplified planar shape mimicking *Alsomitra macrocarpa*, plotted from Minami and Azuma (2003). The analytical formula (2.31) is graphed with a dashed line. *Alsomitra macrocarpa* ($*$) at the measured C_L in Azuma and Okuno (1987) and the flat plate ($\circ$) at the angle of attack $\alpha = \alpha_{trim}$.

2.11 The polar curve

Each sample of *Alsomitra macrocarpa* flies at a lift coefficient, drag coefficient and in a range of angles of attack. In order to get the polar curve, hence the lift coefficient versus the drag coefficient, each seed Azuma and Okuno (1987) had to artificially change the trimmed angle of attack (α_{trim}). Azuma and Okuno (1987) applied a thin column along the plane of symmetry, as shown in figure 2.21, which shifted the position of the centre of mass by applying additional weights. The different position of the weight, hence of the centre of mass, changed α_{trim}. Results of polar curves of two and three-dimensional wings are plotted in figure 2.22.

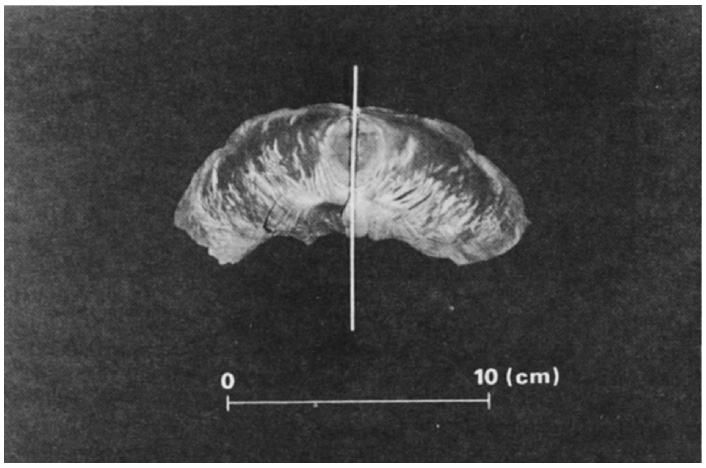

Fig. 2.21 Modified diaspore. Additional weights were attached to the column. Picture from Azuma and Okuno (1987).

2.12 The real seed and the flat plate

The drop tests performed by Azuma and Okuno (1987), on three different *Alsomitra macrocarpa* and ten flights gave an average C_L = 0.337 and C_D = 0.090. These are the average aerodynamic coefficients of real seeds, a 3D wing. Azuma and Okuno (1987) reported a C_L = 0.476 for a 2D wing and a C_L = 0.337 for a 3D wing, given that $C_L = 4.72\alpha$ (Azuma and Okuno, 1987), the range of possible trimmed angles of attack (α_{trim}) is between 4.09° and 5.78°. This range is totally different from the value stated in Minami and Azuma (2003), α_{trim} =12°. Minami and Azuma (2003) attributed α_{trim} =12° to Azuma and Okuno (1987), but the value never appears in their paper ("In the case of the *Alsomitra macrocarpa*, the trimmed angle of attack α_{trim} is 12° (Azuma and Okuno, 1987)"). The experimental mea-

surements performed by Minami and Azuma (2003) on a flat plate with the same planform of *Alsomitra macrocarpa* showed that, at 4.09° to 5.78°, $\frac{\partial C_m}{\partial \alpha} > 0$, so the flat plate would be unstable (Torenbeek and Wittenberg, 2009). Minami and Azuma (2003) had α_{trim} =12°, angle obtained with $C_m = 0$. The corresponding C_L is 0.85, hence 2.5 times higher than the value in Azuma and Okuno (1987), produced by experiments on real *Alsomitra macrocarpa*. Azuma and Okuno (1987) stated: "the flight at high lift coefficients C_L showed a slight tendency to spiral instability ". Figure 2.22 shows that in the range of C_D and C_L where *Alsomitra macrocarpa* operates, the real seed is closer to a rectangular flat plate with an aspect ratio of 2 than to the artificial model described in Minami and Azuma (2003). Drop tests of a flat piece of paper, with the geometry reported in table 3.1, displayed a tumbling motion. Section 3.5 highlighted recirculation areas behind the wrinkles of the corrugated membrane wing, a flow feature that does not belong to flat plates (Murphy and Hu, 2010). This analysis highlighted the importance of collecting independent data with a bespoke glide arena and depth cameras.

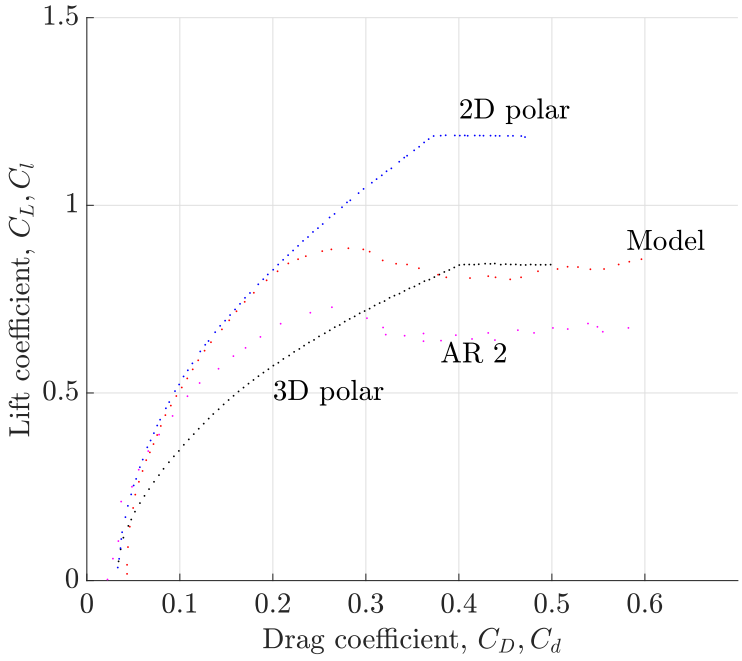

Fig. 2.22 Polar curves of *Alsomitra macrocarpa* (3 *Dpolar*) (Azuma and Okuno, 1987), rectangular flat plate with aspect ratio 2 (*AR2*) (Okamoto and Azuma, 2011), flat plate with the planform of the real seed (*Model*) (Minami and Azuma, 2003) and 2D wing (*2Dpolar*) (Azuma and Okuno, 1987).

Table 2.3 Geometric parameters of the ellipses.

a [m]	b [m]	c [m]	d [m]	e/a
0.03	0.003	0.012	0.001	[0,0.9]

2.13 Dynamics model

Leaves and seeds falling from trees do not fly in a straight line but exhibit complex dynamics. Maxwell (1854) performed a qualitative analysis of the tumbling motion. Kirchhoff (1882) analytically described the motion of a solid body in an inviscid fluid with a set of ordinary differential equations. Quasi-two-dimensional plates have been extensively studied (Andersen et al., 2005a,b; Belmonte et al., 1998; Mahadevan et al., 1999; Tanabe and Kaneko, 1994; Vincent et al., 2020a,b). In these papers the centre of gravity and the centre of buoyancy or centre of exterior geometry coincide, hence all the forces are applied to the same point and no net torque is produced. The centre of gravity describes three different kinds of non-chaotic, two-dimensional, trajectories: steady vertical descent, oscillatory flutter and rotary tumbling (Huang et al., 2013). These flight paths are exhibited by different seeds, for instance *Taraxacum officinale* and *Tragopogon pratensis* display a vertical descent (Casseau et al., 2015; Cummins et al., 2018), *Betula platyphylla* glides with a fluttering path (Minami and Azuma, 2003) and *Ailanthus altissima*shows a tumbling behaviour (Overbeck et al., 2007). In the experiments performed as part of this thesis, *Alsomitra macrocarpa* that flew in a straight path, displayed a motion that merged a periodic oscillation of the angle of attack, typical of fluttering and a net horizontal displacement characteristic of tumbling. A quasi-steady numerical model developed by Andersen et al. (2005a,b), was adapted to model this flying behaviour.

2.14 *Alsomitra macrocarpa* a two dimensional shape

A schematic drawing of the two-dimensional body is shown in figure 2.23. The mass m per unit length is:

$$m = \rho_p \pi ab + \left(\rho_a - \rho_p\right) \pi cd. \tag{2.32}$$

where $\rho_p = 1.2\,\mathrm{kg\,m^{-3}}$ is the density of the ellipse with semi-major axis a, while $\rho_a = 2.7\,\mathrm{kg\,m^{-3}}$ is the density of the ellipse with semi-major axis c. The set of parameters is reported in table 2.3. The centre of gravity of the ellipse is marked by O and the offset of O and O$'$ is

$$e = \frac{\left(\rho_a - \rho_p\right) cd}{m} h. \tag{2.33}$$

The moment of inertia of the ellipse with respect to the axis through O into the plane of the ellipse is

$$I = \rho_p \pi ab \left(\frac{a^2 + b^2}{4} + e^2 \right) + \left(\rho_a - \rho_p \right) \pi cd \left[\frac{c^2 + d^2}{4} + (h - e)^2 \right]. \tag{2.34}$$

2.14.1 The equations of motion

The flight of four *Alsomitra macrocarpa* that glided in a straight path was assumed to be two-dimensional. Straight flight allows *Alsomitra macrocarpa* to disperse over long distances, without being carried by the wind (Minami and Azuma, 2003). The three-dimensional helical paths are well beyond the scope of this thesis but will be studied, building on the data already collected. The straight flight path, representing two-dimensional dynamics, was modelled using ordinary differential equations. Pesavento and Wang (2004), described the free fall of leaves and business cards, developing Kirchoff's differential equations which model the dynamics of a solid body in an inviscid and irrotational flow (Aref and Jones, 1993; Kozlov, 1989; Lamb, 1945). The forces taken into account were: weight and fluid force, composed of lift, drag, buoyancy-corrected gravity and added mass (Andersen et al., 2005a,b; Pesavento, 2006; Pesavento and Wang, 2004). A quasi-steady approximation was implemented following Andersen et al. (2005a,b); Sedov (1980), the fluid forces depend on the kinematic variables alone, as in Andersen et al. (2005a,b). The Reynolds number was based on the semi-major axis a and the average descend velocity $\bar{U}$. The body that represented *Alsomitra macrocarpa* had an elliptical cross-section with half major axis a and half minor axis b. The model was written in the coordinate system linked to the moving elliptical body, a non-inertial reference frame. The angle θ was defined as the angle between the gravity vector ($\mathbf{g}$) and the minor axis of the ellipse. Instantaneous velocities of the centre of gravity and centre of buoyancy were written as:

$$\mathbf{V}_b = u_b \mathbf{i} + v_b \mathbf{j}, \quad \mathbf{V}_g = u_g \mathbf{i} + v_g \mathbf{j}. \tag{2.35}$$

They were connected by:

$$u_b = u_g, \quad v_b = v_g - e\dot{\theta}. \tag{2.36}$$

The angular velocity $\dot{\theta} = \omega$. The velocity of the centre of mass $\mathbf{V}_g$ was then re-written in the inertial reference frame of the laboratory

$$u = u_g \cos(\theta) - v_g \sin(\theta), \quad v = u_g \sin(\theta) + v_g \cos(\theta). \tag{2.37}$$

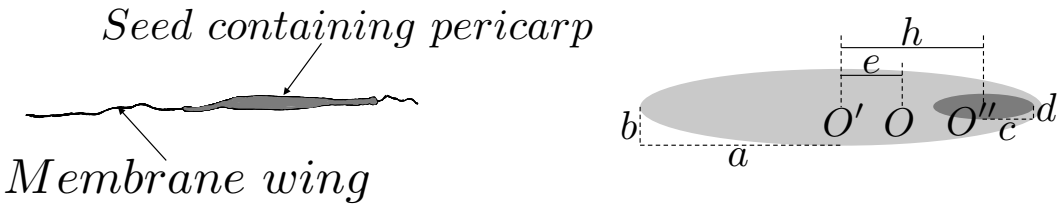

Fig. 2.23 Cross section of *Alsomitra macrocarpa* along the longitudinal plane and elliptical 2D geometry with two different densities used to model it.

where u is the horizontal velocity component and v is the vertical velocity component. The following set of second-order coupled differential equations describes the dynamics.

$$(m+m_{11})\,\dot{u}_g = (m+m_{22})\,\dot{\theta}v_g - \rho_f\Gamma v_g - m'g\sin\theta - F^{\nu}_{gx} \tag{2.38a}$$

$$(m+m_{22})\,\dot{v}_g = -(m+m_{11})\,\dot{\theta}u_g + \rho_f\Gamma u_g - m'g\cos(\theta) - F^{\nu}_{gy} \tag{2.38b}$$

$$(I+I_a)\,\ddot{\theta} = (m_{11}-m_{22})\,u_g v_g + l_\tau\rho_f\Gamma\sqrt{u_b^2+v_b^2} - \rho_f\pi abge\cos(\theta) - \tau^{\nu} \tag{2.38c}$$

Alsomitra macrocarpa gliding through the air was subjected to fluid forces and gravity. The buoyancy corrected gravity, as defined in Pesavento (2006), with the values reported in table 3.1 is $392\,\mathrm{g\,s^{-2}}$, comparable to the buoyancy corrected gravity of $88\,\mathrm{g\,s^{-2}}$ in Pesavento (2006). The lift, by definition, is orthogonal to the direction of motion and depends on the circulation $\Gamma = \Gamma\left(u_g, v_g, \dot{\theta}\right)$ (Andersen et al., 2005a). The drag is orthogonal to the lift and opposite to the direction of motion $\mathbf{F}^{\nu} = \mathbf{F}^{\nu}\left(u_g, v_g, \dot{\theta}\right)$ (Andersen et al., 2005a). The dissipative torque is opposite to the direction of rotation $\tau^{\nu} = \tau^{\nu}\left(u_g, v_g, \dot{\theta}\right)$ (Andersen et al., 2005a). The added mass coefficients m_{11} and m_{22} and the added mass moment of inertia I_a of an elliptical object with inhomogeneous mass distribution were derived from inviscid

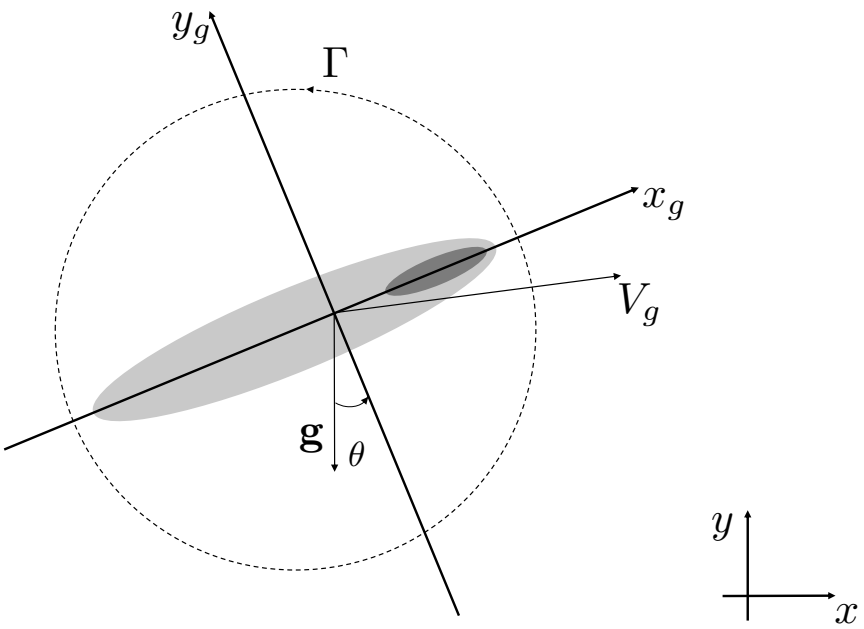

Fig. 2.24 The velocity components u_g and v_g of $\mathbf{V_g}$, in the laboratory reference frame were defined with respect to the coordinate system that follows the rotation of the elliptical body, as in Andersen et al. (2005a,b); Huang et al. (2013). The velocity components u and v are the horizontal and the vertical velocity component in the inertial reference frame, attached to the laboratory. The angle θ is the angle between the axis y_g, perpendicular to the major axis of the ellipse, and the direction of gravity $\mathbf{g}$.

theory (Andersen et al., 2005a; Huang et al., 2013; Sedov, 1980):

$$m_{11} = \pi\rho_f b^2, \quad m_{22} = \pi\rho_f a^2, \quad I_a = \frac{1}{8}\pi\rho_f \left(a^2 - b^2\right)^2 + \pi\rho_f a^2 e^2. \tag{2.39}$$

The second term in the expression for I_a is related to the fact that the origin of the non-inertial reference frame is placed at the centre of gravity which is displaced with respect to the centre of exterior geometry (Sedov, 1980).

Circulation and lift

Experiments performed by Andersen et al. (2005a,b), coupled with direct numerical simulations of Pesavento and Wang (2004) allowed to express the lift in a self-consistent form. Andersen et al. (2005a) discovered that the circulation of fluttering and tumbling cards, with Reynolds number between 100 and 1000 is related to translational speed and angular velocity. The circulation can be written in terms of the velocity components of the centre of exterior geometry, u_b,v_b and the angular velocity $\dot{\theta}$, as follows:

$$\Gamma = -C_T a \frac{u_b v_b}{\sqrt{u_b^2 + v_b^2}} + \frac{1}{2} C_R a^2 \dot{\theta}, \tag{2.40}$$

where C_T and C_R are dimensionless constants, weighing the contributions from translational and rotational velocity respectively. The translational component of the lift provides fluid forces during the straight gliding sections, fluttering for Andersen et al. (2005a,b), whereas the rotational component is dominant during tumbling, as described by Andersen et al. (2005a,b). The translational term is the Kutta-Joukowski lift at low angles of attack and it allows to consider stall at high angles of attack. Most of *Alsomitra macrocarpa*'s gliding path is like fluttering, while the sudden change in angle of attack α resembles tumbling, which may be caused by a stall of the wing. The elevation of the centre of mass is given by the rotational lift.

Table 2.4 Fitting parameters for the quasi-steady model as in (Huang et al., 2013).

C_T	C_R	C_0	$C_{\pi/2}$	C_τ
4.5	1.8	0.2	0.5	1.9

Drag and dissipative torque

Drag and dissipative torque depend on the Reynolds number. Wang et al. (2004) gave an equation for drag which is quadratic and depends on the angle of attack α:

$$
\begin{aligned}
F_x &= -\frac{\rho_f a}{2}\left[C_0\frac{u_g^2}{\sqrt{u_g^2+v_g^2}} + C_{\pi/2}\frac{v_g^2}{\sqrt{u_g^2+v_g^2}}\right]u_g,\\
F_y &= -\frac{\rho_f a}{2}\left[C_0\frac{u_g^2}{\sqrt{u_g^2+v_g^2}} + C_{\pi/2}\frac{v_g^2}{\sqrt{u_g^2+v_g^2}}\right]v_g,\\
\tau^v &= C_\tau\frac{\rho_f a^4\dot{\theta}|\dot{\theta}|}{64},
\end{aligned}
\tag{2.41}
$$

where C_0, $C_{\pi/2}$ and C_τ are dimensionless constants. The dissipative torque is described with a single term which depends on the squared angular velocity $\dot{\theta}$. It has to be highlighted that the circulation in Eq. 2.40 and the components of drag in Eq. 2.41 are only related to the plate's instantaneous motion, no history dependence is present. This is a quasi-steady assumption that greatly simplifies the full flow-structure interaction problem. The dynamic equations 2.38 coupled with the kinematic relations form a closed system that was solved with the MATLAB ode45 routine. This routine ode45 is based on an explicit Runge-Kutta formula, the so-called Dormand-Prince pair. It is a single-step solver because, in solving the first order ordinary differential equations, it only needs the solution at the preceding time step (Videler et al., 2004). The solution was made by the velocities u_b, v_b and θ, which were further integrated to get the trajectories in the inertial reference frame, i.e. the laboratory frame. The five parameters involved in the model (C_T, C_R, C_0, C_π and C_τ), which are present in equation 2.40 and equation 2.41 are mainly related to the outer shape of the ellipse with semi-major axis a. In the experimental drop test, *Alsomitra macrocarpa* was released with zero initial velocity and zero initial tilt angle θ, these were also the initial conditions for the numerical model.

2.14.2 Limits of the quasi-steady approximation

A quasi-steady force model, described in the previous sections and in Andersen et al. (2005a,b) misses two types of effects:

- unsteady effects related to the acceleration;
- interaction of the body with existing vortices.

The lift could be generated during translational acceleration from rest at a low angle of attack. Unsteady forces could be caused by the formation of vortices, both at the leading edge and the trailing edge during translational acceleration at a high angle of attack (Pullin and Wang, 2004). The second kind of unsteady effect, instead, is negligible for *Alsomitra macrocarpa* and fluttering or tumbling cards (Andersen et al., 2005a). It is relevant for flapping insects, where the wing, oscillating back and forth, dives into its own wake.

2.15 Simplified dynamics model

In drop tests, performed as part of this work, *Alsomitra macrocrpa* exhibited a straight gliding flight that may be modelled as a simple steady-state trimmed glide (Anderson Jr, 2010). The dynamic effects, presented in the previous sections 2.14.1, had to be included to capture the oscillations, not displayed by some diaspores. The torque due to circulatory lift τ_{Lift} could be a driver of the observed dynamics. The steady-state glide, at small angles of attack, of flat plates and symmetric aerofoils, develops a pitching moment (Anderson Jr, 2010). The dominant contribution to the pitching moment is the moment due to aerodynamic lift, shown in figure 2.25. A first representation of the gliding flight is a plate with a centre of mass forward of the aerodynamic centre, granting static stability (Torenbeek and Wittenberg, 2009), figure 2.25. The moment due to translational lift, and the dissipative drag, could be sufficient to capture some of the gliding trajectories displayed in chapter 3. This model represents a glider, trimmed at zero lift (Minami and Azuma, 2003). The trimmed flight condition presents a lift contribution equal to zero (Anderson Jr, 2010). In Andersen et al. (2005b), some results highlight that, during parts of the tumbling and fluttering flight of plates, some periods have a moment due to translational lift higher than the moment measured with the experiments. This observation is based on the assumption that the lift acts at the quarter chord for all angles of attack (Anderson Jr, 2010). A flat plate model, subject to the acceleration due to gravity, where the centre of mass is placed at the leading edge and taking into account circulatory lift and moment, dissipative drag is studied, as displayed in figure 2.26. The addition of a zero-lift pitching moment coefficient (C_{m0}), allows considering the moment

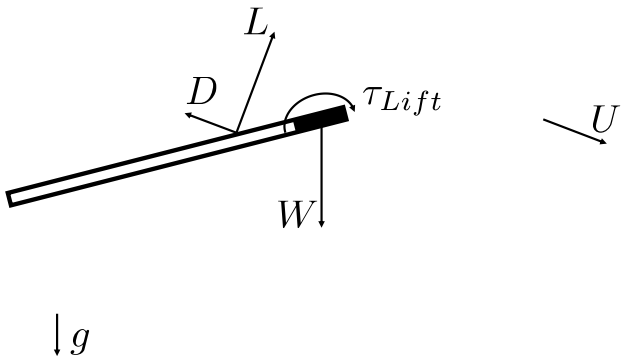

Fig. 2.25 Flat plate with the centre of mass at the leading edge.

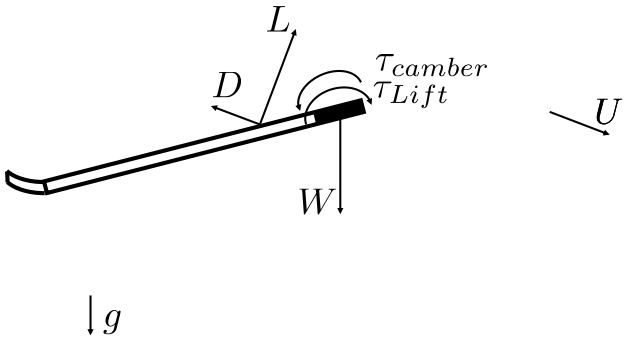

Fig. 2.26 Flat plate with the centre of mass at the leading edge and curved trailing edge.

generated by camber τ_{camber}, figure 2.26. This zero-lift pitching moment allows the plate to be trimmed at a positive lift and consequently achieve an inclined glide path as shown by gliding aircrafts (Pajno, 2010). While a diaspore like *Alsomitra macrocarpa* is capable of achieving a cambered airfoil through passive aero-elastic deformation, observed during the test campaign performed in the wind tunnel, a plate would require negative camber, mainly located towards the trailing edge (Anderson Jr, 2010; Torenbeek and Wittenberg, 2009). The modelling of the local wing aerodynamics and aero-elastic effects is an interesting research topic, but beyond the scope of this thesis.

Chapter 3

Results

3.1 Morphology

The description of the morphology of *Alsomitra macrocarpa* required the purchase of 31 diaspores from two different suppliers, in order to get a broad sample variability. The geometrical characteristics of the 31 diaspores are provided in tables A.1, A.2, A.3 and A.4. The mean values and 95% confidence intervals are reported in table 3.1, showing good agreement with the values reported by Azuma and Okuno (1987); Nachtigall (2011b). The seed containing pericarp presented a thickness of 1 or 2 millimetres and was assumed to be the centre of gravity of the diaspore. The membrane wing is extremely thin, from a few µm at the edges to a few hundred µm in the thickest part. The thickness contributes to making some parts of the membrane wing transparent. The geometrical sweep angle is key to moving the aerodynamic centre behind the centre of mass and stabilising the pitching motion. Some cross sections of the wing are presented later in figure 3.2. The reflected airfoil mentioned by Azuma and Okuno (1987) as a source of pitching stability was not detected. A correlation matrix was applied to the values of mass, wing span, wing surface, geometrical sweep angle and mean geometric chord, with a threshold on the correlation coefficient of 0.6 and a p-value of 0.05, no unexpected correlation was detected.

3.2 Planform

A quadratic equation was developed, building on the results of the morphometric analysis, to describe the average planar form of 24 diaspores. The idea of representing the outline of a wing with a simple mathematical function has already been implemented by Weis-Fogh (1973) and Faisal and Filippone (2016a,b) to study the fluid mechanics of wings of hovering

Table 3.1 Mean value and 95% Confidence interval of morphological characteristics *Alsomitra macrocarpa*.

Morphology	Mean value	95% Confidence interval
Mass, m [g]	0.36	0.32 to 0.39
Wing-span, b [mm]	171	168 to 175
Wing chord, c_{centre} [mm] on the roll axis	70	68 to 73
Wing surface, S [mm^2]	10244	9787 to 10656
Geometrical sweep angle, Λ [deg]	17.5	16.9 to 18.2
Centre of gravity, CG [mm] distance from leading edge	22	22 to 23
Aspect ratio, AR = b^2/S	2.84	2.77 to 2.92
Mean geometric chord, $m.g.c.$ [mm]	60	58 to 61
Wing loading, W/S [N m^{-2}]	0.35	0.32 to 0.37
Density, ρ [g m^{-2}]	35	32 to 37

Table 3.2 Coefficients of the quadratic equation 3.1.

Coefficient	Value
a_{am}	0.38
b_{am}	0.80
c_{am}	0.39
d_{am}	-0.96

insects. This simple, two-dimensional, geometrical shape presents a sweep, tapered form, as required to perform a stable gliding flight, as presented in figure 3.1.

$$(y_{am} - c_{am}|x_{am}|^{b_{am}})^2 + (c_{am}x_{am})^2 - d_{am} = 0 \tag{3.1}$$

where $y_{am} = y/b$ is the normalised wing-span, $x_{am} = x/b$ is the normalised chord and b is the average wing-span of the 24 *Alsomitra macrocarpa* analysed. The coefficients are listed in table 3.2.

3.3 Three-Dimensional Shape

The 3D scanner produced a point cloud with more than 3 000 000 points. Wing roughness height of the *Alsomitra macrocarpa* studied turned out to be 1 to 3 % of the chord length on the membrane wing, similarly to swift wings (Lentink and De Kat, 2014), 10 000 times rougher

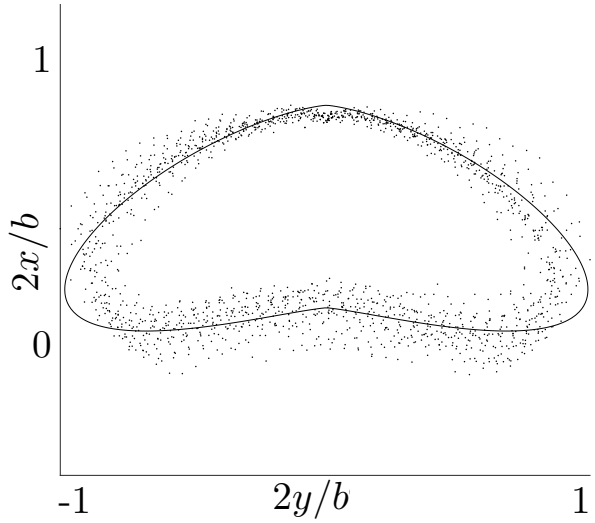

Fig. 3.1 Data points from the planar form of 24 diaspores fitted with the quadratic equation.

than sailplane wings. Sailplanes rely on smooth wings to increase the area of laminar flow over the wing and minimise drag, with the scope of extending the gliding distance. Corrugated wings are common in the insect kingdom, some examples include *Aeschna cyanea*, *Locusta migratoria* and *Tipula*. The wing has to provide aerodynamic efficiency during flight.From a structural perspective, the effect of corrugations, or wrinkles is that of raising the moment of inertia I of the cross-section and as a consequence, the flexural stiffness EI (Rees, 1975a). The aerodynamic contribution of a corrugated airfoil is linked to the roughness height, relative to the thickness of the air layer that flows over the wing, known as the boundary layer (Schlichting and Gersten, 2015; White and Majdalani, 2006). At the coordinate where roughness height and boundary layer thickness are similar, disturbances trigger the laminar to turbulent transition (Schlichting and Gersten, 2015; White and Majdalani, 2006). The boundary layer thickness δ is a function of chord length L and the velocity of the wing U through the Reynolds number. This dimensionless number describes the ratio of inertial to viscous forces in the boundary layer (Schlichting and Gersten, 2015). $Re \approx 5000$ is the average Reynolds number experienced by *Alsomitra macrocarpa* during the glide. The Reynolds number is always around a few thousand, taking into account natural variation and unsteady glide. Adopting a flat plate approximation, $\delta/L = 5Re^{-0.5} \approx 0.07$ as reported by Schlichting and Gersten (2015), the boundary layer thickness at the trailing edge is 7% of the chord length.The mean geometric chord, reported in table 3.1 is 60 mm, hence the boundary layer thickness at the trailing edge is around 4 mm. The measured roughness on the scanned *Alsomitra macrocarpa* was 1 to 3 %, hence it may disturb the laminar

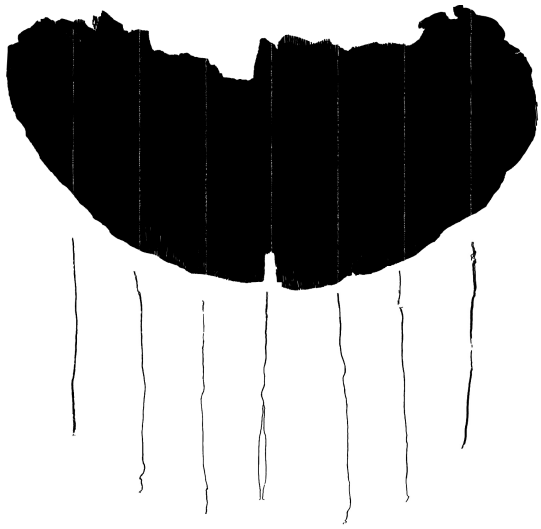

Fig. 3.2 *Alsomitra macrocarpa* scanned at the top, with the corresponding cross sections of the wing at the bottom.

airflow, forcing a transition to a turbulent state (Schlichting and Gersten, 2015; White and Majdalani, 2006). Surface roughness elements that force airflow to become turbulent are usually called "turbulators" (Schlichting and Gersten, 2015). Turbulators can increase lift and decrease drag by reducing laminar flow separation (Nachtigall, 1985). In order to understand the effectiveness of a turbulator, the roughness Reynolds number, defined as $Re_k = Re \times k/L$ has to be calculated. The roughness height is k. *Alsomitra macrocarpa* had a $Re_k \approx 167$. The lowest value of Re_k required to force the laminar to turbulent transition is 80, but for a Reynolds number of 100 000 (Lyon et al., 1997). This was the lowest Reynolds number found in the literature. *Alsomitra macrocarpa* could have sufficient aerodynamic roughness to trigger turbulence.

3.4 Tip deformation

Experiments performed in the Visualisation Tunnel showed that during its glide *Alsomitra macrocarpa*'s membrane wing experiences noticeable deformations. The pattern of wrinkles and the spatial distribution of thickness defined the scale of this deformation.

Data from the experiments are plotted in figure 3.3 and 3.4. Different markers are related to different angles of attack, $\circ$ for 0 deg, $\diamond$ for 5 deg, $\triangle$ for 10 deg and $*$ for 15 deg.

The membrane wing, from a structural perspective, was modelled as a cantilever beam, fixed on the longitudinal plane, with a uniform load distribution over the span (Combes and

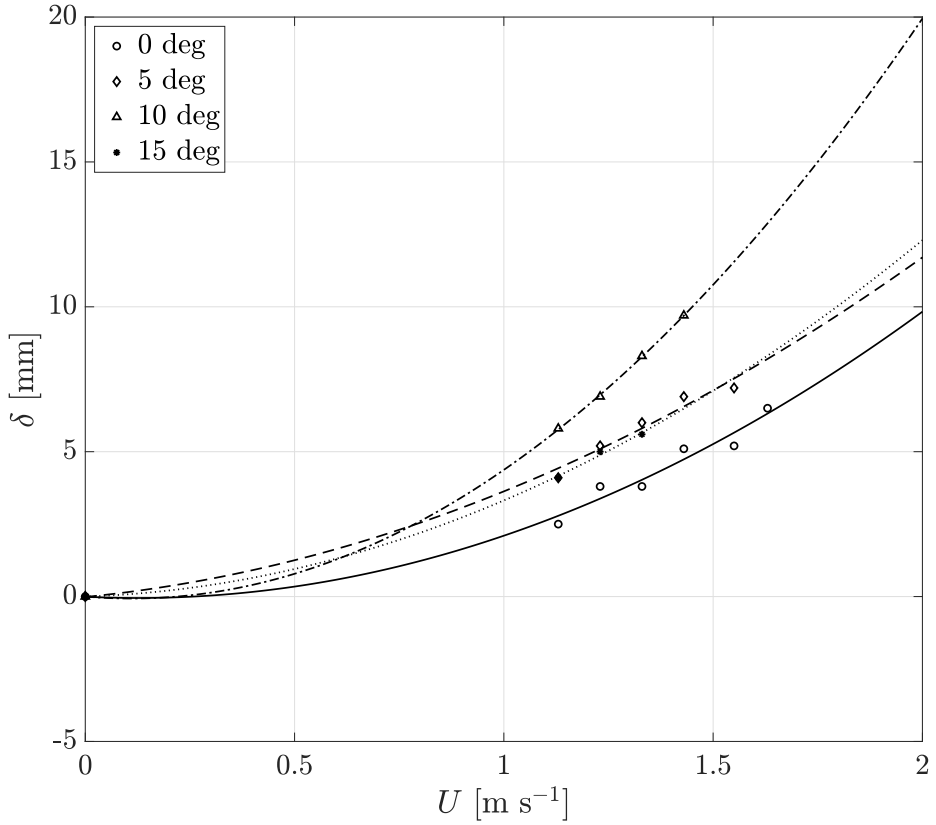

Fig. 3.3 Deflection of the left wing tip.

Daniel, 2003a,b). The load applied in the vertical direction, that caused the tip deflection is lift L. The lift can be expressed as $L = \frac{1}{2}\rho S c_L U^2$, where ρ is the density of the fluid, S is the wing surface, C_L is the lift coefficient and U the free stream velocity. Lift depends on the squared value of free stream velocity, hence $\delta \propto U^2$. The values measured were then fitted with a second-order polynomial, as shown in figure 3.3 and 3.4 to extend the results over the range of velocities experienced by *Alsomitra macrocarpa* during the glide. All the fitted curves are monotonically increasing with free stream velocity (figure 3.3 and 3.4), however, for both tips, the deflection δ is maximum when the angle of attack is 10 deg. The lift coefficient C_L is the only term of the lift equation that depends on the angle of attack. A lower lift at a higher angle of attack would mean that 15 deg is over the stall angle, differently from what is claimed by Azuma and Okuno (1987); Minami and Azuma (2003); Nachtigall (2012). The dihedral angle produced by the deformation has a crucial role in guaranteeing rolling stability (Torenbeek and Wittenberg, 2009) and elevating the aerodynamic centre relative to the centre of gravity (Thomas and Taylor, 2001).

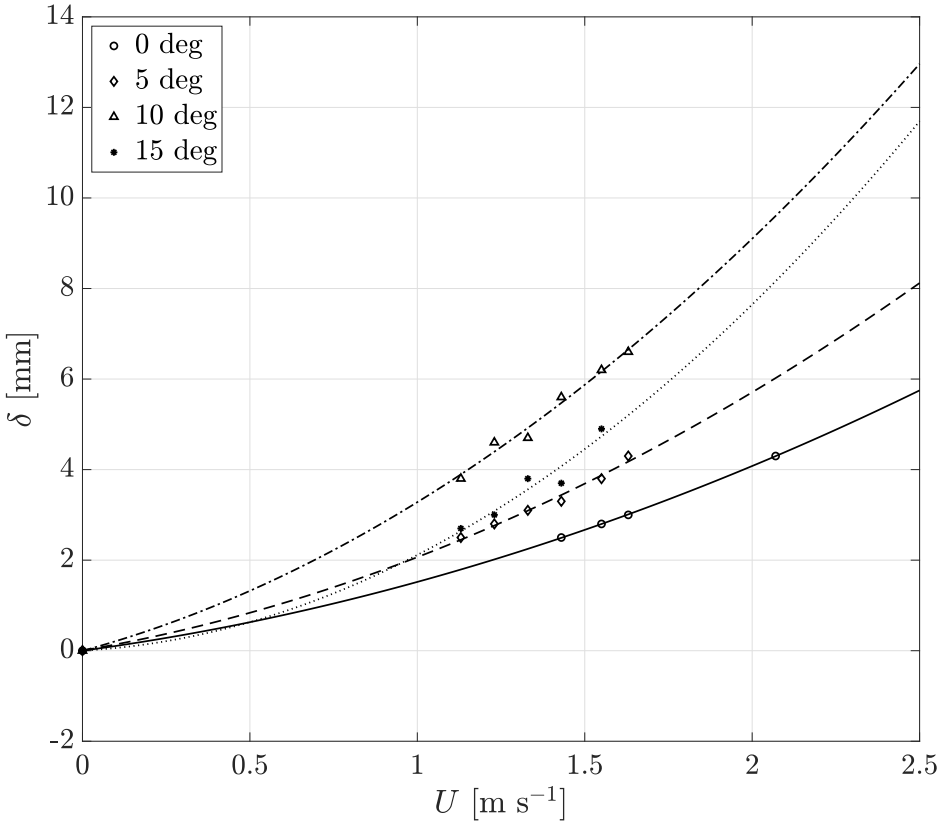

Fig. 3.4 Deflection of the right wing tip.

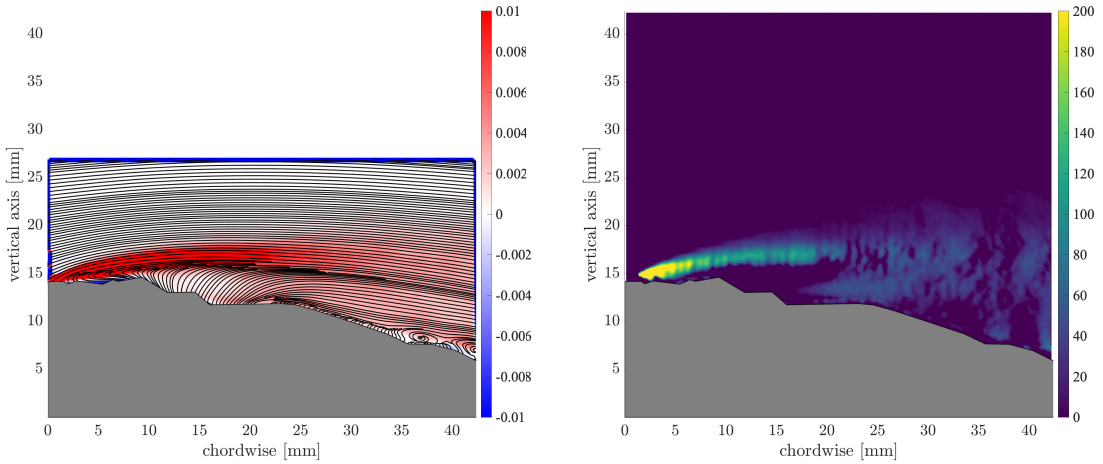

(a) Streamlines superimposed to the vorticity plot.

(b) Swirling strength.

Fig. 3.5 Flow field near the leading edge.

3.5 Particle Image Velocimetry

This section presents the results of the experiments conducted in the Anatomy Wind Tunnel. Figure 3.6 shows the tip vortex on the right side of the membrane wing. In figure 3.5a the streamlines on the suction side of the corrugated airfoil are bent, behaving exactly how they do on an airfoil. The flow over a corrugated wing, presented in figure 3.5a and 3.5b seemed to involve some fluid becoming trapped in the folds where it rotates slowly about an axis parallel to the span of the wing (Rees, 1975a). As shown by the recirculation zones near half of the chord (chordwise coordinate around 40 mm). However the streamlines that seem to originate from the solid (chordwise coordinate 15 mm) reveal a significant spanwise flow. At the Reynolds number experienced by *Alsomitra macrocarpa* during the glide, the corrugated airfoil offers a range of advantages: low mass, high stiffness and a reduced stress due to bending (Rees, 1975a,b), while providing an aerodynamic performance comparable to that of a smooth profile. Wings that operate at a Reynolds number of a few thousands do not show a deterioration in performance due to roughness.

3.6 Emission results

The results of measurements performed with the spectrometer at King's college by Dr Taani (Taani, 2020) are shown in Figure 3.7 and 3.8. These results confirmed that Azure Kinect cameras could get the position of the object from the received infrared light, allowing the depth cameras to track *Alsomitra macrocarpa*'s flight. Figure 3.7a and 3.8a are 3D

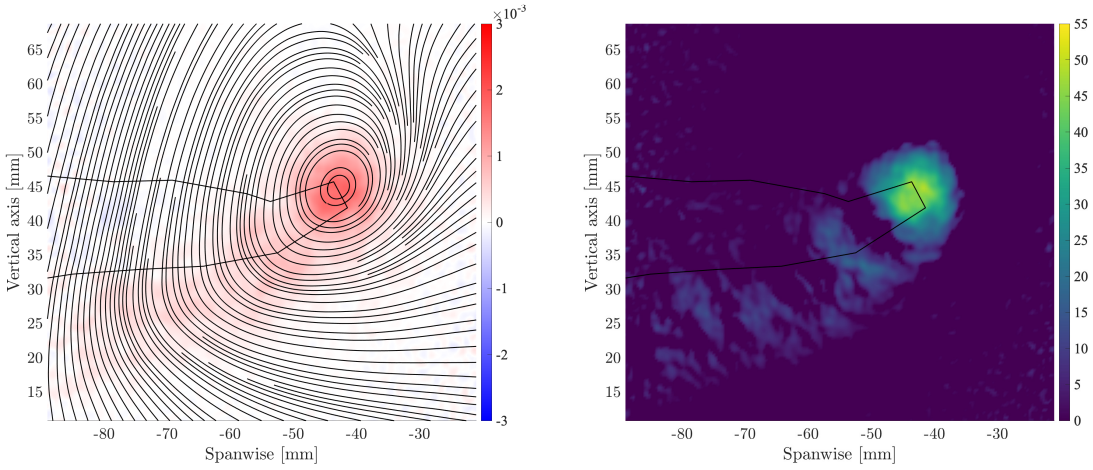

(a) Streamlines superimposed to the vorticity plot.

(b) Swirling strength.

Fig. 3.6 Images highlighting the tip vortex one mean geometric chord downstream of the trailing edge.

reflection spectrum plots that show the wavelengths of reflected light on the vertical axis versus the wavelengths of incident light on the horizontal axis. Both axes cover a wavelength range spanning between 600 and 900 nm. The colour map represents the intensity of the detected light. The 2D graphs in figure 3.7b and 3.8b were obtained extracting the values from figure 3.7a and 3.8a respectively, when the incident light has a frequency of 850 nm, i.e. frequency at which the Azure Kinect depth cameras operate (Microsoft, 2019). When the seed containing pericarp or the membrane wing are illuminated with light at 850 nm they reflect at 850 nm, if they were absorbing all the incident light, there would not have been peaks in figure 3.7b and 3.8b.

3.7 Point cloud analysis

A total of 15 *Alsomitra macrocapra* were recorded, with at least 5 technical repeats per diaspore and an average of 51 frames per glide, almost 2 s. The flow chart drawn in figure 3.10 highlights the main steps used to process the point clouds generated by the depth cameras. The analysis was performed with a custom-written program in MATLAB (MathWorks, Inc., Natick, MA, USA). Firstly, point clouds independently generated by the two cameras were acquired. In each frame recorded, the two point clouds were merged to generate a single point cloud. Three geometrical transformations, two rotations, around x and y axes and a translation along the z axis were executed, aligning the reference frame of the point cloud with the reference frame of the laboratory. The z axis is perpendicular to the ground

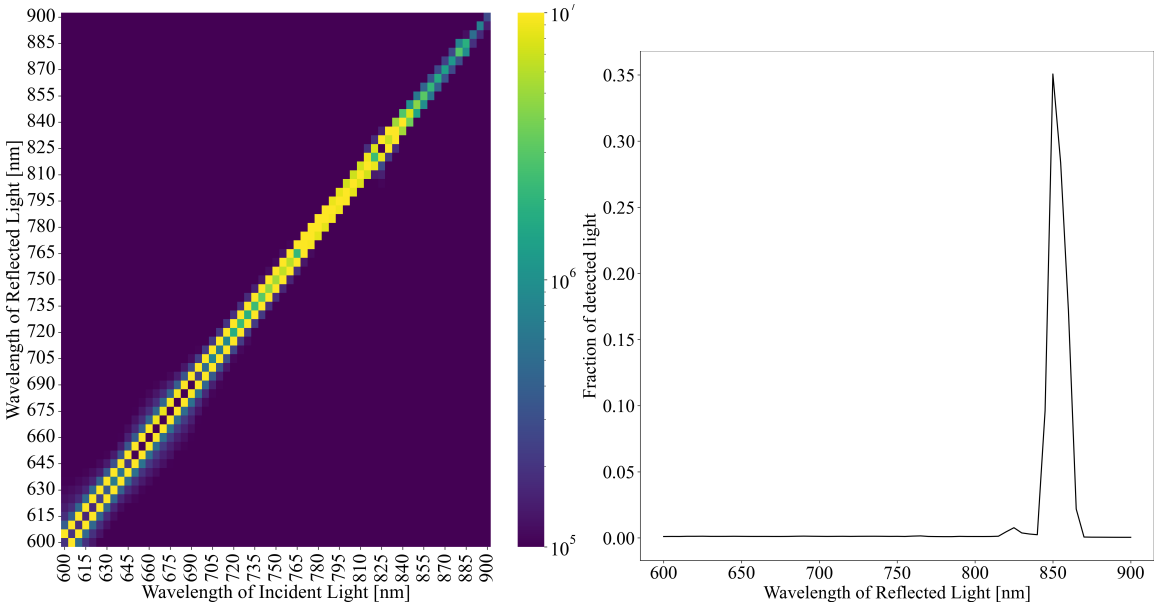

(a) Spectrum of reflected light for the seed containing pericarp.

(b) Spectrum of reflected light when the seed containing pericarp is illuminated with 850 nm light.

Fig. 3.7 Results of spectrometer measurements performed on the seed containing pericarp.

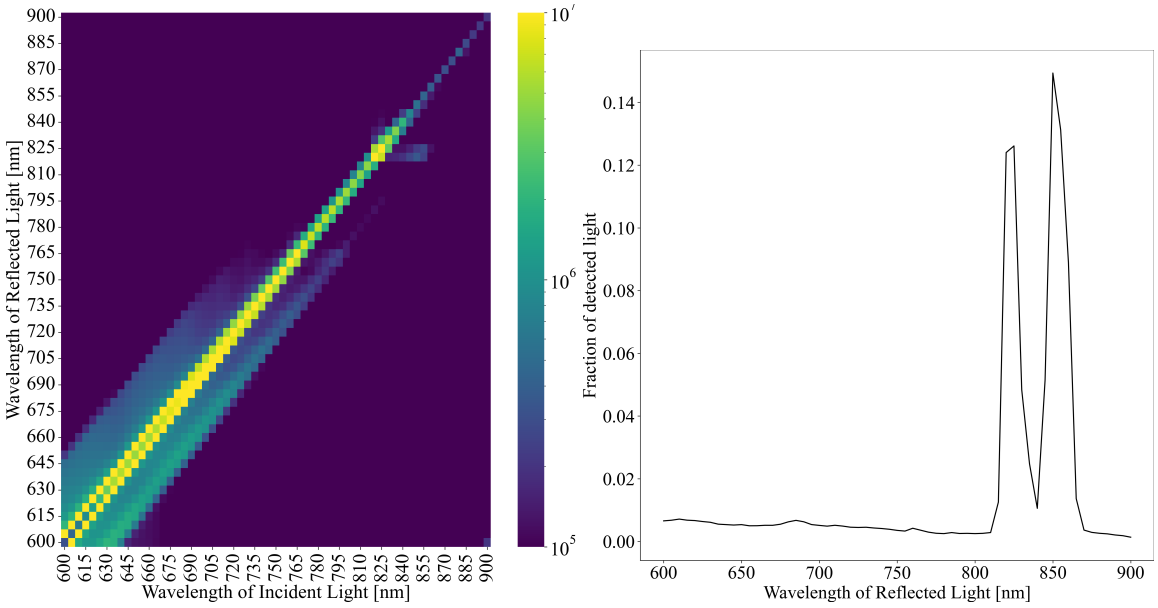

(a) Spectrum of reflected light for the membrane wing.

(b) Spectrum of reflected light when the membrane wing is illuminated with 850 nm light.

Fig. 3.8 Results of spectrometer measurements performed on the membrane wing.

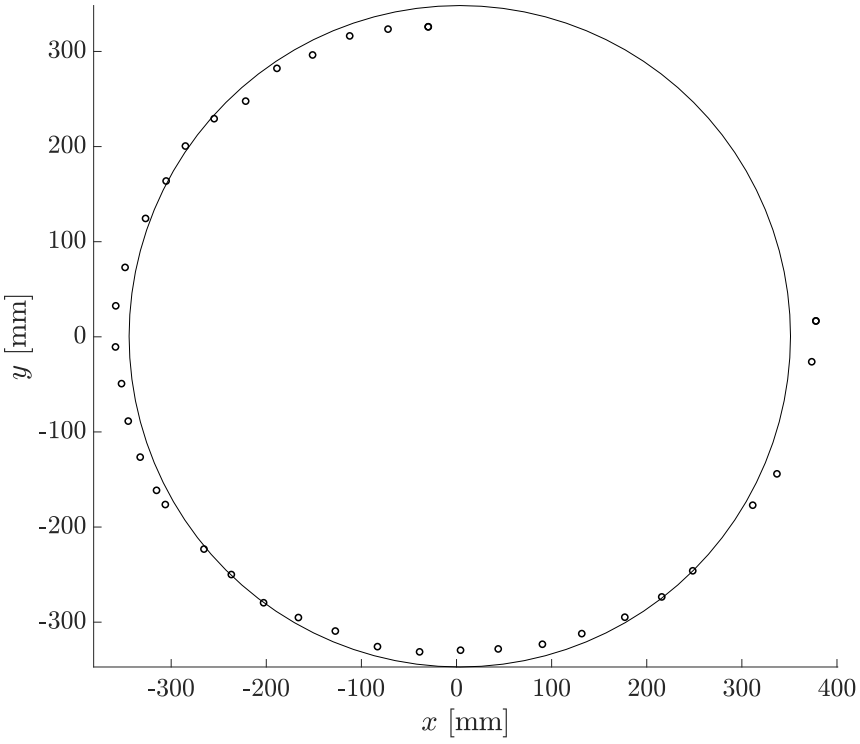

Fig. 3.9 Example of a set of centroid positions fitted with the function circfit.

and the x axis points in the direction of the glide for a straight flight. A region of interest (ROI) was then defined to reduce the number of points taken into consideration, reducing the computational time and performing raw denoising. Points within the specified ROI were obtained with the MATLAB function findPointsInROI. This function is built around a Kd-tree based search algorithm (Muja and Lowe, 2009). The point cloud inside the ROI was then denoised with the function pcdenoise (Rusu et al., 2008), obtaining a point cloud representative of the surface of the diaspore. The arithmetic mean of the coordinates was identified as the centroid of the point cloud. The extent of the initial transient, between the release at zero initial velocity and the gliding flight in a steady or periodic state, was determined with the qualitative investigation of hand-held diaspores dropped in a quiescent environment and with the literature Azuma and Okuno (1987); Nachtigall (2011a); Saito et al. (2008). The different flight trajectories, straight and helical, required two different approaches. In order to confirm the qualitative analysis conducted with simple drop tests, the centroids projected on the horizontal plane x y were fitted with a circle, employing the Matlab function circfit, as shown in figure 3.9. The function circfit executes the least squares fitting of two-dimensional data to a circle. The results of this analysis led to an average radius

of 0.573 m. The maximum radius obtained was 1.574 m, any trajectory that led to a radius three orders of magnitude bigger was considered a straight glide.

3.7.1 Data processing

A total of four diaspores flew with a straight gliding path, while the majority, eleven, displayed a helical gliding path. Data points depicting the position of the centroid in each frame, and in straight gliding were fitted with a straight line. The data points were then rotated rigidly around the z axis, placing the fitting line on the vertical plane x-z. The horizontal axis x followed the glide's projection onto the floor and the vertical axis z pointed vertically up, opposite to gravity, with the last position detected set as the origin. The data points were then interpolated with a Fourier series with six harmonics, describing the coordinates x, y and z as a function of time. In MATLAB, Fourier series are expressed in trigonometric form. The following equation, for instance, represents the approximation of $x(t)$ with a Fourier series:

$$x(t) = a_0 + \sum_{k=1}^{n} a_k \cos(k\xi t) + b_k \sin(k\xi t), \tag{3.2}$$

the constant a_0, known as the intercept, is associated with the $k = 0$ cosine term, ξ is the fundamental frequency and n is the number of harmonics in the series, $n = 6$ in our analysis. Various interpolating methods were tested, Fourier series with 6 harmonics was selected because it produced the best balance between smoothness and accuracy. A coefficient of determination, Ordinary R-squared, greater than 0.95 defined an accurate fitting. The Fourier series allowed to move from a discrete to a continuous description of the position in time. Velocity and acceleration components were calculated as first and second derivative of the Fourier series, thanks to the MATLAB function differentiate. The terminal velocity, vertical component of velocity, was calculated as ratio of the distance covered over the time interval, similarly the total velocity was obtained from the vector sum of the three averaged components.

3.8 Gliding path

The gliding flight of 15 *Alsomitra macrocarpa* was tracked. Gliding is an efficient form of travel adopted by plants (Minami and Azuma, 2003) and terrestrial vertebrates (Bahlman et al., 2013). To understand the kinematics of *Alsomitra macrocarpa* the glide was tracked with two depth cameras, operating at 30 Hz. Velocities and accelerations were extracted from the trajectories in cartesian coordinates.

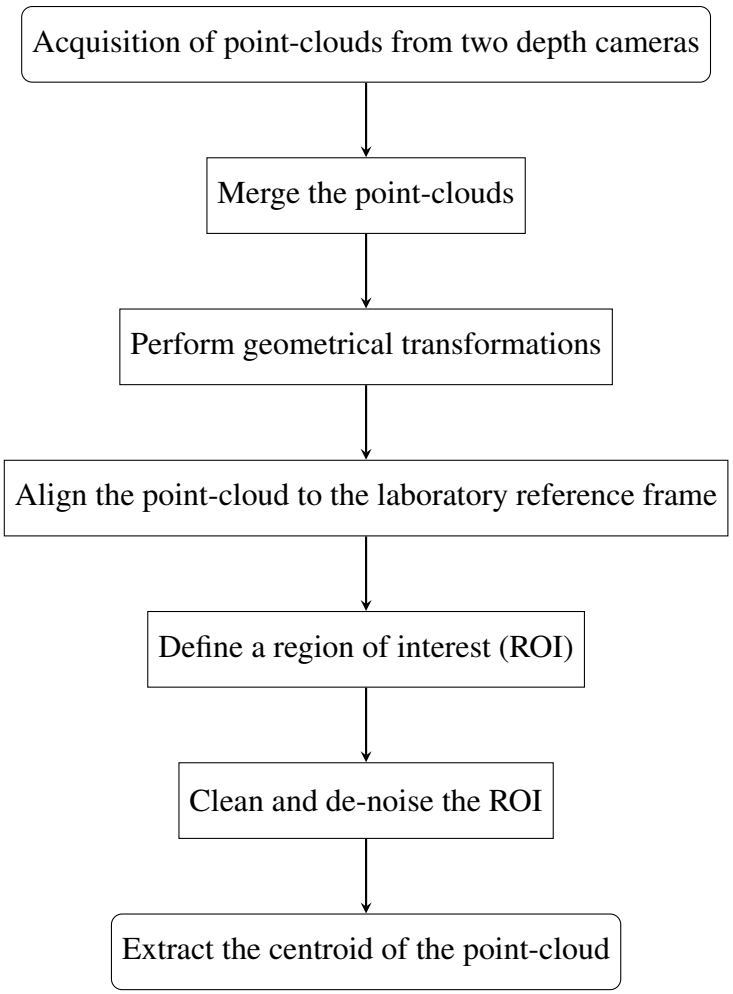

Fig. 3.10 High-level flowchart of the MATLAB analysis of the point-clouds.

3.9 Different gliding paths

Alsomitra macrocarpa exhibits different gliding paths, 15 diaspores were tracked with depth cameras. A helical trajectory was displayed by 11 diaspores depicted in figure 3.15, figure 3.16, figure 3.17, while the remaining 4 glided in a straight path (figure 3.14). The time series of the x, y and z coordinates for the straight glide are reported in figure 3.11, figure 3.12 and figure 3.13, while the time series regarding the helical glide are presented in figure 3.18, figure 3.19 and figure 3.20. Both helical and straight trajectories exhibited a phugoid motion which is linked to displacement of the centre of mass and centre of buoyancy as shown in previous sections and by the literature (Li et al., 2022). The analysis of the planar form of the diaspores with the parameters commonly adopted in aviation, to characterise wings (table 3.1, Azuma and Okuno (1987)) and leaves (Chuanromanee et al., 2019) did not give conclusive results, because of a small sample size. Studies on insect wings (Alba et al., 2021) and leaves (Chuanromanee et al., 2019) involved hundreds of samples. The proportion of diaspores that performed different gliding behaviours agrees with the data reported in the literature (Azuma and Okuno, 1987). *Taraxacum officinale* and *Zelkova abelicea* have different dispersal mechanisms, wind dispersal for the former (Cummins et al., 2018) and animal dispersal for the latter (Egli, 1997), nonetheless the majority of the seeds germinate in the proximity of the mother plant (Howe and Smallwood, 1982). The gliding flight of 4 diaspores, tracked with depth cameras displayed a straight path, as reported in figure 3.14 and figure 3.12 where the oscillations are between $-120\,\mathrm{mm}$ and $130\,\mathrm{mm}$. The four time series in figure 3.11 are monotonically increasing as the diaspores advance during their fall (figure 3.13). The gliding trajectories were recorded once the diaspores had reached their steady or periodic flight. The initial transient was kept outside the investigated volume. The time series of x, y and z highlight that, given the biological variation, it was not always possible to capture a full period. The gliding flight of *Alsomitra macrocarpa* was considered straight when the lateral displacement, plotted in figure 3.12, was of the same order of magnitude of the wing-span b in table 3.1. The lateral displacement can be inferred from figure 3.12. The lateral oscillations depicted in figure 3.14 could be related to an asymmetric development of the three-dimensional separation bubble as documented in Gresham et al. (2010). Low aspect ratio wings at low Reynolds number showed self-induced roll oscillations (Gresham et al., 2010). The horizontal velocity component u, in the direction of the gliding flight, oscillates around a positive value, reaching negative values for diaspore 21 and 26. A negative value for the horizontal velocity u means that *Alsomitra macrocarpa* is moving backwards, opposite to the direction of flight. The lateral velocity component v, oscillates around $0\,\mathrm{m\,s^{-1}}$. In a planar motion, which is two-dimensional, v would be 0. The vertical velocity component w oscillates around a negative value, *Alsomitra macrocarpa* is falling, for a glider it would have a constant

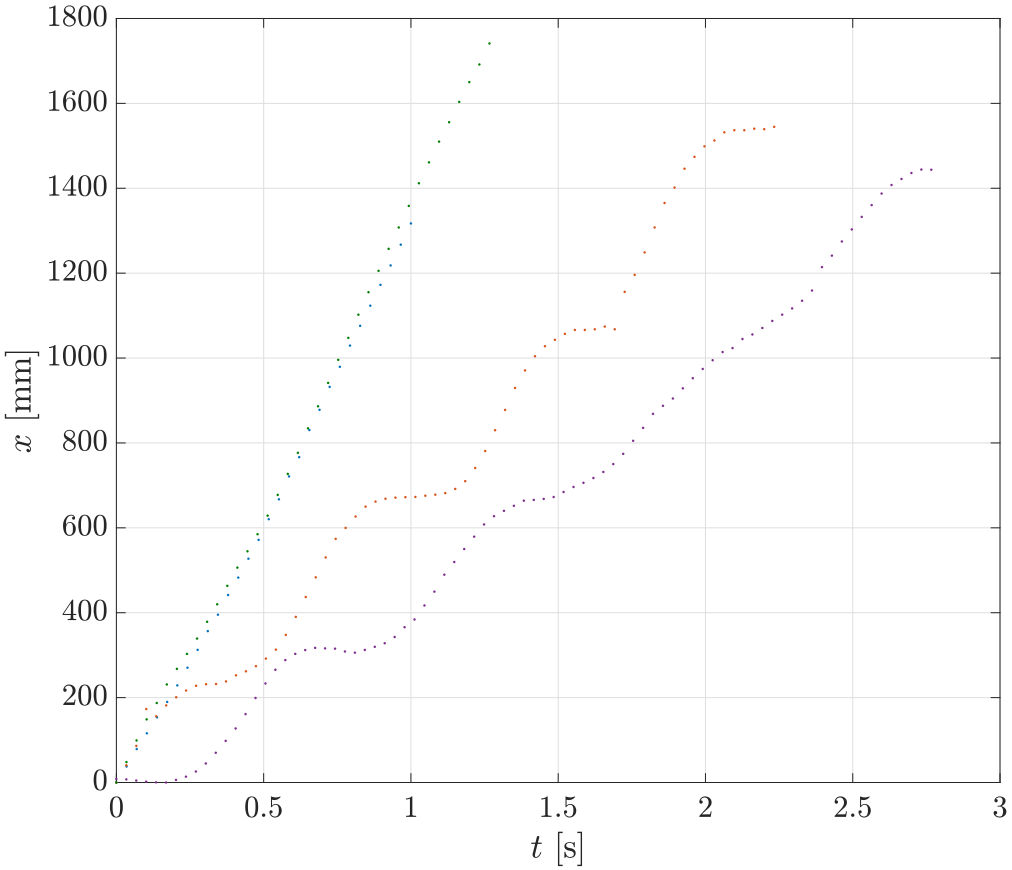

Fig. 3.11 Time series of the x component of the straight glide of 4 diaspores. Each glide is represented by a different colour.

value. A positive value of w, showed by figure 3.14 for diaspore 21 and 26 means that the diaspore is climbing, moving in a direction opposite to the gravity vector. The acceleration plots display the three components of acceleration a_x, a_y and a_z, oscillating around a zero mean value in a maximum range $-10\,\mathrm{m\,s^{-2}}$ to $10\,\mathrm{m\,s^{-2}}$. The lateral acceleration component a_y presents the shallowest range as the respective velocity v is almost constant and has a narrow range of values.

3.9.1 Helical gliding path

The gliding flight of the remaining 11 diaspores featured a helical gliding path as recorded in figure 3.15, figure 3.16 and figure 3.17. The time series are plotted in figure 3.18, figure 3.19 and figure 3.20. The gliding trajectories were recorded once the diaspores had reached their steady or periodic flight. The time series highlight that, given the biological variation, a

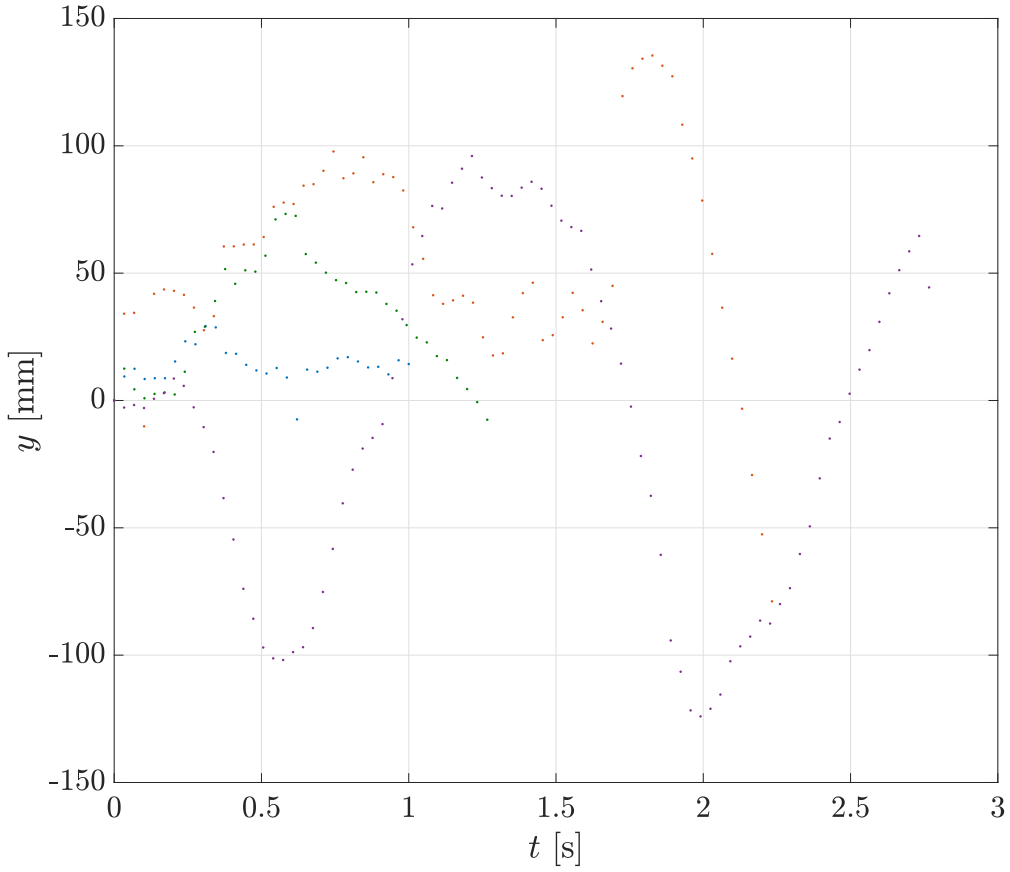

Fig. 3.12 Time series of the y component of the straight glide of 4 diaspores. Each glide is represented by a different colour.

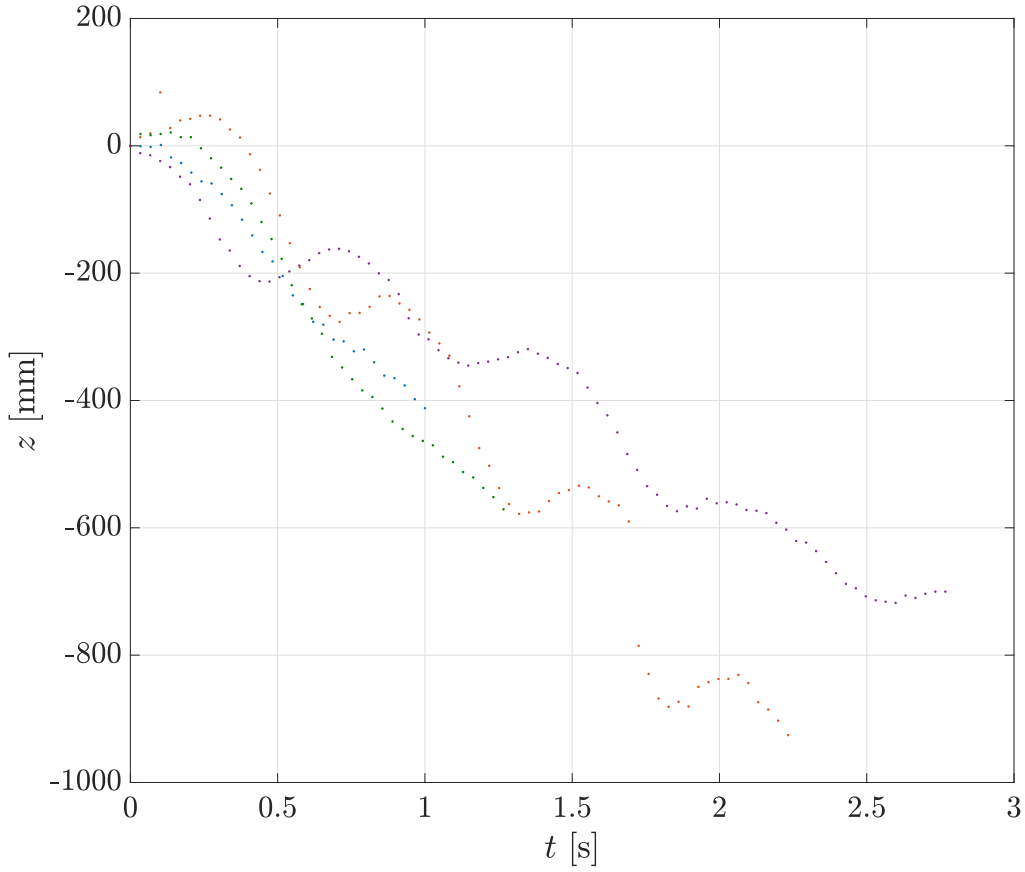

Fig. 3.13 Time series of the z component of the straight glide of 4 diaspores. Each glide is represented by a different colour.

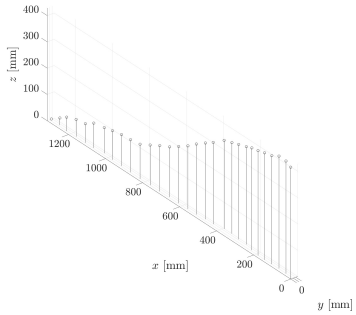

(a) Diaspore 1, 3D trajectory,

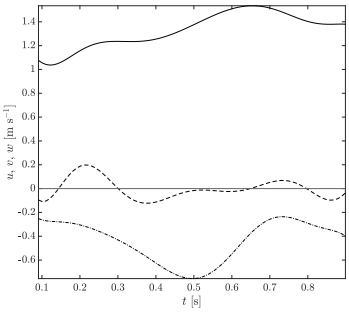

(b) Velocity components,

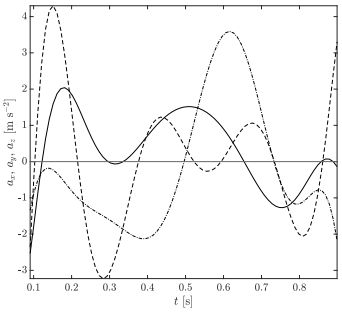

(c) Acceleration components.

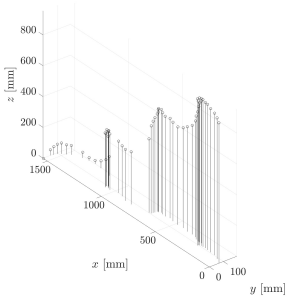

(d) Diaspore 21, 3D trajectory,

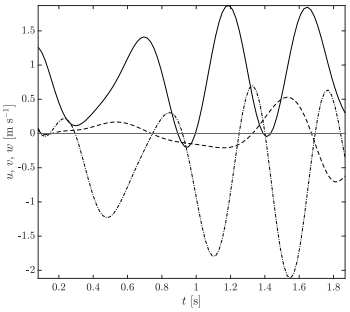

(e) Velocity components,

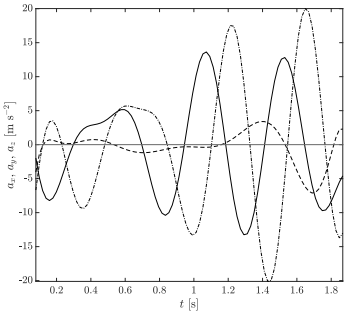

(f) Acceleration components.

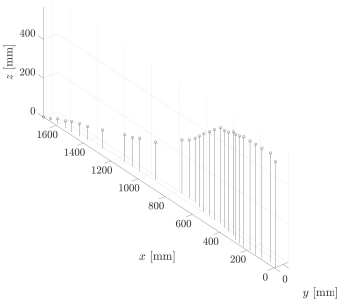

(g) Diaspore 23, 3D trajectory,

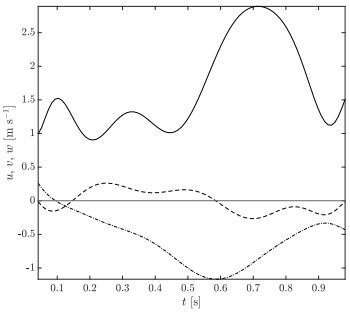

(h) Velocity components,

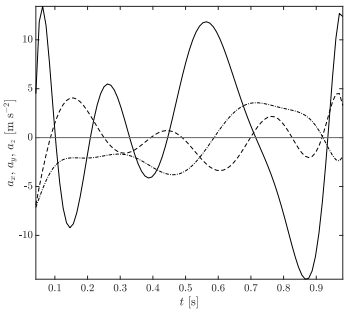

(i) Acceleration components.

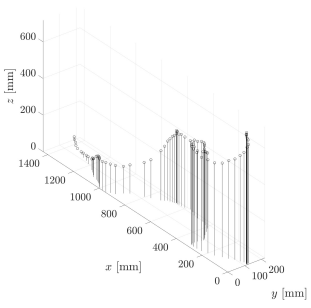

(j) Diaspore 26, 3D trajectory,

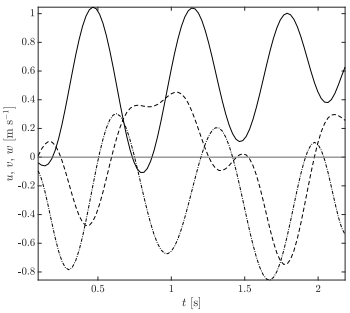

(k) Velocity components,

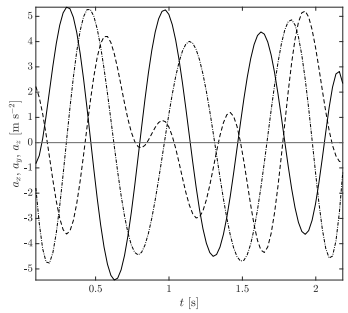

(l) Acceleration components.

Fig. 3.14 *Alsomitra macrocarpa* 1, 21, 23 and 26 that flew in a straight line.

full period of the motion was not always recorded. The vertical velocity component w has a negative value with small oscillations around the mean absolute value of $0.5\,\mathrm{m\,s^{-1}}$, in agreement with $0.41\,\mathrm{m\,s^{-1}}$ reported in the literature (Azuma and Okuno, 1987). The other two velocity components u and v, which belong to the motion on the horizontal plane, present oscillations in a range of absolute values spanning from $0\,\mathrm{m\,s^{-1}}$ to $1.50\,\mathrm{m\,s^{-1}}$. The acceleration components reported in figure 3.15 and figure 3.16 show a range of values admissible for seed dispersal (Minami and Azuma, 2003). Limitations on the time available prevented the analysis of velocity and acceleration components for the 5 diaspores in figure 3.17 and further analysis on the plots. Helical paths are a ubiquitous feature in nature (Lentink et al., 2007), the DNA molecule is made of two intertwined helices, climbing plants have helical appendages and a charged particle in a uniform magnetic field describes a helical trajectory. The majority of *Alsomitra macrocarpa* tested, 11, flew in a helical path, some with oscillations in the direction of flight similar to a phugoid, others in a smooth helix with a radius smaller than 1 m. This research focused on the four diaspores performing a straight gliding path, the three-dimensional helical flight will be the subject of future studies. In mathematics, a helix is a smooth space curve with tangent lines forming a constant angle to a fixed axis. In cartesian coordinates, the parametrisation used to fit the 3D coordinates collected by the depth cameras is:

$$x = R\cos(\omega t) \tag{3.3a}$$

$$y = R\sin(\omega t) \tag{3.3b}$$

$$z = wt \tag{3.3c}$$

where R is the radius of curvature and ω is the frequency. The instantaneous velocity and acceleration are obtained as the first and second derivatives of x, y and z versus time. The total velocity is $U = (R^2\omega^2 + w^2)^{0.5}$. Figure 3.21 shows, as an example, the fitting of the 3D trajectory, data points are represented by $\circ$ with the fitting curve described in equations 3.3.

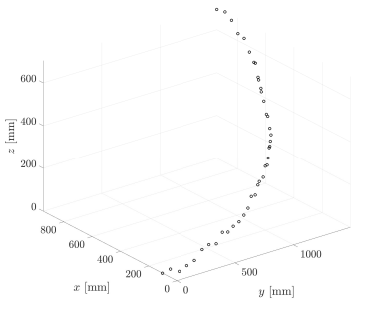

(a) Diaspore 2, 3D trajectory,

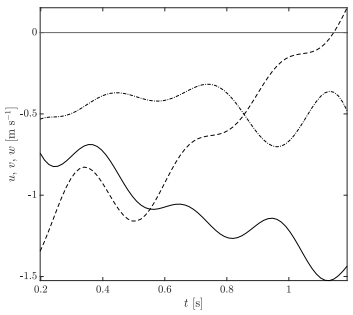

(b) Velocity components,

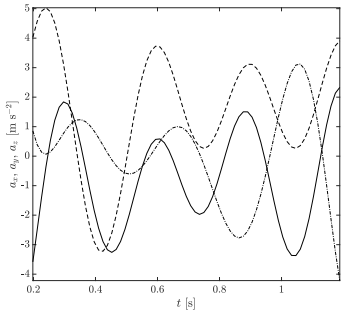

(c) Acceleration components.

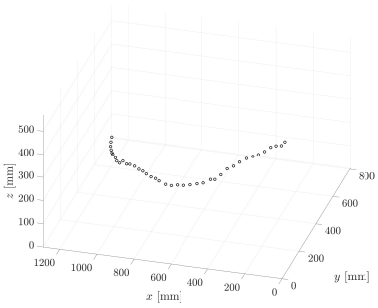

(d) Diaspore 12, 3D trajectory,

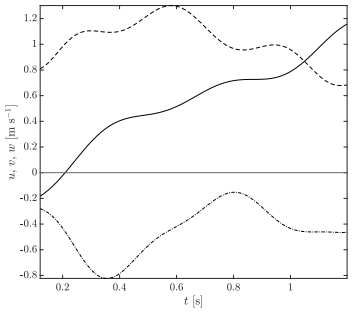

(e) Velocity components,

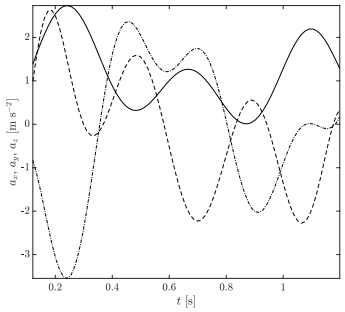

(f) Acceleration components.

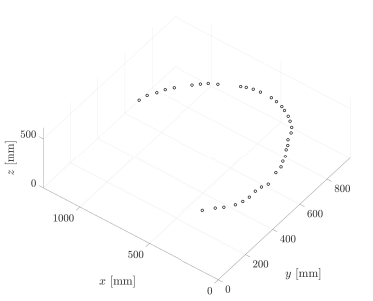

(g) Diaspore 15, 3D trajectory,

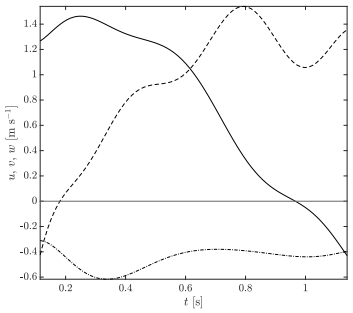

(h) Velocity components,

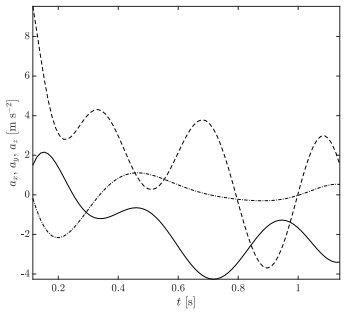

(i) Acceleration components.

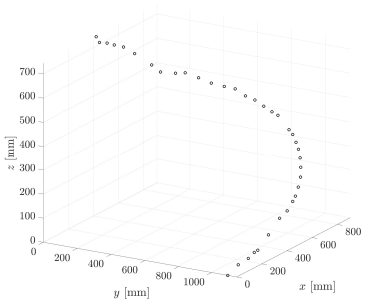

(j) Diaspore 25, 3D trajectory,

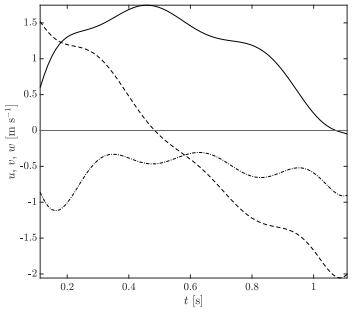

(k) Velocity components,

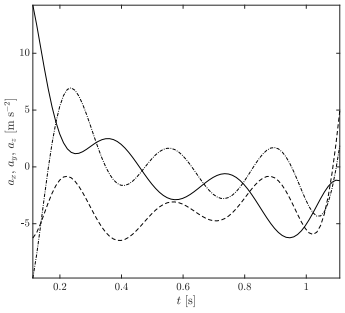

(l) Acceleration components.

Fig. 3.15 *Alsomitra macrocarpa* 2, 12, 15 and 25 that flew in a helical path.

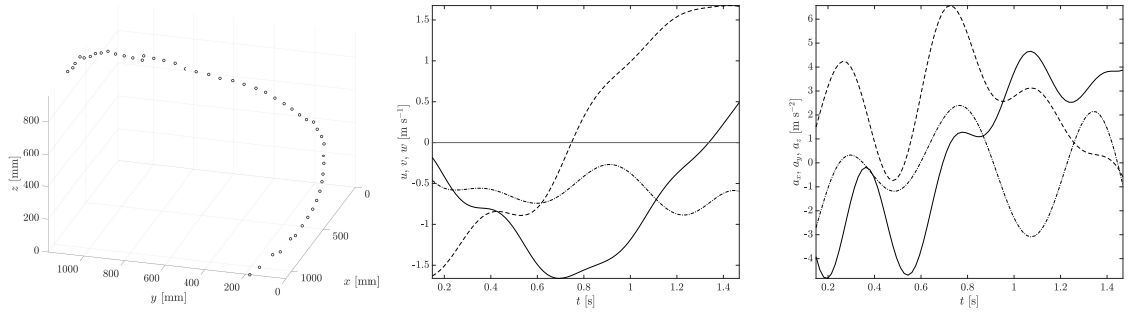

(a) Diaspore 27, 3D trajectory, (b) Velocity components, (c) Acceleration components.

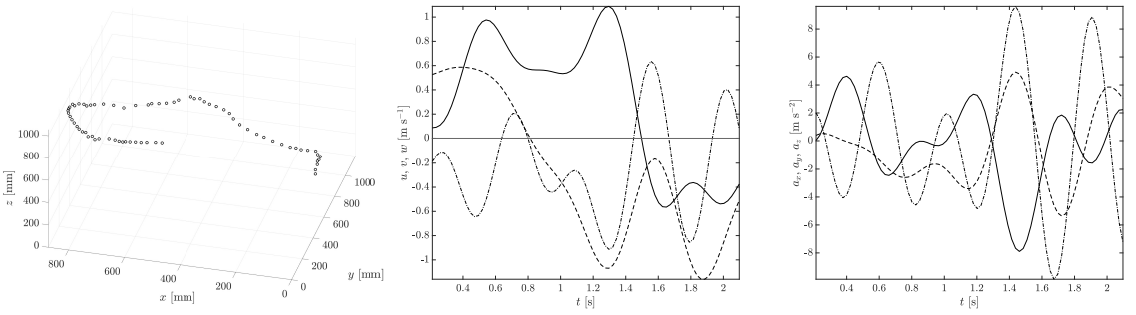

(d) Diaspore 31, 3D trajectory, (e) Velocity components, (f) Acceleration components.

Fig. 3.16 *Alsomitra macrocarpa* 27 and 31 that flew in a helical path.

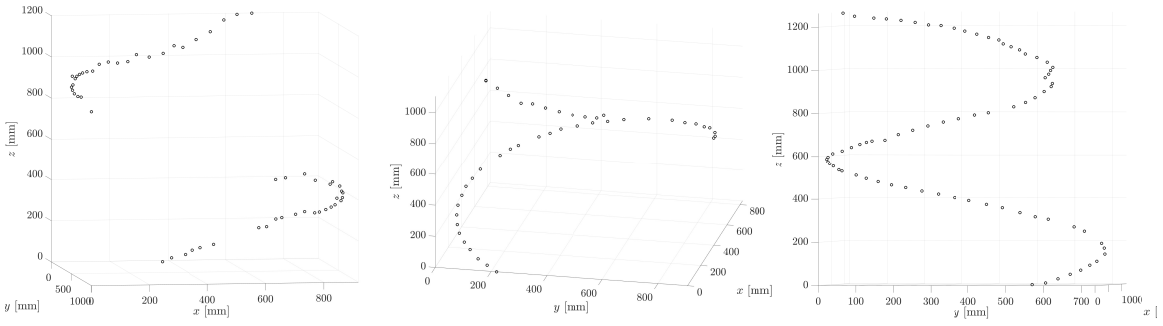

(a) Diaspore 4, 3D trajectory, (b) Diaspore 9, 3D trajectory, (c) Diaspore 10, 3D trajectory.

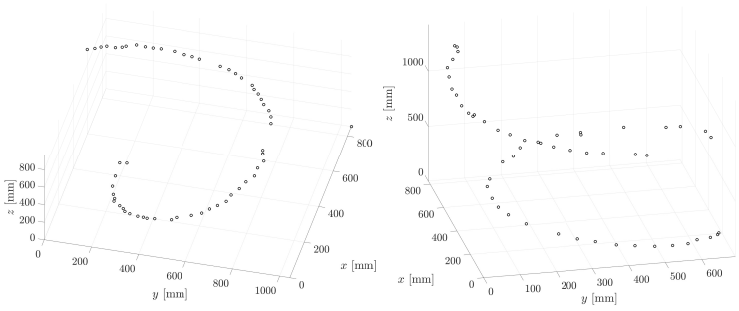

(d) Diaspore 18, 3D trajectory, (e) Diaspore 20, 3D trajectory

Fig. 3.17 *Alsomitra macrocarpa* 4, 9, 10, 18 and, 20 that flew in a helical path.

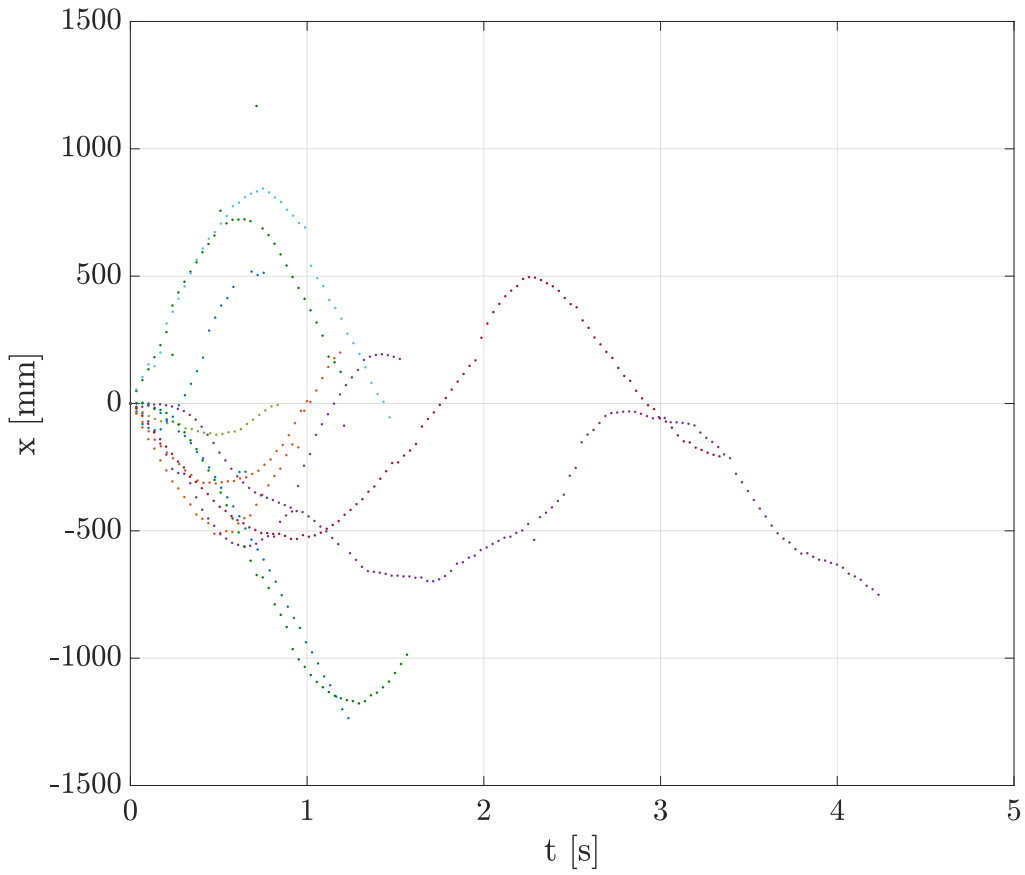

Fig. 3.18 Time series of the *x* component of the helical glide of 11 diaspores. Each glide is represented by a different colour.

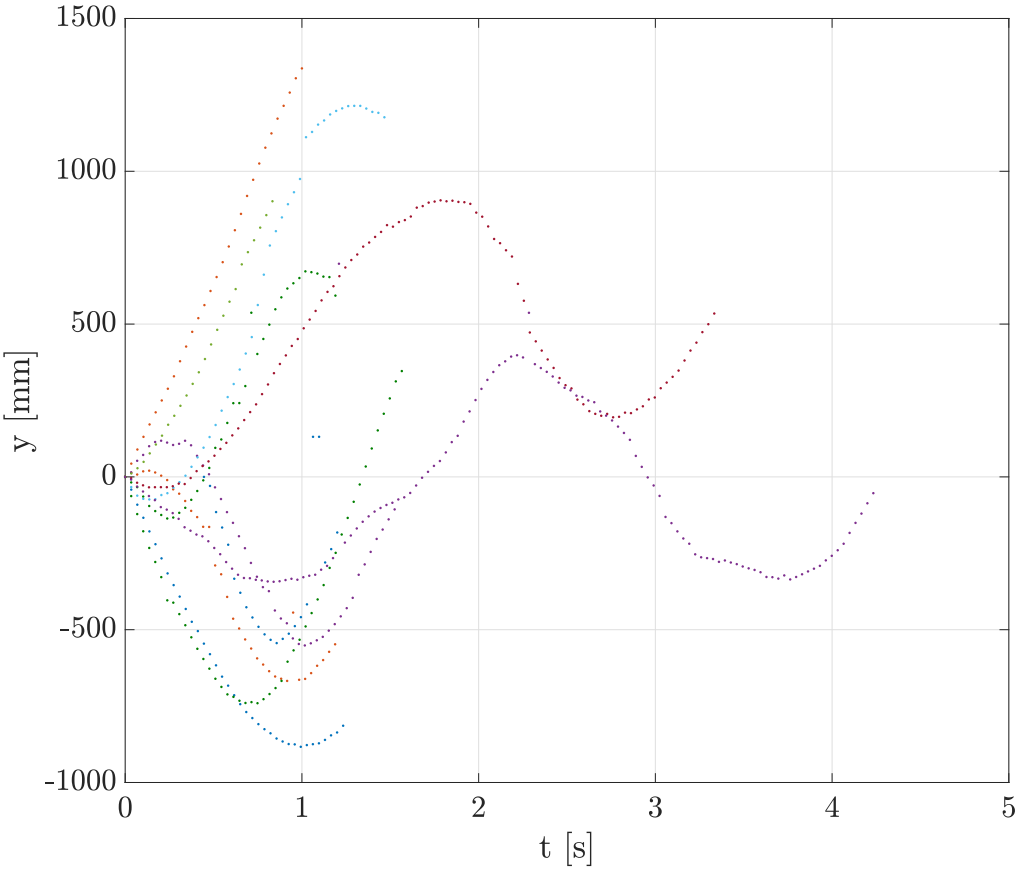

Fig. 3.19 Time series of the *y* component of the helical glide of 11 diaspores. Each glide is represented by a different colour.

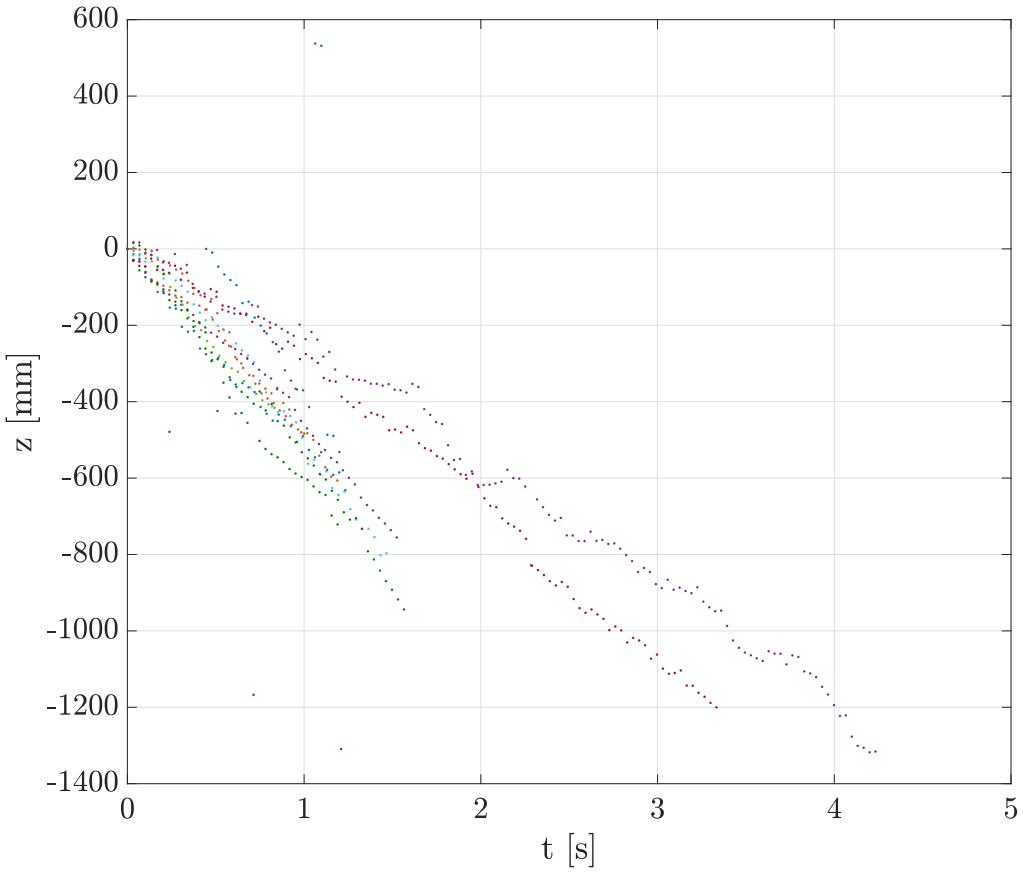

Fig. 3.20 Time series of the z component of the helical glide of 11 diaspores. Each glide is represented by a different colour.

Fig. 3.21 Two plots showing the three-dimensional helical path of Diaspore 2 and Diaspore 5. The discrete data points from the flights of two *Alsomitra macrocarpa* are fitted with equations 3.3.

Chapter 4

Discussion

4.1 A gentle glide

Winged seeds like black pine, maple, hornbeam and ash exhibit autorotation during their fall to the ground (Azuma and Yasuda, 1989; McCutchen, 1977). The gliding flight of *Alsomitra macrocarpa* was first studied by Ahlborn (1897) and subsequently by Azuma (2007); Azuma and Okuno (1987); Hagiwara (1992); Hertel (1966); Minami and Azuma (2003); Nachtigall (2011a, 2012) and Saito et al. (2008), who modelled the flight with the laws of equilibrium gliding. This specific form of gliding is based on the assumption that the glider, *Alsomitra macrocarpa* for instance, flies in equilibrium, hence in a steady state. This flight requires that lift and drag produce a total force of the same magnitude as the weight, but in opposite direction. Equilibrium gliding produces a linear glide path, at constant velocity and constant glide angle (Minami and Azuma, 2003). Aerodynamic forces depend on the squared value of velocity. Consequently, a specific speed is associated with each wing shape and orientation to develop a total force that precisely balances the weight. A constant gliding velocity is also associated with a fixed gliding angle (Bahlman et al., 2013). Gliding, straying and parachuting seeds, which are passive gliders (Minami and Azuma, 2003), reach their steady falling conditions after a short transient, a few body lengths from the release position (Seiichi et al., 2008). They behave as a falling object that eventually reaches terminal velocity. The non-equilibrium phases in steady gliding are present at the beginning of the glide, given the influence of the dynamics of take-off (Bahlman et al., 2013) and towards the end as a result of the ground effect. Azuma and Okuno (1987); Minami and Azuma (2003) and Nachtigall (2011a) recorded some of the parameters listed in table B.1, B.2 and B.3, but those descriptors characterise equilibrium gliding and do not address time-resolved changes. Time-resolved trajectories are needed to understand if the path, hence the velocity and acceleration components evolve during the flight (Bahlman et al., 2013). In the following

sections we look at the whole glide performance of 15 *Alsomitra macrocarpa*, most of them performed a helical glide while 4 a straight glide. Some diaspores flew with a lateral oscillation, known as "wing rock"in aeronautics. This oscillation was linked by Minami and Azuma (2003) to the nonlinear behaviour of the local separation point and lateral oscillations of vortex breakdown (Gresham et al., 2010).

4.1.1 Unsteady effects

A steady flow, like the one produced by a wind tunnel, could interact with a solid body and produce an unsteady flow. Vortex shedding behind a cylinder and self-excited oscillations of a flexible object are two examples (Vogel, 1996). Aircraft and gliding seeds can follow an oscillating path, composed of two under-damped oscillatory modes, with different time scales: the mode with a longer period and lightly damped is called phugoid mode. The descent or a local wind gust increases the speed and the lift, its effect is to stop the descent and slow the craft, reducing the lift and so forth. This alternation produces a wave-like path. It is commonly observed in model aeroplanes and gliders. *Alsomitra macrocarpa* is a pale species from Java, gliding in the forests of southeast Asia. Its habitat is made of forests up to 800 m, with rich soils along rivers (Singapore, 2021). This environment might be shielded by trees, but the air cannot be considered steady and the membrane wing is not rigid, as shown by the wind tunnel experiments performed in the Flow Visualisation Tunnel. This deformability of the membrane wing is another element that differentiate *Alsomitra macrocarpa* from a rigid flat plate. The study of the unsteady effects affecting the flight of seeds, insects and birds gives a better understanding of their flight (Godoy-Diana and Thiria, 2018). A rule of thumb suggested by Vogel (1996), helps to uncover if unsteady effects can be safely ignored. Vogel (1996) introduced a dimensionless parameter, the aerodynamic frequency parameter also named reduced frequency:

$$f_a = \frac{2\pi\omega_n c}{u_0}$$

where ω_n is the frequency of the oscillation and c is the chord at the wing centre. This parameter is a ratio of chord-wise flow speed to free stream speed u_0. It is usually high for short, broad wings, hence a low aspect ratio. A locust in full forward flight has the fore-wing operating at 0.25 and the hind-wing at about 0.5, same for a fruit fly wing (Vogel, 1996). Our samples, with a wing span of 171 mm, a chord of 70 mm and an aspect ratio of 2.84 have similar dimensions. The flight speed reported by (Azuma and Okuno, 1987) is $1.12\,\mathrm{m\,s^{-1}}$. The reduced frequency f_a is 0.48, extremely close to the 0.5, limit for unsteady effects to be negligible (Vogel, 1996). These calculations were executed with the morphological data

coming from the diaspores acquired, but the gliding properties documented in Azuma and Okuno (1987), a comparison with data produced by the drop tests tracked with depth cameras was not possible because of time constraints.

4.2 Results of the low order model

Falling paths

This section displays the computed (equations 2.38) falling trajectories of the centre of gravity of an elliptical body, with five different values of e (figure 2.23) and five different trajectories in the vertical plane. The dimensions of the semi-axes of the two ellipses are reported in table 2.3. The geometrical dimensions were kept constant, only the offset e, the distance between the centre of the exterior geometry O' and the centre of gravity O, was changed, figure 2.23. All the trajectories calculated were independent of the initial conditions in terms of the initial position; x and y and the angle θ that were set to zero. The trajectories highlighted a periodicity that emerged after a short transient. In figure 4.1, the two-dimensional trajectory of the elliptical body with a small offset, i.e. $e = 0.02$, is displayed. The efficiency E of the tumbling motion plotted in Fig. 4.1 is 1.04. The tumbling motion generates lift due to the "Magnus effect " (Magnus, 1853; Vincent et al., 2020a). Lift has a rotational contribution, a contribution similar to the Magnus effect (Li et al., 2022). This tumbling-induced horizontal displacement is part of the strategies employed by seeds like *Ailanthus altissima* to disperse (Vogel, 1996) and it does not rely on wind gusts, because of the lift generated. The behaviour of the falling body was changed, by displacing the centre of gravity of the ellipse by more than 10% of the ellipse semi-major axis a. The ellipse changed its flight path, instead of tumbling in the direction of the negative x axis, it fluttered. The shift of the centre of gravity, represented by the increase in the value of e, directly affected equation 2.38c, where the magnitude of the moment generated by the buoyancy force scales linearly with e. Figure 4.2 pictures the trajectory, similar to flutter (Pesavento, 2006), where the falling body alternates between gliding at a low angle of attack and fast rotational motion and centre of mass elevation at the turning points (Andersen et al., 2005a; Pesavento, 2006; Pesavento and Wang, 2004). Fluttering is characterised by symmetrical oscillations on the vertical plane, and because of these oscillations the horizontal displacement is always close to zero, hence the efficiency is close to zero. A further increase in the offset e to 0.36, leads to a falling trajectory that resembles that of *Alsomitra macrocarpa*, figure 4.3. The efficiency increased with respect to the fluttering motion. When the offset was increased to 0.91, as shown in figure 4.3 and to 0.97, in figure 4.4, the flight path converged towards an almost parabolic fall. The offset was further increased, and the torque generated by the displaced

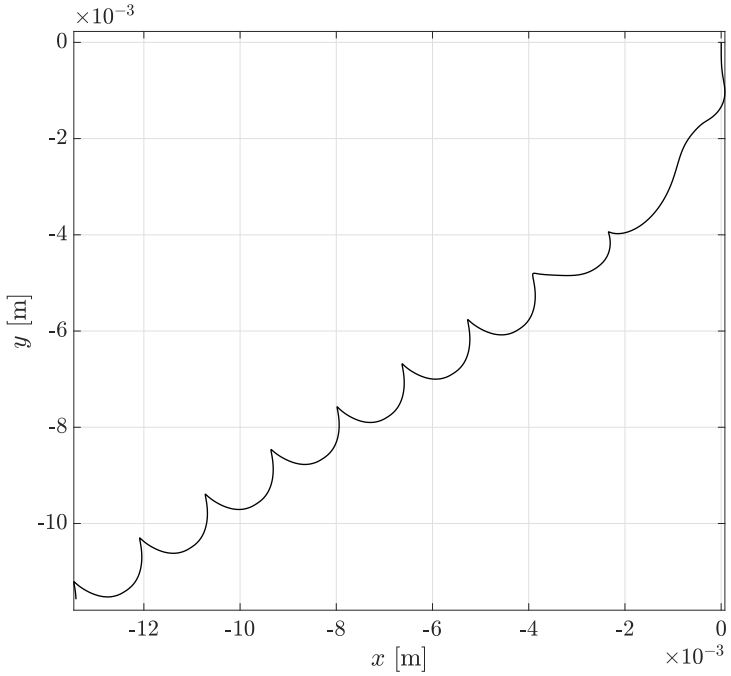

Fig. 4.1 Numerical solution of equations 2.38 for $e = 0.02$.

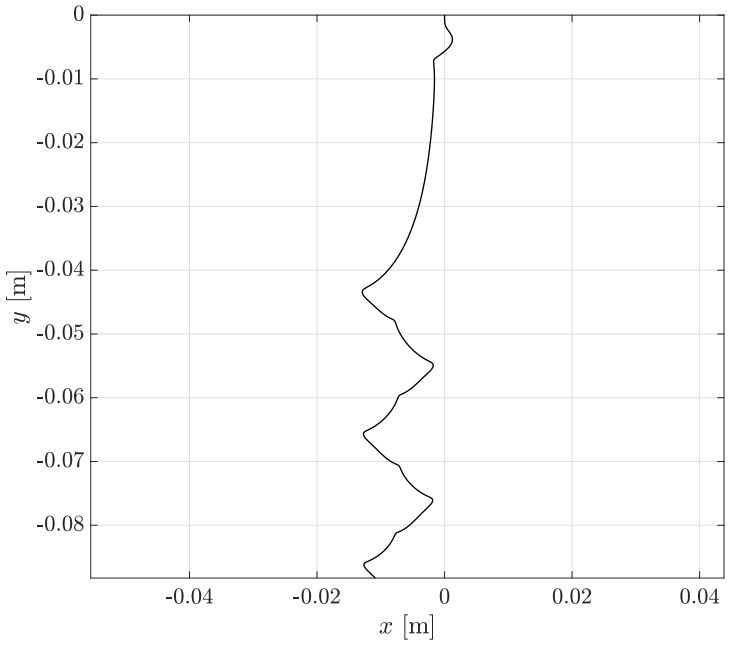

Fig. 4.2 Numerical solution of equations 2.38 for $e = 0.16$.

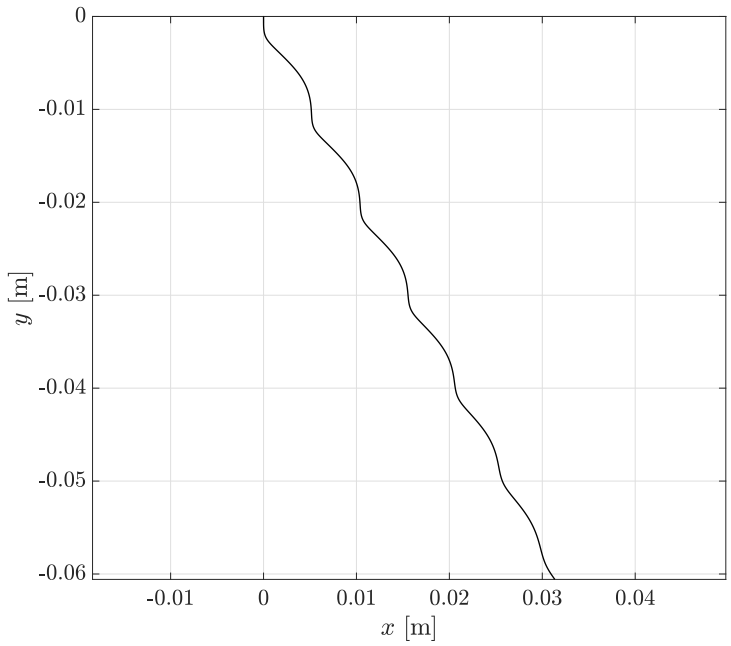

Fig. 4.3 Numerical solution of equations 2.38 for e = 0.36.

centre of mass became a relevant term in equation 2.38c. This flight path is an edge-on configuration, where the heavier side, the side of the elliptical shape where the centre of mass is located, points downward.

Temporal Dynamics

The temporal dynamics are discussed to better understand the falling trajectories plotted in figure 4.1, figure 4.3 and figure 4.4. Figure 4.3 presents a two-dimensional trajectory that resembles the trajectory displayed by *Alsomitra macrocarpa* in straight glide. Figure 4.6 plots the horizontal velocity component against time, in cases where e = 0.02, e = 0.36 and e = 0.91. The horizontal velocity component oscillates around a negative value when e = 0.02 and the ellipse performs a tumbling motion. The horizontal velocity oscillates around a positive value when e = 0.36 with the oscillation converging towards a constant positive velocity. When e = 0.91 the horizontal velocity is monotonically decreasing and tends to zero. The trajectory is not perfectly vertical and presents a horizontal displacement, hence the horizontal velocity different from zero. The damping is more pronounced when e = 0.36. Figure 4.7 shows the vertical velocity component related to the same cases. As expected it is negative for all three cases, but for the tumbling motion, e = 0.02, it presents periodic oscillations while for the case e = 0.36 the oscillations are damped. When e = 0.91

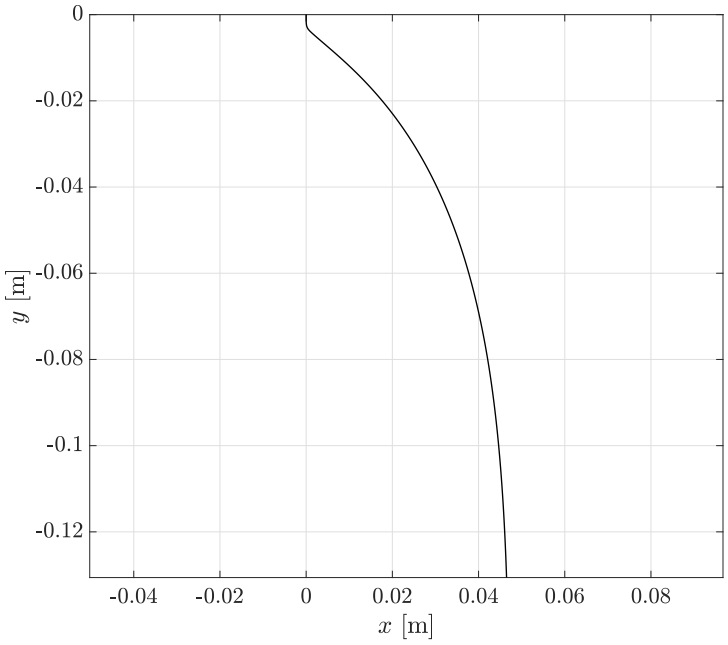

Fig. 4.4 Numerical solution of equations 2.38 for e = 0.91.

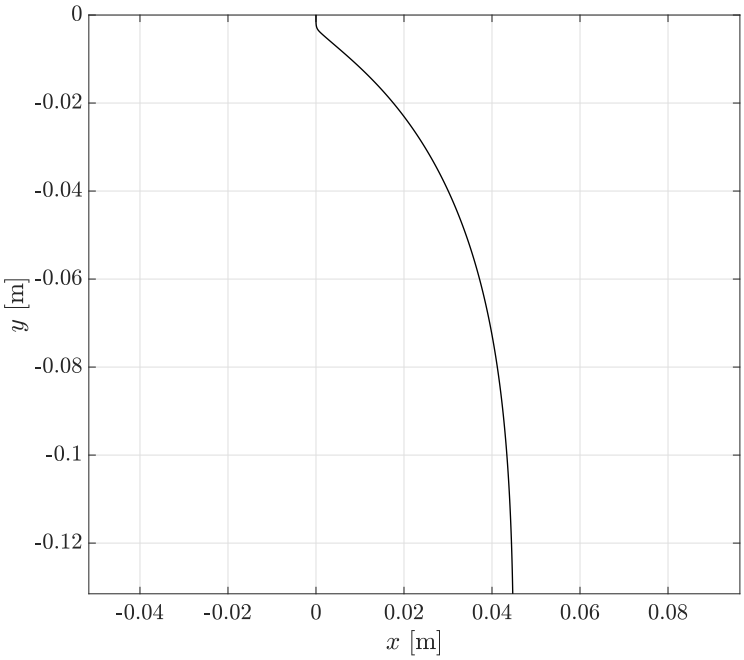

Fig. 4.5 Numerical solution of equations 2.38 for e = 0.97.

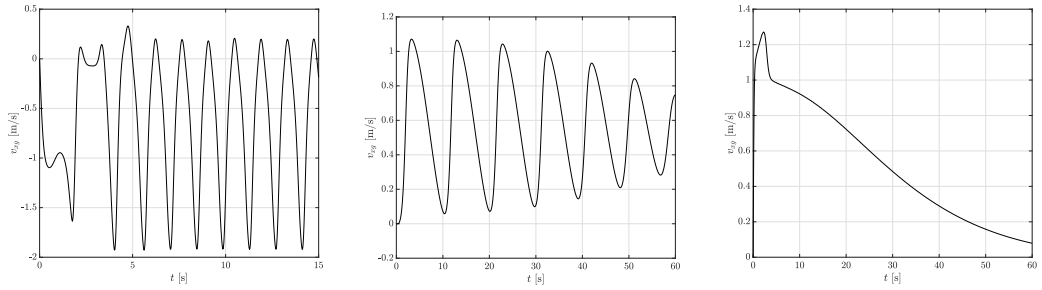

(a) Velocity u for $e = 0.02$. (b) Velocity u for $e = 0.36$. (c) Velocity u for $e = 0.91$.

Fig. 4.6 Temporal records of the horizontal velocity component u, in the laboratory reference frame, for two values of e.

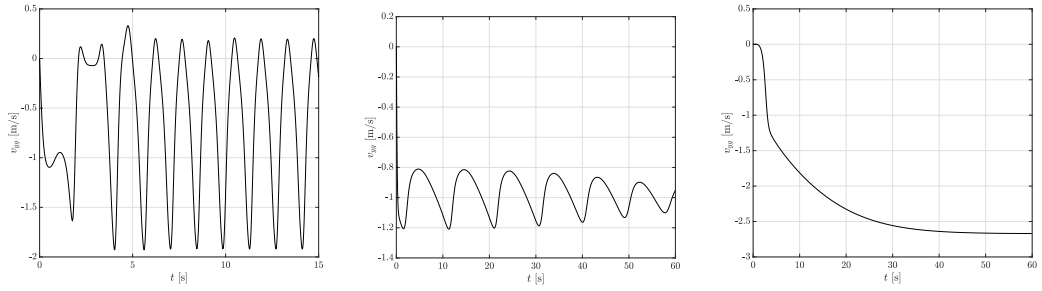

(a) Velocity v for $e = 0.02$. (b) Velocity v for $e = 0.36$. (c) Velocity v for $e = 0.91$.

Fig. 4.7 Temporal records of the vertical velocity component v, in the laboratory reference frame, for three values of e.

the vertical velocity component tends to a constant value, the terminal velocity of the falling body. The angular velocity in figure 4.8 shows a similar trend for $e = 0.02$ and $e = 0.36$. In tumbling motion, the angular velocity oscillates between negative values. The angular velocity ω for $e = 0.36$ presents damped oscillations around zero and for 0.91 tends to zero. The time dependence of the forces, Lift and Drag, is shown in figure 4.9. The rotational lift is plotted as a red line, while the translational lift is a blue line and drag is a black line. Rotational lift is a relevant part of the total lift produced in tumbling flight and becomes almost negligible for $e = 0.36$ and 0.91. The dependence over time of the four torques listed in equation 2.38 is shown by figure 4.10. The term $(m_{11} - m_{22})u_g v_g$ from ideal fluid theory is depicted by the black line. The term that takes into account the circulation Γ and describes the torque due to rotational and translational lift is represented by the red line, while the dissipative torque τ^v by the green line, the torque produced by buoyancy force acting at the centre of buoyancy is the blue line. In the three cases examined the ideal fluid torque produced the largest contribution and the dissipative torque tended to be negligible.

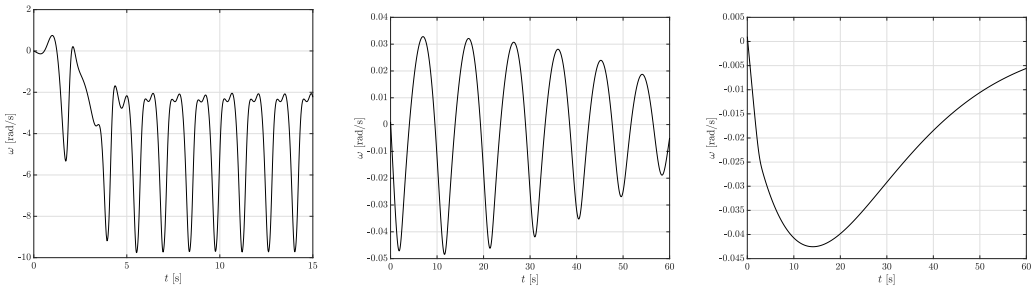

(a) ω for $e = 0.02$. (b) ω for $e = 0.36$. (c) ω for $e = 0.91$.

Fig. 4.8 Temporal records of the angular velocity ω for three values of e.

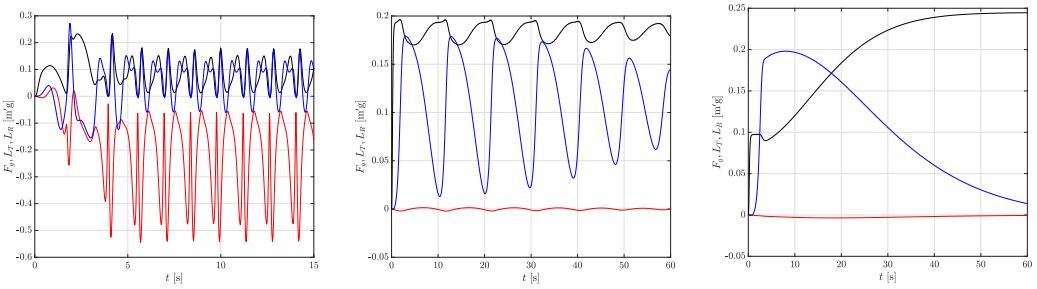

(a) Lift and Drag for $e = 0.02$. (b) Lift and Drag for $e = 0.36$. (c) Lift and Drag for $e = 0.91$.

Fig. 4.9 Temporal records of translational lift (blue), rotational lift (red), and drag (black) for three values of e.

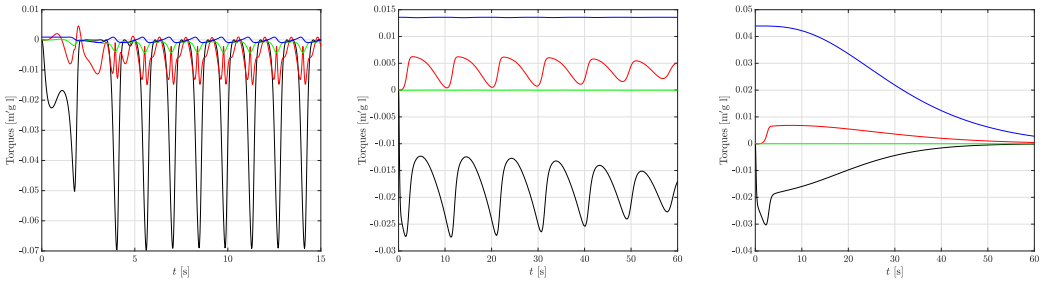

(a) Torque for $e = 0.02$. (b) Torque for $e = 0.36$. (c) Torque for $e = 0.91$.

Fig. 4.10 Temporal records of the total torque for three values of e. The term $(m_{11} - m_{22})\, u_g v_g$ from ideal fluid theory (black), the torque due to buoyancy force (blue), the dissipative torque (green) and the torque produced by translational and rotational lift (red).

4.3 Results of the simplified dynamics model

The simple model described in 2.15 can capture some of the behaviours seen in the straight glides depicted in figure 3.14. In this section, the trajectories computed from a simplified model, developed following Anderson Jr (2010); Torenbeek and Wittenberg (2009) are presented. The morphological dimensions of *Alsomitra macrocarpa*, listed in table 3.1, lead to the two-dimensional gliding paths displayed in figure 4.11. The dotted line represents a vertical fall similar to the vertical fall presented in figure 4.5, while the other three trajectories resemble the damped oscillations of figure 4.4. Static stability is guaranteed by the centre of mass being displaced with respect to the aerodynamic centre (Torenbeek and Wittenberg, 2009). Lift and drag act at the aerodynamic centre, located at a quarter chord from the leading edge, generating a moment with respect to the centre of mass, where weight W is applied (Anderson Jr, 2010). This assumption stands when the angle of attack α is small (Anderson Jr, 2010). The lift coefficient is $C_L = C_{Lmax}\sin(2\alpha)$ (Anderson Jr, 2010), while the drag coefficient is $C_D = C_{D0} + C_{Dmax}\sin(\alpha^2)$ (Anderson Jr, 2010). The dotted line ($\cdots$) displays the gliding path of a flat plate, while the empty circles ($\circ$), the black circles ($\bullet$) and the triangles ($\triangle$) depict the flight of a plate with camber, which generates an additional moment $M_0 = \frac{1}{2}\rho S c C_{M0} U^2$. The empty circles ($\circ$) correspond to a cambered plate with $C_{M0} = -0.0041$ while the black circles ($\bullet$) to $C_{M0} = -0.0047$ and the triangles to ($\triangle$) $C_{M0} = -0.0055$. The model assumes that the gliding flight happens at a small angle of attack α and C_{M0} is considered constant. This simple model captures parts of the gliding flight of the *Alsomitra macrocarpa* that flew in a straight line and were assumed to fly only in the vertical plane, without any motion in the lateral direction.

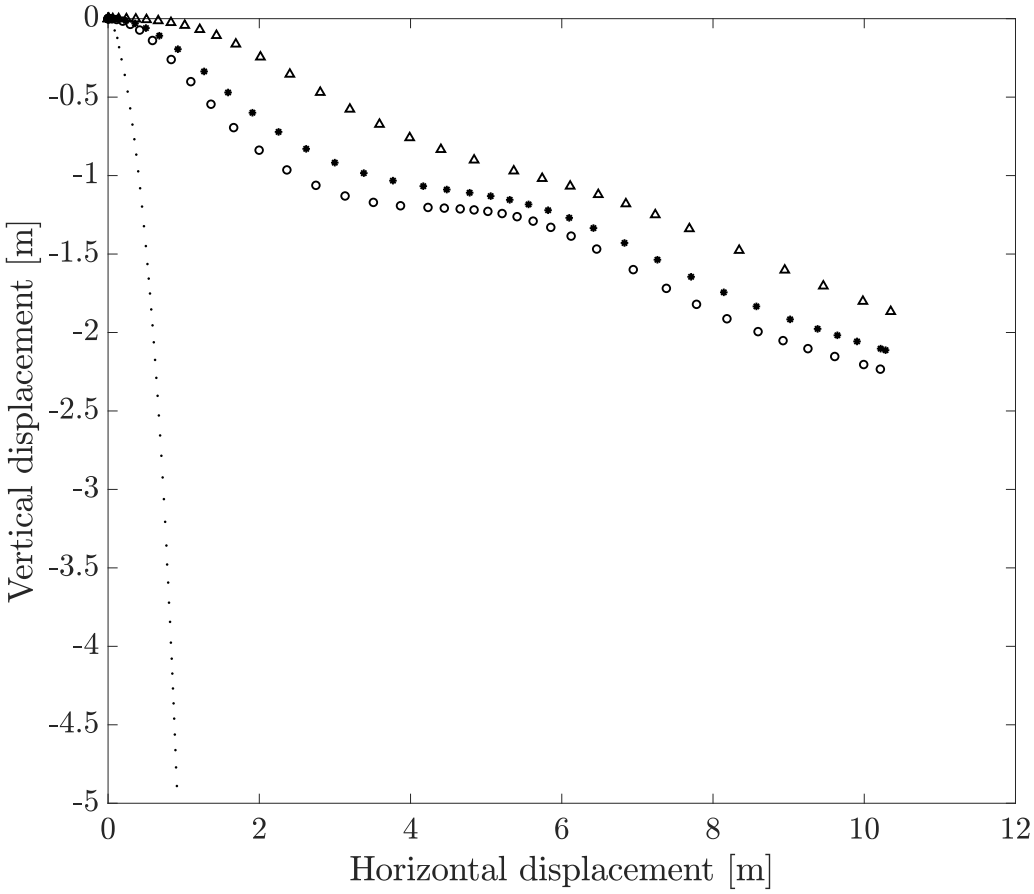

Fig. 4.11 Glide trajectories on the vertical plane.

Chapter 5

Conclusions

This study reveals some of the key morphological features of *Alsomitra macrocarpa* that enable its unique flight. Each diaspore shows either a straight or a helicoidal flight. Both types of flights can include a phugoid mode, which results in a lower terminal velocity. In figure 5.1 the *Alsomitra macrocarpa* that presented a phugoid mode are highlighted with a red circle (∘). Hence, the phugoid is not only a fluctuation around the mean flight path but could also be a feature that enhances the seed dispersal.

By modelling *Alsomitra macrocarpa* with a simplified dynamics, described in section 2.15, model we were able to capture the dynamics of the diaspores flying in a two-dimensional straight trajectory, reproducing some of the oscillations observed in the drop tests. The model of a two-dimensional ellipsoid with inhomogeneous mass distribution, showed that there is a range of positions of the centre of gravity with respect to the centre of buoyancy that allows the diaspore to glide without tumbling or falling in a parabolic motion.

Secondly, differently from what was previously thought, we discovered that *Alsomitra macrocarpa* has an intrados and an extrados. In fact, independently from the initial conditions, every diaspore always glides with the same face upwards as described in section 2.7.1. Hence, the wing of *Alsomitra macrocarpa* is not two-dimensional, nor is its airfoil symmetrical, hence it cannot be modelled as a rigid flat plate in order to capture this behaviour.

Thirdly, wind tunnel tests revealed significant wing deformations, which is critical to ensure pitch stability. In fact, coupled with the position of the centre of gravity, located in front of the aerodynamic centre, as a result of the wing swept, the upward displacement of the aerodynamic centre gives stability to the gliding flight.

Finally, we investigated the flow field around *Alsomitra macrocarpa* during a constrained flight in a wind tunnel. As described in section 3.5 the flow separates at the leading edge and recirculates between the corrugations of the wing, tip vortices were also detected.

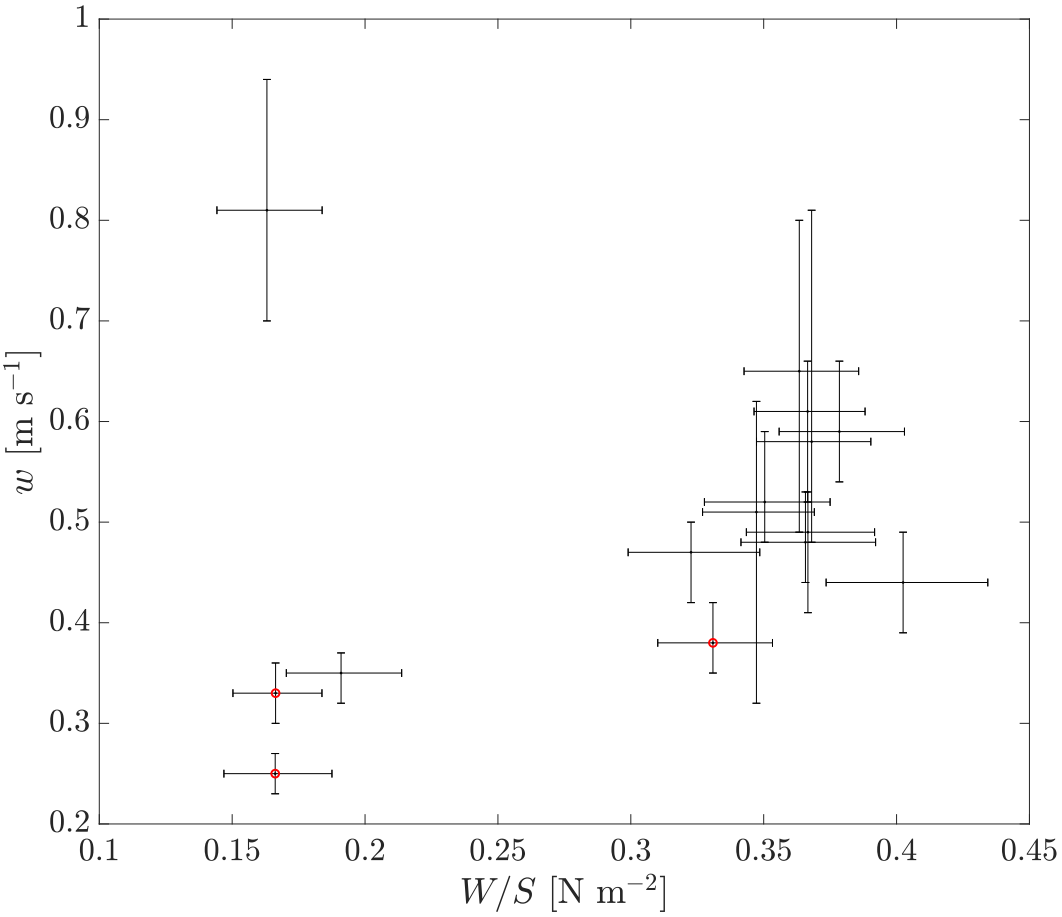

Fig. 5.1 Terminal velocity versus wing loading of the 15 *Alsomitra macrocarpa* tested. *Alsomitra macrocarpa* that showed a phugoid are represented by a red circle (○). Low wing loading and phugoid mode, are contributing factors to a lower terminal velocity.

In summary, this work provides new insights into the unique flight of *Alsomitra macrocarpa*, which may contribute to the design of future micro aerial vehicles.

Chapter 6

Future Work

6.1 Estimate of the aerodynamic parameters

To examine the aerodynamics of *Alsomitra macrocarpa* in greater detail, several aerodynamic parameters have to be calculated. The instantaneous glide angle $\gamma(t)$, for instance, could not be extracted, because of the noise in the interpolated data. A Savitzky-Golay filter (Schafer, 2011) could solve the problem (Galler and Rival, 2021). The angle between the horizontal and the net velocity vector gives the instantaneous glide angle (Bahlman et al., 2013).

$$\gamma = \arctan\left(\frac{w}{u}\right), \tag{6.1}$$

where w is the vertical component of the velocity vector and u is the horizontal component. The instantaneous values of Lift (L), the aerodynamic force perpendicular to the direction of flight, and Drag (D) the aerodynamic force perpendicular to lift, are then determined from the following equations

$$L = m\left(a_x \sin(\gamma) + a_z \cos(\gamma)\right), \tag{6.2}$$

and

$$D = m\left(a_z \sin(\gamma) + a_x \cos(\gamma)\right), \tag{6.3}$$

where m represents the mass of each diaspore, a_x and a_z are the horizontal and vertical components of the instantaneous acceleration. This information allows the extraction of the lift coefficient (C_L) and drag coefficient (C_D) as function of time t

$$C_\mathrm{L} = \frac{L}{1/2\rho U^2 S} \tag{6.4}$$

and

$$C_{\mathrm{D}} = \frac{D}{1/2\rho U^2 S} \tag{6.5}$$

with U being the total velocity, ρ air density and S the surface area of the body. The dependence of the Efficiency (E), lift-to-drag ratio is

$$E = \frac{C_L}{C_D} \tag{6.6}$$

The interplay between kinetic energy (E_k), potential energy (E_p) and total energy (E_T), normalised by the body mass m is written as follows

$$\begin{aligned} \frac{E_{\mathrm{P}}}{m} &= gh \\ \frac{E_{\mathrm{K}}}{m} &= \frac{1}{2}U^2 \\ \frac{E_{\mathrm{T}}}{m} = \frac{E_{\mathrm{P}}}{m} + \frac{E_{\mathrm{K}}}{m} &= gh + \frac{1}{2}U^2 \end{aligned} \tag{6.7}$$

where the height of the gliding path, above an arbitrarily chosen reference height, the ground of the laboratory for instance, is h. When the diaspore takes off the total energy is simply potential energy, because the initial total velocity is zero. With the aerodynamic coefficients derived from equations 6.4 and 6.5, it would be possible to derive a low-order model of the flight of *Alsomitra macrocarpa*. The model developed by Andersen et al. (2005a,b) assumes a homogeneous mass distribution and a constant density, but this is not the case for biological organisms. *Alsomitra macrocarpa* has most of its mass concentrated in the seed containing pericarp. Experiments proved that the centre of mass of our 31 *Alsomitra macrocarpa* is located in the seed containing pericarp. The centre of mass position in our 2D model replicated this positioning. The planar shape, similar to an inverse Zimmerman (Chen and Qin, 2013) moves the aerodynamic centre backwards. The distance between the aerodynamic centre and the centre of mass is a key requisite for static stability and causes an external torque which breaks the symmetry of the rotational motion, moves the mean tilting position from the horizontal plane and causes a horizontal displacement (Huang et al., 2013; Li et al., 2022). The offsetting of aerodynamic centre and centre of mass experienced by *Alsomitra macrocarpa* in gliding flight has a longitudinal and a vertical component. The deformation moves the aerodynamic centre along the vertical axis and generates an external torque that alters the fluttering dynamics. The position of the seed containing pericarp prescribes the location of the centre of mass along the longitudinal axis.

6.2 Collaborations

A collaboration with Professor Mintchev at ETH Zurich was established to understand the super-stability of *Alsomitra macrocarpa*. The stability of *Alsomitra macrocarpa*, its dynamic response to impacts and critical stability loss is promising for the design of bio-inspired drones operating in cluttered environments. Preliminary experiments highlighted the capability of *Alsomitra macrocarpa* to recover stable gliding flight from stall or spin. The collaboration will focus on understanding the contribution of morphology and aerodynamics to the quick recovery of stable gliding flight with the end goal of designing a novel type of unmanned aerial vehicle with inherently superior dynamic stability.

A collaboration with Dr Alam at the University of Edinburgh will characterise the physical, material and mechanical properties of the membrane wing of *Alsomitra marocarpa* to absorb impacts and deform, dissipating the energy without breaking. The aim would be to reproduce these mechanical properties of the membrane wing in a bio-inspired material.

A collaboration with Dr Zhdanov and Dr Busse at the University of Glasgow aims at investigating the contribution of the rough surface of the membrane wing to the flow field, using direct numerical simulations. The experiments performed in the wind tunnel at the University of Glasgow showed promising results and highlighted all the limitations of an experimental approach, hence the necessity to tackle the problem numerically.

Appendix A

Morphological Analysis

In this appendix chapter the morphological and geometrical values of 31*Alsomitra macrocarpa* are presented.

Table A.1 Principal dimensions measured on 31 *Alsomitra macrocarpa*.

Diaspore Accuracy	Mass, m [g] ± 0.01	Wing-span, b [mm] ± 2	Wing-chord on the roll axis, c_{centre} [mm] ± 1
1	0.36	162	64
2	0.39	167	70
3	0.33	153	60
4	0.14	159	54
5	0.41	178	81
6	0.39	152	68
7	0.46	168	78
8	0.41	171	75
9	0.45	182	85
10	0.37	176	65
11	0.42	175	81
12	0.31	166	66
13	0.38	177	63
14	0.38	172	70
15	0.44	178	76
16	0.41	177	76
17	0.31	166	66
18	0.16	154	58
19	0.42	178	84
20	0.43	186	74
21	0.37	188	71
22	0.38	191	68
23	0.37	178	67
24	0.37	178	78
25	0.42	176	79
26	0.17	170	68
27	0.41	171	70
28	0.42	171	71
29	0.45	169	76
30	0.30	161	59
31	0.14	158	61

Table A.2 Principal dimensions measured on 31 *Alsomitra macrocarpa*.

Diaspore	Wing surface, S [mm^2]	Geometrical sweep angle, Λ [deg]	Centre of gravity, CG [mm]
Accuracy	$\pm$200	$\pm$1	$\pm$1
1	87750	18	21
2	10435	20	22
3	80090	21	23
4	84220	16	22
5	11380	19	21
6	88130	17	20
7	10238	19	20
8	10523	17	22
9	12044	18	24
10	99250	17	24
11	97410	17	23
12	94250	18	23
13	97240	17	23
14	10205	15	22
15	11728	15	22
16	11248	17	23
17	94780	18	24
18	82190	16	24
19	11950	18	23
20	11608	16	23
21	10969	15	24
22	11471	22	22
23	10359	20	21
24	11459	16	20
25	10886	17	21
26	10026	15	22
27	11582	19	22
28	11582	20	23
29	10875	17	23
30	82100	18	23
31	82640	15	23

Table A.3 Values describing the planar form of 31 *Alsomitra macrocarpa*.

Diaspore	Fluctuating Asymmetry	Roundness	Circularity	Solidity
1	0.01	1.92	0.58	0.90
2	1.44	1.72	0.63	0.89
3	1.60	1.75	0.63	0.88
4	1.36	1.59	0.62	0.90
5	1.06	1.83	0.62	0.94
6	1.09	1.25	0.66	0.90
7	0.00	1.64	0.58	0.88
8	0.89	1.89	0.67	0.94
9	0.00	1.69	0.68	0.94
10	0.00	1.64	0.59	0.90
11	0.00	1.64	0.59	0.90
12	1.20	1.91	0.65	0.92
13	1.25	2.10	0.63	0.92
14	Missing	Missing	Missing	Missing
15	1.17	1.44	0.63	0.91
16	1.02	1.69	0.69	0.94
17	0.00	1.58	0.65	0.91
18	0.00	1.86	0.66	0.94
19	0.00	1.44	0.61	0.92
20	1.17	2.06	0.63	0.94
21	0.01	1.69	0.49	0.88
22	1.75	1.64	0.45	0.83
23	1.96	1.63	0.47	0.83
24	Missing	Missing	Missing	Missing
25	1.01	1.70	0.61	0.93
26	0.00	1.61	0.55	0.88
27	1.48	1.63	0.64	0.91
28	1.48	1.63	0.64	0.91
29	0.00	1.73	0.64	0.93
30	1.37	1.57	0.58	0.88
31	0.94	2.10	0.64	0.93

Table A.4 Geometrical configuration of 31 *Alsomitra macrocarpa*.

Diaspore	Aspect ratio, AR	Mean geometric chord, $m.g.c.$ [mm]	Wing loading, W/S [$\mathrm{N\,m^{-2}}$]	Density, ρ [$\mathrm{g\,m^{-2}}$]
1	3.0	54	0.409	41
2	2.6	62	0.392	37
3	2.9	52	0.400	41
4	3.1	53	0.170	17
5	2.7	64	0.368	36
6	2.8	58	0.430	44
7	2.8	61	0.415	45
8	2.8	62	0.394	39
9	2.6	66	0.396	37
10	3.1	56	0.381	37
11	2.6	56	0.366	43
12	2.8	57	0.335	33
13	3.1	55	0.394	39
14	2.9	59	0.365	37
15	2.6	66	0.394	38
16	2.7	64	0.373	36
17	2.9	57	0.331	33
18	2.9	53	0.198	19
19	2.5	67	0.368	35
20	2.8	62	0.376	37
21	3.1	58	0.329	34
22	3.2	60	0.333	33
23	3.1	58	0.349	36
24	2.8	64	0.317	32
25	2.8	62	0.381	39
26	2.9	59	0.178	17
27	2.8	68	0.399	35
28	2.4	68	0.368	36
29	2.6	64	0.404	41
30	3.2	51	0.362	37
31	3.0	52	0.172	17

Appendix B

Flight test results

In this appendix chapter the average flight performance for *Alsomitra macrocarpa* is presented.

Table B.1 Results from the flight tests of 4 *Alsomitra macrocarpa* gliding in a straight path.

Diaspore	Drop	Terminal velocity [$m\,s^{-1}$]	Total velocity [$m\,s^{-1}$]	Gliding angle [deg]
1	1	0.37	1.41	15
	2	0.42	1.38	18
	3	0.52	1.33	23
	4	0.40	1.40	17
	5	0.47	1.47	19
21	1	0.39	0.85	27
	2	0.33	0.74	26
	3	0.42	0.86	29
	4	0.47	0.90	31
	5	0.41	0.90	27
	6	0.32	0.82	23
	7	0.33	0.75	26
23	1	0.39	1.15	20
	2	0.48	1.70	16
	3	0.63	1.87	19
	4	0.45	1.59	17
	5	0.53	1.72	18
	6	0.53	1.69	18
26	1	0.32	0.81	23
	2	0.34	0.72	28
	3	0.38	0.81	28
	4	0.26	0.60	26
	5	0.34	0.69	29
	6	0.35	0.73	28

Table B.2 Results from the flight tests of 6 *Alsomitra macrocarpa* gliding in a helical path.

Diaspore	Drop	Terminal velocity $m\,s^{-1}$	Radius of curvature m
2	1	0.53	1.078
	2	0.49	0.746
	3	0.54	1.574
	4	0.38	Missing
	5	0.53	1.004
4	1	0.75	0.381
	2	0.91	0.363
	3	0.74	0.358
	4	1.02	0.529
	5	0.64	0.518
9	1	0.57	0.428
	2	0.67	0.452
	3	0.46	0.406
	4	0.64	0.470
	5	0.66	0.507
	6	0.66	0.454
10	1	0.58	0.373
	2	0.44	0.338
	3	0.51	0.323
	4	0.42	0.380
	5	0.43	0.351
	6	0.51	0.310
12	1	0.52	0.915
	2	0.39	0.903
	3	0.50	1.342
	4	0.47	1.489
	5	0.45	0.978
15	1	0.44	0.620
	2	0.54	0.646
	3	0.46	0.739
	4	0.54	0.722
	5	0.90	0.896

Table B.3 Results from the flight tests of 5 *Alsomitra macrocarpa* gliding in a helical path.

Diaspore	Drop	Terminal velocity $m\,s^{-1}$	Radius of curvature m
18	1	0.38	0.430
	2	0.33	0.362
	3	0.34	0.353
	4	0.31	0.309
	5	0.38	0.233
20	1	0.68	0.305
	2	0.87	0.315
	3	0.60	0.298
	4	Missing	Missing
	5	0.43	0.289
25	1	0.51	0.847
	2	0.62	0.599
	3	0.57	0.602
	4	0.70	0.460
	5	0.56	0.462
27	1	0.62	0.567
	2	0.56	0.521
	3	0.69	0.589
	4	0.47	0.497
	5	0.22	0.505
31	1	0.23	0.322
	2	0.28	0.353
	3	0.23	0.238
	4	0.28	0.347
	5	0.24	Missing
	6	0.23	0.512

References

Ahlborn, F. (1897). Abhandl, aus dem bebiete der naturwissenschaften.

Alba, V., Carthew, J. E., Carthew, R. W., and Mani, M. (2021). Global constraints within the developmental program of the drosophila wing. *Elife*, 10:e66750.

Alexander, R. (1982). Locomotion of animals. *Glasgow: Blackie*.

Andersen, A., Pesavento, U., and Wang, Z. J. (2005a). Analysis of transitions between fluttering, tumbling and steady descent of falling cards. *Journal of Fluid Mechanics*, 541(1):91–104.

Andersen, A., Pesavento, U., and Wang, Z. J. (2005b). Unsteady aerodynamics of fluttering and tumbling plates. *Journal of Fluid Mechanics*, 541:65–90.

Anderson Jr, J. D. (2010). *Fundamentals of aerodynamics*. Tata McGraw-Hill Education.

Aref, H. and Jones, S. W. (1993). Chaotic motion of a solid through ideal fluid. *Physics of Fluids A: Fluid Dynamics*, 5(12):3026–3028.

Attenborough, D. (1995). *The private life of plants: a natural history of plant behaviour*. BBC Books.

Azuma, A. (2007). Flight of seeds, flying fish, squid, mammals, amphibians and reptiles. *Flow Phenomena in Nature: A challenge to engineering design*, 1:88.

Azuma, A. and Okuno, Y. (1987). Flight of a samara, alsomitra macrocarpa. *Journal of Theoretical Biology*, 129(3):263–274.

Azuma, A. and Yasuda, K. (1989). Flight performance of rotary seeds. *Journal of Theoretical Biology*, 138(1):23–53.

Bahlman, J. W., Swartz, S. M., Riskin, D. K., and Breuer, K. S. (2013). Glide performance and aerodynamics of non-equilibrium glides in northern flying squirrels (glaucomys sabrinus). *Journal of The Royal Society Interface*, 10(80):20120794.

Barba, L. (2011). Bio-aerial locomotion 2011.

Bateman, R. M. and Rudall, P. J. (2006). Evolutionary and morphometric implications of morphological variation among flowers within an inflorescence: a case-study using european orchids. *Annals of botany*, 98(5):975–993.

BBC (2009). Life: Plants.

References

BBC (2016). Life in the air: Defying gravity.

Belmonte, A., Eisenberg, H., and Moses, E. (1998). From flutter to tumble: inertial drag and froude similarity in falling paper. *Physical Review Letters*, 81(2):345.

Boyd, A. (2002). Morphological analysis of sky island populations of macromeria viridiflora (boraginaceae). *Systematic Botany*, pages 116–126.

Caple, J., Byrd, J., and Stephan, C. N. (2017). Elliptical fourier analysis: fundamentals, applications, and value for forensic anthropology. *International Journal of Legal Medicine*, 131(6):1675–1690.

Casseau, V., De Croon, G., Izzo, D., and Pandolfi, C. (2015). Morphologic and aerodynamic considerations regarding the plumed seeds of tragopogon pratensis and their implications for seed dispersal. *PloS one*, 10(5):e0125040.

Certini, D., Fazan, L., Nakayama, N., Viola, I. M., and Kozlowski, G. (2020). Velocity of the falling dispersal units in zelkova abelicea: remarkable evolutionary conservation within the relict tree genus. *American Journal of Botany*, 107(12):1831–1838.

Chen, M. and McMasters, J. (1981). From paleoaeronautics to altostratus-a technical history of soaring. In *Aircraft Systems and Technology Conference*, page 1611.

Chen, Z. and Qin, N. (2013). Planform effects for low-reynolds-number thin wings with positive and reflex cambers. *Journal of aircraft*, 50(3):952–964.

Chitwood, D. H. and Otoni, W. C. (2017). Morphometric analysis of passiflora leaves: the relationship between landmarks of the vasculature and elliptical fourier descriptors of the blade. *GigaScience*, 6(1):giw008.

Chuanromanee, T. S., Cohen, J. I., and Ryan, G. L. (2019). Morphological analysis of size and shape (mass): An integrative software program for morphometric analyses of leaves. *Applications in Plant Sciences*, 7(9):e11288.

Church, N. S. (1960). Heat loss and the body temperatures of flying insects: Ii. heat conduction within the body and its loss by radiation and convection. *Journal of Experimental Biology*, 37(1):186–212.

Combes, S. and Daniel, T. (2003a). Flexural stiffness in insect wings i. scaling and the influence of wing venation. *Journal of experimental biology*, 206(17):2979–2987.

Combes, S. and Daniel, T. (2003b). Flexural stiffness in insect wings ii. spatial distribution and dynamic wing bending. *Journal of Experimental Biology*, 206(17):2989–2997.

Cummins, C., Seale, M., Macente, A., Certini, D., Mastropaolo, E., Viola, I. M., and Nakayama, N. (2018). A separated vortex ring underlies the flight of the dandelion. *Nature*, 562(7727):414.

de Oliveira, R. R., Campos, F. L., and de Andrade, I. M. (2016). Foliar morphometric study of jatropha curcas l.(euphorbiaceae). *Journal of Plant Sciences*, 4(2):23–28.

Egli, B. (1997). A project for the preservation of zelkova abelicea (ulmaceae), a threatened endemic tree species from the mountains of crete. *Bocconea*, 5(2):505–510.

Ellington, C. P. (1984). The aerodynamics of hovering insect flight. vi. lift and power requirements. *Philosophical Transactions of the Royal Society of London. B, Biological Sciences*, 305(1122):145–181.

Ennos, A. R. (1989). The effect of size on the optimal shapes of gliding insects and seeds. *Journal of Zoology*, 219(1):61–69.

Faisal, A. and Filippone, A. (2016a). Aerodynamic model for insect flapping wings with induced flow effect. *Journal of Aircraft*, 53(3):701–712.

Faisal, A. and Filippone, A. (2016b). Aerodynamic model for tandem flapping wings. *AIAA Journal*, 54(12):3849–3858.

Floreano, D. and Wood, R. J. (2015). Science, technology and the future of small autonomous drones. *Nature*, 521(7553):460.

Galler, J. N. and Rival, D. E. (2021). Characterization of milkweed-seed gust response. *Bioinspiration & biomimetics*, 16(6):066017.

Gardens, K. R. B. (2022). Alsomitra macrocarpa (blume) m.roem.: Plants of the world online: Kew science.

Giuni, M. and Green, R. B. (2013). Vortex formation on squared and rounded tip. *Aerospace science and technology*, 29(1):191–199.

Godoy-Diana, R. and Thiria, B. (2018). On the diverse roles of fluid dynamic drag in animal swimming and flying. *Journal of The Royal Society Interface*, 15(139):20170715.

Gómez, J. M., Torices, R., Lorite, J., Klingenberg, C. P., and Perfectti, F. (2016). The role of pollinators in the evolution of corolla shape variation, disparity and integration in a highly diversified plant family with a conserved floral bauplan. *Annals of Botany*, 117(5):889–904.

Green, R., Doolan, C., and Cannon, R. (2000). Measurements of the orthogonal blade–vortex interaction using a particle image velocimetry technique. *Experiments in Fluids*, 29(4):369–379.

Green, R. B., Gillies, E. A., and Brown, R. E. (2005). The flow field around a rotor in axial descent. *Journal of Fluid Mechanics*, 534:237–261.

Gresham, N. T., Wang, Z., and Gursul, I. (2010). Low reynolds number aerodynamics of free-to-roll low aspect ratio wings. *Experiments in Fluids*, 49(1):11–25.

Hagiwara, S. (1992). A seed model of glinder tree, alsomitra macrocarpa roem. *Rept. Inst. Nat. Stu.*, 23:11–20.

Hedrick, T. L. (2008). Software techniques for two-and three-dimensional kinematic measurements of biological and biomimetic systems. *Bioinspiration & biomimetics*, 3(3):034001.

Hertel, H. (1966). *Structure, form, movement*. Reinhold.

Howe, H. F. and Smallwood, J. (1982). Ecology of seed dispersal. *Annual review of ecology and systematics*, 13:201–228.

Huang, W., Liu, H., Wang, F., Wu, J., and Zhang, H. (2013). Experimetal study of a freely falling plate with an inhomogeneous mass distribution. *Physical Review E*, 88(5):053008.

Innes, D. and Bates, J. (1999). Morphological variation of mytilus edulis and mytilus trossulus in eastern newfoundland. *Marine Biology*, 133(4):691–699.

ITHAKA (2022). Jstor global plants.

Karasik, A., Rahimi, O., David, M., Weiss, E., and Drori, E. (2018). Development of a 3d seed morphological tool for grapevine variety identification, and its comparison with ssr analysis. *Scientific reports*, 8(1):1–9.

Kirchhoff, G. (1882). *Collected Work*. Barth, Leipzig.

Klein, L. L. and Svoboda, H. T. (2017). Comprehensive methods for leaf geometric morphometric analyses. *Bio-protocol*, 7:e2269.

Knippers, J., Nickel, K. G., and Speck, T. (2016). Biomimetic research for architecture and building construction. *Switzerland: Springer International Publishing*.

Kozlov, V. (1989). Heavy rigid body falling in an ideal fluid. *Mech. Solids*, 24(5):9–17.

Kuhl, F. P. and Giardina, C. R. (1982). Elliptic fourier features of a closed contour. *Computer graphics and image processing*, 18(3):236–258.

Kulfan, B. (2009). Dr. john mcmasters: following the foot steps of a creative paleoaerodynamicist. In *47th AIAA Aerospace Sciences Meeting including The New Horizons Forum and Aerospace Exposition*, page 869.

Lamb, H. (1945). *Hydrodynamics*. Dover.

Lentink, D. and De Kat, R. (2014). Gliding swifts attain laminar flow over rough wings. *PloS one*, 9(6):e99901.

Lentink, D., Dickson, W. B., Van Leeuwen, J. L., and Dickinson, M. H. (2009). Leading-edge vortices elevate lift of autorotating plant seeds. *Science*, 324(5933):1438–1440.

Lentink, D., Müller, U., Stamhuis, E., De Kat, R., Van Gestel, W., Veldhuis, L., Henningsson, P., Hedenström, A., Videler, J. J., and Van Leeuwen, J. L. (2007). How swifts control their glide performance with morphing wings. *Nature*, 446(7139):1082–1085.

Lever, J., Krzywinski, M., and Altman, N. (2017). Points of significance: Principal component analysis. *Nature methods*, 14(7):641–643.

Li, H., Goodwill, T., Jane Wang, Z., and Ristroph, L. (2022). Centre of mass location, flight modes, stability and dynamic modelling of gliders. *Journal of Fluid Mechanics*, 937.

Lyon, C., Selig, M., Broeren, A., Lyon, C., Selig, M., and Broeren, A. (1997). Boundary layer trips on airfoils at low reynolds numbers. In *35th aerospace sciences meeting and exhibit*, page 511.

Magnus, H. (1853). Über die abweichung der geschosse—about the deviation of the projectiles. *Poggendorf's Ann. Phys. Chem.*, 88:1–28.

Mahadevan, L., Ryu, W. S., and Samuel, A. D. (1999). Tumbling cards. *Physics of Fluids*, 11(1):1–3.

Manurung, A. (2016). Elliptic fourier for shape analysis.

Maxwell, J. C. (1854). On a particular case of the descent of a heavy body in a resisting medium. *Camb. Dublin Math. J*, 9:145–148.

McCutchen, C. (1977). The spinning rotation of ash and tulip tree samaras. *Science*, 197(4304):691–692.

McLellan, T. and Endler, J. A. (1998). The relative success of some methods for measuring and describing the shape of complex objects. *Systematic Biology*, 47(2):264–281.

Microsoft (2019). Azure kinect dk documentation.

Minami, S. and Azuma, A. (2003). Various flying modes of wind-dispersal seeds. *Journal of Theoretical Biology*, 225(1):1–14.

Muir, R. E., Arredondo-Galeana, A., and Viola, I. M. (2017). The leading-edge vortex of swift wing-shaped delta wings. *Royal Society Open Science*, 4(8):170077.

Muja, M. and Lowe, D. G. (2009). Fast approximate nearest neighbors with automatic algorithm configuration. *VISAPP (1)*, 2(331-340):2.

Murphy, J. T. and Hu, H. (2010). An experimental study of a bio-inspired corrugated airfoil for micro air vehicle applications. *Experiments in Fluids*, 49(2):531–546.

Nachtigall, W. (1985). *Warum die Vögel fliegen*. Rasch und Röhring.

Nachtigall, W. (2011a). Nurflügler-samen von alsomitra macrocarpa—die besten pflanzlichen gleitflieger der welt. teil 1: Funktionsmorphologie und gleitflug. *Mikrokosmos*, 100(4):223.

Nachtigall, W. (2011b). Nurflügler-samen von alsomitra macrocarpa—die besten pflanzlichen gleitflieger der welt. teil 2: Optimierung und größenvergleich. *Mikrokosmos*.

Nachtigall, W. (2012). Nurflügler-samen von alsomitra macrocarpa—die besten pflanzlichen gleitflieger der welt. teil 4: Die" aerodynamische visitenkarte". mit einer einführung in die strömungstechnik. *Mikrokosmos*, 101(1):51.

Nakamura, T. (2011). Real-time 3-d object tracking using kinect sensor. In *2011 IEEE International Conference on Robotics and Biomimetics*, pages 784–788. IEEE.

Neto, J. C., Meyer, G. E., Jones, D. D., and Samal, A. K. (2006). Plant species identification using elliptic fourier leaf shape analysis. *Computers and electronics in agriculture*, 50(2):121–134.

Okamoto, M. and Azuma, A. (2011). Aerodynamic characteristics at low reynolds number for wings of various planforms. *AIAA journal*, 49(6):1135–1150.

Onoue, K. and Breuer, K. S. (2016). Vortex formation and shedding from a cyber-physical pitching plate. *Journal of Fluid Mechanics*, 793:229–247.

References

Ōtomo, S., Henne, S., Mulleners, K., Ramesh, K., and Viola, I. M. (2021). Unsteady lift on a high-amplitude pitching aerofoil. *Experiments in Fluids*, 62(1):1–18.

Overbeck, G. E., Müller, S. C., Fidelis, A., Pfadenhauer, J., Pillar, V. D., Blanco, C. C., Boldrini, I. I., Both, R., and Forneck, E. D. (2007). Brazil's neglected biome: the south brazilian campos. *Perspectives in Plant Ecology, Evolution and Systematics*, 9(2):101–116.

Pajno, V. (2010). *Sailplaine [ie Sailplane] Design: A Guide for Students and Designers: from Drafting to Flight Test*. IBN.

Pesavento, U. (2006). *Unsteady aerodynamics of falling plates*. Cornell University.

Pesavento, U. and Wang, Z. J. (2004). Falling paper: Navier-stokes solutions, model of fluid forces, and center of mass elevation. *Physical review letters*, 93(14):144501.

Pullin, D. and Wang, Z. J. (2004). Unsteady forces on an accelerating plate and application to hovering insect flight. *Journal of Fluid Mechanics*, 509:1–21.

Rattenborg, N. C., Voirin, B., Cruz, S. M., Tisdale, R., Dell'Omo, G., Lipp, H.-P., Wikelski, M., and Vyssotski, A. L. (2016). Evidence that birds sleep in mid-flight. *Nature communications*, 7:12468.

Rees, C. J. (1975a). Aerodynamic properties of an insect wing section and a smooth aerofoil compared. *Nature*, 258(5531):141.

Rees, C. J. (1975b). Form and function in corrugated insect wings. *Nature*, 256(5514):200–203.

Rose, J. P., Kriebel, R., and Sytsma, K. J. (2016). Shape analysis of moss (bryophyta) sporophytes: Insights into land plant evolution. *American Journal of Botany*, 103(4):652–662.

Rusu, R. B., Marton, Z. C., Blodow, N., Dolha, M., and Beetz, M. (2008). Towards 3d point cloud based object maps for household environments. *Robotics and Autonomous Systems*, 56(11):927–941.

Saito, K., Ishitsuka, Y., and Ito, A. (2008). Flow visualization around seeds of alsomitra macrocarpa.

Schafer, R. W. (2011). What is a savitzky-golay filter?[lecture notes]. *IEEE Signal processing magazine*, 28(4):111–117.

Schindelin, J., Arganda-Carreras, I., Frise, E., Kaynig, V., Longair, M., Pietzsch, T., Preibisch, S., Rueden, C., Saalfeld, S., Schmid, B., et al. (2012). Fiji: an open-source platform for biological-image analysis. *Nature methods*, 9(7):676–682.

Schlichting, H. and Gersten, K. (2015). *Boundary layer theory*. Springer.

Sedov, L. (1980). *Two-dimensional problems of hydrodynamics and aerodynamics*. Moscow Izdatel Nauka.

Seiichi, S., Nao, M., Koji, T., and Tetsuya, Y. (2008). Morphological design of dandelion.

Shannon, C. (1949). Communication in the presence of noise. *Proceedings of the IRE*, 37(1):10–21.

Singapore, N. P. (2021). National parks alsomitra macrocarpa.

Sobel, A. (2012). Tropical weather. nature education knowledge, 3 (12): 2.

Srisuwan, T. (2020). Phyto-inspired design: Innovative solutions for architecture. *International Journal of Building, Urban, Interior and Landscape Technology (BUILT)*, 16:7–22.

Taani, M. (2020). *Non-standard neutrino interaction analysis with atmospheric neutrino data in Super-Kamiokande I-IV and the design of the Hyper-Kamiokande outer detector*. PhD thesis, University of Edinburgh.

Tanabe, Y. and Kaneko, K. (1994). Behavior of a falling paper. *Physical Review Letters*, 73(10):1372.

Thomas, A. L. and Taylor, G. K. (2001). Animal flight dynamics i. stability in gliding flight. *Journal of theoretical biology*, 212(3):399–424.

Tölgyessy, M., Dekan, M., Chovanec, L., and Hubinskỳ, P. (2021). Evaluation of the azure kinect and its comparison to kinect v1 and kinect v2. *Sensors*, 21(2):413.

Torenbeek, E. and Wittenberg, H. (2009). *Flight physics: essentials of aeronautical disciplines and technology, with historical notes*. Springer Science & Business Media.

Van Valen, L. (1962). A study of fluctuating asymmetry. *Evolution*, pages 125–142.

Vargas, A., Mittal, R., and Dong, H. (2008). A computational study of the aerodynamic performance of a dragonfly wing section in gliding flight. *Bioinspiration & biomimetics*, 3(2):026004.

Varshney, K., Chang, S., and Wang, Z. J. (2011). The kinematics of falling maple seeds and the initial transition to a helical motion. *Nonlinearity*, 25(1):C1.

Videler, J., Stamhuis, E., and Povel, G. (2004). Leading-edge vortex lifts swifts. *Science*, 306(5703):1960–1962.

Vincent, L., Liu, Y., and Kanso, E. (2020a). Shape optimization of tumbling wings. *Journal of Fluid Mechanics*, 889.

Vincent, L., Zheng, M., Costello, J. H., and Kanso, E. (2020b). Enhanced flight performance in non-uniformly flexible wings. *Journal of the Royal Society Interface*, 17(168):20200352.

Viola, I. M., Nakayama, N., and Dickinson, M. H. (2022). Quick guide on plant seed aerodynamics.

Vogel, S. (1996). *Life in moving fluids: the physical biology of flow*. Princeton University Press.

Wang, Z. J., Birch, J. M., and Dickinson, M. H. (2004). Unsteady forces and flows in low reynolds number hovering flight: two-dimensional computations vs robotic wing experiments. *Journal of Experimental Biology*, 207(3):449–460.

Weis-Fogh, T. (1973). Quick estimates of flight fitness in hovering animals, including novel mechanisms for lift production. *Journal of experimental Biology*, 59(1):169–230.

White, F. M. and Majdalani, J. (2006). *Viscous fluid flow*, volume 3. McGraw-Hill New York.

Whitesides, G. M. (2015). Bioinspiration: something for everyone. *Interface focus*, 5(4):20150031.

Wilroy, J., Wahidi, R. A., and Lang, A. (2018). Effect of butterfly-scale-inspired surface patterning on the leading edge vortex growth. *Fluid Dynamics Research*, 50(4):045505.

Zhou, J., Adrian, R. J., Balachandar, S., and Kendall, T. (1999). Mechanisms for generating coherent packets of hairpin vortices in channel flow. *Journal of fluid mechanics*, 387:353–396.